

# Important Notice

This copy may be used only for the purposes of research and private study, and any use of the copy for a purpose other than research or private study may require the authorization of the copyright owner of the work in question. Responsibility regarding questions of copyright that may arise in the use of this copy is assumed by the recipient.

**AVO developments applied to Blackfoot 3C-2D  
broadband line**

by

Yong Xu

M.Sc. Thesis  
University of Calgary  
Department of Geology and Geophysics  
December, 1999



*Consortium for Research in  
Elastic Wave Exploration and Seismology*

© Yong Xu 1999



## ABSTRACT

This thesis evaluates and refines AVO analysis of the data from 3C-2D broadband line in Blackfoot using the vertical and radial components data. AVO attributes and elastic parameters are studied for the hydrocarbon indication and lithology differentiation in the thesis.

The  $P$ - $S$  reflection coefficient is studied to look for a formula for analysis of the radial component data. The sensitivities of Lamé's parameters to hydrocarbon saturation and lithologic changes is studied. The method to extract Lamé's parameter information is presented. The noise issue in the AVO analysis is studied.

Four wells with shear sonic logs in Blackfoot are analyzed to extract a linear relationship between  $P$  wave velocity and  $S$  wave velocity. This linear trend is used to calculate the anomalies from the  $P$  wave reflectivity and  $S$  wave reflectivity extracted from vertical component data, both CMP gathers and CSP gathers. Pure  $S$  wave reflectivity is extracted from radial component. Lamé's parameters are extracted from vertical component. The AVO analysis results show a strong anomaly on the Glauconitic channel.

## **ACKNOWLEDGEMENTS**

I thank Dr. John. C. Bancroft for his supervision on my studies.

I thank the sponsors of CREWES project.

I thank all people who taught or helped me in my study and life.

*Dedicated to my wife and my parents*

## TABLE OF CONTENTS

APPROVAL PAGE.....	ii
ABSTRACT.....	iii
ACKNOWLEDGEMENTS.....	iv
DEDICATION.....	v
TABLE OF CONTENTS.....	vi
LIST OF TABLES.....	viii
LIST OF FIGURES.....	iv
LIST OF SYMBOL DEFINITIONS.....	xvii
CHAPTER 1: INTRODUCTION.....	1
1.1    Rock properties inside AVO.....	1
1.2    Theoretical basis of AVO analysis.....	2
1.3 <i>P-S</i> AVO analysis.....	3
1.4    What's covered in the thesis.....	4
CHAPTER 2: REFLECTIVITY DEPENDENT ON INCIDENT ANGLES.....	5
2.1    Compressional wave propagation.....	5
2.2    Snell's law.....	5
2.3    Aki and Richards' approximations.....	6
2.3.1    Simplified and meaningful equations.....	6
2.3.2    Ostrander's hypothetical gas sand model.....	8
2.3.3    Accuracy of Aki and Richards' approximations.....	8
2.4    More accurate approximations of <i>P-S</i> reflection coefficient.....	10
2.4.1    Higher order truncation.....	10
2.4.2    Comparisons of various expressions using models.....	11
2.4.3    Corrections of the first order approximations.....	15
2.4.4    Comparisons using other models.....	18
2.4    Relationship between $R_{PS}$ and $R_{SS}$ .....	20
CHAPTER 3: METHODOLOGY OF AVO ANALYSIS .....	22
3.1    Methods of AVO analysis.....	22
3.1.1    Various AVO extraction methods.....	23
3.1.1.1    Shuey's simplification of the Zoeppritz equation.....	24
3.1.1.2    Hilterman's approximation.....	25
3.1.1.3    Smith & Gidlow's weighted stack method.....	25
3.1.1.4    Fatti et. al.'s method.....	26
3.1.1.5    Lame's parameters extraction.....	27
3.1.1.6    Xu and Bancroft's extraction.....	28
3.1.1.7    Gray's extraction.....	29
3.1.2    Methodology of AVO extraction.....	30
3.1.3    Fluid factor.....	31

3.2	Sensitivities of elastic parameters in AVO analysis.....	33
3.2.1	Dry rock line.....	34
3.2.2	$\kappa-\mu$ as hydrocarbon indicator.....	36
3.2.3	Cross-plots of well log elastic parameters.....	40
3.2.4	Relative changes of physical properties.....	42
3.3	Noise in AVO analysis.....	45
3.3.1	Theory review of $L1$ and $L2$ norms.....	45
3.3.2	Comparisons of $L1$ norm and $L2$ norm estimations.....	47
3.3.2.1	Multiple effects.....	47
3.3.2.2	Linear noises.....	57
3.3.2.3	Random noises.....	64
3.4	Decoupling lithology change by crossplotting $\frac{\Delta\lambda}{\lambda+2\mu}$ and $\frac{\Delta\mu}{\lambda+2\mu}$ .....	67
3.4.1	Crossplot of $\Delta\mu/(\lambda+2\mu)$ and $\Delta\lambda/(\lambda+2\mu)$ for 25 set of samples (Castagna, 1994).....	69
3.4.2	Relationship between $\Delta\mu/(\lambda+2\mu)$ and $\Delta\lambda/(\lambda+2\mu)$ .....	73
3.4.3	Decoupling of lithology by crossplotting.....	76
3.5	AVO analysis after equivalent offset migration.....	79

CHAPTER 4: AVO ANALYSIS OF BLACKFOOT MULTI-COMPONENT SEISMIC DATA.....		82
4.1	Blackfoot survey.....	82
4.2	Statistical relationship between $V_P$ and $V_S$ from well logs.....	86
4.2.1	Review of fluid factor method.....	86
4.2.2	Statistical relationship between $V_P$ and $V_S$ .....	86
4.2.3	Summary of the statistical analysis.....	89
4.3	Lame parameters extraction from vertical component.....	100
4.3.1	Background.....	100
4.3.2	Equations in Lamé's parameter extraction.....	100
4.3.3	Lamé's parameter extraction from vertical component.....	102
4.3.3.1	$V_P/V_S$ ratio reflectivity.....	103
4.3.3.2	Extraction results.....	104
4.3.3.3	Inversion of extracted Lamé parameters.....	107
4.4	Extraction of $R_p$ and $R_s$ and fluid factor from vertical component data.....	109
4.4.1	Methodologies.....	109
4.4.2	Extraction results.....	111
4.4.3	Correlation of the extractions with well logs.....	117
4.4.4	$R_p$ , $R_s$ , and fluid factor from CSP gathers.....	120
4.5	Analysis of radial component data.....	122
4.5.1	Methodologies.....	122
4.5.2	Extraction result from radial component.....	123
CHAPTER 5: CONCLUSIONS AND DISCUSSIONS.....		126
5.1	Chapter summary.....	126

5.2	Summary of methodology study.....	127
5.3	Summary of work on Blackfoot survey.....	128
5.4	Problems and discussions.....	128
REFERENCES .....		130
APPENDIX.....		134
A.	Zoeppritz equations of P-P and P-S reflection coefficient.....	134
B.	Derivation of equations (3.7) and (3.8) .....	135

## TABLE OF TABLES

Table 2.1	Property of second gas sand model.....	18
Table 3.1	Properties for a gas sand model.....	39
Table 3.2	Shallow Gas Sand Log Measurements (Goodway et al, 1997).....	39
Table 3.3	The RMS deviations, errors of fitted $R_p$ and $R_s$ for Figures 3.9 to 3.22 .....	49
Table 3.4	The RMS deviations, errors of fitted $R_p$ and $R_s$ for the spikes before band pass filtering in Figure 3.21.....	57
Table 3.5	The RMS deviations, and the errors of fitted $R_p$ and $R_s$ for Figures 3.23 to 3.34.....	57
Table 3.6	The RMS deviations and errors of fitted $R_p$ and $R_s$ for Figures 3.35 to 3.37.....	64
Table 3.7	Properties for 25 set of sand and shale samples (Castagna et al., 1994).....	68
Table 4.1	The top depth and bottom depth of the dipole logs of the four wells, 04-16, 08-08, 09-17, and 12-16.....	86

## TABLE OF FIGURES

Figure 2.1.	Waves generated by an incident P-wave at an interface between two infinite elastic half spaces.....	5
Figure 2.2	Three-layer hypothetical gas sand model (Ostrander, 1984).....	8
Figure 2.3	The exact and approximated reflection coefficients in the media with elastic properties specified in Figure 2.2. The solid lines are for the exact reflection coefficients and the dash lines are for Aki-Richards' approximations of reflection coefficients.....	9
Figure 2.4	Comparisons of the exact <i>P-S</i> reflection coefficients, Aki-Richards approximation (2.3), and equation (2.8), for the three-layer sand model in Figure 2.2. The reflection coefficients versus incident angles are indicated in (a), (b), (c), and (d). The relative errors versus incident angles are indicated in (e), (f), (g), and (h).....	14
Figure 2.5	Comparisons of the exact <i>P-S</i> reflection coefficients, Aki-Richards' approximation (2.3), equations (2.10), (2.11), and (2.12), for the three-layer sand model in Figure 2.2. On each panel, the curve for equation (2.10) overlaps with the curve for Aki-Richards' approximation, due to the close accuracies of both.....	15
Figure 2.6	Plots of equations (2.3), (2.8), (2.13) and (2.14) after division by $\tan j$ versus incident angle.....	17
Figure 2.7	Comparisons of the exact <i>P-S</i> reflection coefficients, Aki-Richards' approximation (2.3), equation (2.8), equation (2.13) and equation (2.14) for the three-layer sand model in Figure 2.2.....	18
Figure 2.8	Comparison of the approximations and exact <i>P-S</i> reflection coefficients for gas sand model in Table 2.1.....	19
Figure 2.9	The average relative error of Aki-Richards' approximation for the macro layers from well logs (Blackfoot 0808 well).....	20
Figure 2.10	Comparisons of <i>P-S</i> reflection coefficients in equation (2.8), Aki-Richards approximation--equations (2.3), (2.8), and (2.16)--relationship between <i>P-S</i> and <i>S-S</i> . The four panels demonstrate the <i>P-S</i> reflection coefficients versus angle of incidence for the three-layer sand model in Figure 2.2.....	21
Figure 3.1	Relationships of clastic rocks (Castagna, 1985). (a) The computed relationships between the bulk and shear moduli (normalized by density) based on the observed $V_s$ and $V_p$ trends. (b) The computed relationships between Poisson's ratio and $V_p$ based on the observed $V_s$ and $V_p$ trends. (c) The computed relationships between the bulk modulus (normalized by density) and $V_p$ based on the observed $V_s$ and $V_p$ trends. (d) Gassmann's equation prediction and observed $V_p$ and $V_s$ .....	36
Figure 3.2	$\lambda\rho$ vs $\mu\rho$ crossplot of Gas well log data (Goodway et al, 1997).....	37

Figure 3.3	$\kappa\rho$ vs $\mu\rho$ crossplot of gas well log data.....	38
Figure 3.4	$(\kappa-\mu)\rho$ vs $\mu\rho$ crossplot of Gas well log data.....	39
Figure 3.5	Cross-plots of well 08-08 in Blackfoot.....	41
Figure 3.6	The cross-plots of elastic parameters of the Glauconitic formation.....	42
Figure 3.7	Comparisons of various relative changes of rock parameters from well 08-08 in Blackfoot survey. (a) $\Delta Vp/Vp$ ; (b) $\Delta Vs/Vs$ ; (c) $\Delta\rho/\rho$ ; (d) $\Delta\lambda/\lambda$ ; (e) $\Delta\mu/\mu$ ; (f) $\Delta(\kappa-\mu)/(\kappa-\mu)$ ; (g) $\Delta\mu/(\lambda+2\mu)$ ; (h) $\Delta\lambda/(\lambda+2\mu)$ ; (i) $\Delta(\lambda+2\mu)/(\lambda+2\mu)$ .....	44
Figure 3.8	A primary reflection model. The reflectivities versus offsets are on the left side. The right side is the AVO gather created by convolution of reflectivities with bandpass filter of 5-10-60-70 Hz.....	48
Figure 3.9	A reflection model with primary reflection contaminated by multiple. The reflectivities versus offsets are on left side. The right side is the AVO gather created by convolution of reflectivities with bandpass filter of 5-10-60-70 Hz. At 1.0s $D/A_{exp} = 23.5\%$ .....	50
Figure 3.10	The exact primary reflection amplitude, multiple polluted primary reflection amplitude, recovered amplitude from extracted $R_p$ and $R_s$ using $L1$ , and recovered amplitude from extracted $R_p$ and $R_s$ using $L2$ norm fitting. The data used for extraction is shown in Figure 3.9. The amplitude at each offset at 1.0s is picked on noise free data, noise data, and reconstructed data from the extraction results. Same work is done for other similar plots.....	50
Figure 3.11	A reflection model with primary reflection contaminated by multiple. The reflectivities versus offsets are on left side. The right side is the AVO gather created by convolution of reflectivities with bandpass filter of 5-10-60-70 Hz. At 1.0s $D/A_{exp} = 32.4\%$ .....	51
Figure 3.12	The exact primary reflection amplitude, multiple polluted primary reflection amplitude, recovered amplitude from extracted $R_p$ and $R_s$ using $L1$ , and recovered amplitude from extracted $R_p$ and $R_s$ using $L2$ norm fitting. The data used for extraction is shown in Figure 3.11.....	51
Figure 3.13	A reflection model with primary reflection contaminated by multiple. The reflectivities versus offsets are on left side. The right side is the AVO gather created by convolution of reflectivities with bandpass filter of 5-10-60-70 Hz. At 1.0s $D/A_{exp} = 39.7\%$ .....	52
Figure 3.14	The exact primary reflection amplitude, multiple polluted primary reflection amplitude, recovered amplitude from extracted $R_p$ and $R_s$ using $L1$ , and recovered amplitude from extracted $R_p$ and $R_s$ using $L2$ norm fitting. The data used for extraction is shown in Figure 3.13.....	52
Figure 3.15	A reflection model with primary reflection contaminated by multiple. The reflectivities versus offsets are on left side. The right side is the AVO gather created by convolution of reflectivities with bandpass filter of 5-10-60-70 Hz. At 1.0s $D/A_{exp} = 45.6\%$ .....	53

Figure 3.16 The exact primary reflection amplitude, multiple polluted primary reflection amplitude, recovered amplitude from extracted  $R_p$  and  $R_s$  using  $L1$ , and recovered amplitude from extracted  $R_p$  and  $R_s$  using  $L2$  norm fitting. The data used for extraction is shown in Figure 3.15.....53

Figure 3.17 A reflection model with primary reflection contaminated by multiple. The reflectivities versus offsets are on left side. The right side is the AVO gather created by convolution of reflectivities with bandpass filter of 5-10-60-70 Hz. At 1.0s  $D/A_{exp}=50.0\%$ .....54

Figure 3.18 The exact primary reflection amplitude, multiple polluted primary reflection amplitude, recovered amplitude from extracted  $R_p$  and  $R_s$  using  $L1$ , and recovered amplitude from extracted  $R_p$  and  $R_s$  using  $L2$  norm fitting. The data used for extraction is shown in Figure 3.17.....54

Figure 3.19 A reflection model with primary reflection contaminated by multiple. The reflectivities versus offsets are on left side. The right side is the AVO gather created by convolution of reflectivities with bandpass filter of 5-10-60-70 Hz. At 1.0s  $D/A_{exp}=54.4\%$ .....55

Figure 3.20 The exact primary reflection amplitude, multiple polluted primary reflection amplitude, recovered amplitude from extracted  $R_p$  and  $R_s$  using  $L1$ , and recovered amplitude from extracted  $R_p$  and  $R_s$  using  $L2$  norm fitting. The data used for extraction is shown in Figure 3.19.....55

Figure 3.21 A reflection model with primary reflection contaminated by multiple. The reflectivities versus offsets are on the left side. The right side is the AVO gather created by convolution of reflectivities with bandpass filter of 5-10-60-70 Hz. At 1.0s  $D/A_{exp}=100.0\%$ .....56

Figure 3.22 The exact primary reflection amplitude, multiple polluted primary reflection amplitude, recovered amplitude from extracted  $R_p$  and  $R_s$  using  $L1$ , and recovered amplitude from extracted  $R_p$  and  $R_s$  using  $L2$  norm fitting. The data used for extraction is shown in Figure 3.21.....56

Figure 3.23 A reflection model with primary reflection contaminated by linear noise. The linear event crosses over primary reflection event at medium offsets. The reflectivities versus offsets are on the left side. The right side is the AVO gather created by convolution of reflectivities with bandpass filter of 5-10-60-70 Hz. At 1.0s  $D/A_{exp}=36.8\%$ .....58

Figure 3.24 The exact primary reflection amplitude, linear noise polluted primary reflection amplitude, recovered amplitude from extracted  $R_p$  and  $R_s$  using  $L1$ , and recovered amplitude from extracted  $R_p$  and  $R_s$  using  $L2$  norm fitting. The data used for extraction is shown in Figure 3.23.....58

Figure 3.25 A reflection model with primary reflection contaminated by linear noise. The linear event crosses over the primary reflection event at far offsets. The reflectivities versus offsets are on the left side. The right side is the AVO gather created by convolution of reflectivities with bandpass filter of 5-10-60-70 Hz. At 1.0s  $D/A_{exp}=36.8\%$ .....59

Figure 3.26	The exact primary reflection amplitude, linear noise polluted primary reflection amplitude, recovered amplitude from extracted $R_p$ and $R_s$ using $L1$ , and recovered amplitude from extracted $R_p$ and $R_s$ using $L2$ norm fitting. The data used for extraction is shown in Figure 3.25.....	59
Figure 3.27	A reflection model with primary reflection contaminated by linear noise. The linear event crosses over primary reflection event at near offsets. The reflectivities versus offsets are on the left side. The right side is the AVO gather created by convolution of reflectivities with bandpass filter of 5-10-60-70 Hz. At 1.0s $D/A_{exp}=36.8\%$ .....	60
Figure 3.28	The exact primary reflection amplitude, linear noise polluted primary reflection amplitude, recovered amplitude from extracted $R_p$ and $R_s$ using $L1$ , and recovered amplitude from extracted $R_p$ and $R_s$ using $L2$ norm fitting. The data used for extraction is shown in Figure 3.27.....	60
Figure 3.29	A reflection model with primary reflection contaminated by two linear noise events. The two linear events cross over the primary reflection event at the near and far offsets. The two linear events possess the same phase. The reflectivities versus offsets are on the left hand side. The right side is the AVO gather created by convolution of reflectivities, with bandpass filter of 5-10-60-70 Hz. At 1.0s $D/A_{exp}=51.5\%$ .....	61
Figure 3.30	The exact primary reflection amplitude, linear noise polluted primary reflection amplitude, recovered amplitude from extracted $R_p$ and $R_s$ using $L1$ , and recovered amplitude from extracted $R_p$ and $R_s$ using $L2$ norm fitting. The data used for extraction is shown in Figure 3.29.....	61
Figure 3.31	A reflection model with primary reflection contaminated by two linear noise events. The two linear events cross over the primary reflection event at the near and far offsets. The linear event at the near offset has reverse polarity compared with primary reflection. The far offset linear event has the same polarity as primary reflection. The reflectivities versus offsets are on the left hand side. The right hand side is the AVO gather created by convolution of reflectivities with bandpass filter of 5-10-60-70 Hz. At 1.0s $D/A_{exp}=51.5\%$ ..	62
Figure 3.32	The exact primary reflection amplitude, linear noise polluted primary reflection amplitude, recovered amplitude from extracted $R_p$ and $R_s$ using $L1$ , and recovered amplitude from extracted $R_p$ and $R_s$ using $L2$ norm fitting. The data used for extraction is shown in Figure 3.31.....	62
Figure 3.33	A reflection model with primary reflection contaminated by two linear noise events. The two linear events cross over the primary reflection event at the near and far offsets. The linear event at the near has the same polarity as primary reflection. The far offset linear event has reverse polarity. The reflectivities versus offsets are on left side. The right side is the AVO gather created by convolution of reflectivities with bandpass filter of 5-10-60-70 Hz. At 1.0s $D/A_{exp}=51.5\%$ .....	63

Figure 3.34	The exact primary reflection amplitude, linear noise polluted primary reflection amplitude, recovered amplitude from extracted $R_p$ and $R_s$ using $L1$ , and recovered amplitude from extracted $R_p$ and $R_s$ using $L2$ norm fitting. The data used for extraction is shown in Figure 3.33.....	63
Figure 3.35	The exact primary reflection amplitude, 10% random noise polluted primary reflection amplitude, recovered amplitude from extracted $R_p$ and $R_s$ using $L1$ , and recovered amplitude from extracted $R_p$ and $R_s$ using $L2$ norm fitting.....	64
Figure 3.36	The exact primary reflection amplitude, 20% random noise polluted primary reflection amplitude, recovered amplitude from extracted $R_p$ and $R_s$ using $L1$ , and recovered amplitude from extracted $R_p$ and $R_s$ using $L2$ norm fitting.....	65
Figure 3.37	The exact primary reflection amplitude, 30% random noise polluted primary reflection amplitude, recovered amplitude from extracted $R_p$ and $R_s$ using $L1$ , and recovered amplitude from extracted $R_p$ and $R_s$ using $L2$ norm fitting.....	65
Figure 3.38	Crossplot of $\Delta\mu$ and $\Delta\lambda$ for 25 sets of samples.....	70
Figure 3.39	Crossplot of $\Delta\mu/(\lambda+2\mu)$ and $\Delta\lambda/(\lambda+2\mu)$ for 25 sets of samples.....	71
Figure 3.40	$\Delta\mu$ and $\Delta\lambda$ for 25 sets of samples (shale to brine sand).....	71
Figure 3.41	$\Delta\mu$ and $\Delta\lambda$ for 25 sets of samples (shale to gas sand).....	72
Figure 3.42	$\Delta\mu/(\lambda+2\mu)$ and $\Delta\lambda/(\lambda+2\mu)$ for 25 sets of samples (shale to brine sand).....	72
Figure 3.43	$\Delta\mu/(\lambda+2\mu)$ and $\Delta\lambda/(\lambda+2\mu)$ for 25 sets of samples (shale to gas sand).....	72
Figure 3.44	$\Delta\mu/(\lambda+2\mu)$ and $\Delta\lambda/(\lambda+2\mu)$ assuming constant $V_p/V_s$ and constant density. $V_p/V_s$ increase counterclockwise.....	73
Figure 3.45	$\Delta\mu/(\lambda+2\mu)$ and $\Delta\lambda/(\lambda+2\mu)$ assuming linear $V_p$ versus $V_s$ and constant density. $V_p/V_s$ increase counterclockwise. On the left, the slope of $V_p$ versus $V_s$ is 1.16; on the right the slope is 1.25.....	74
Figure 3.46	$\Delta\mu/(\lambda+2\mu)$ and $\Delta\lambda/(\lambda+2\mu)$ assuming linear $V_p$ versus $V_s$ and Gardner density ( $g=0.25$ ). $V_p/V_s$ increase counterclockwise. On the left, the slope of $V_p$ versus $V_s$ is 1.16; on the right the slope is 1.25.....	75
Figure 3.47	25 sets of samples overlaid the relationship between $\Delta\mu/(\lambda+2\mu)$ and $\Delta\lambda/(\lambda+2\mu)$ assuming linear $V_p$ versus $V_s$ and Gardner density. The slope of $V_p$ versus $V_s$ is 1.16. On the right, the circles ('o') are for shale to gas sand; the '*'s for shale to brine sand.....	76
Figure 3.48	Crossplot of $V_p$ and $V_s$ for the linear $V_p$ versus $V_s$ model.....	77
Figure 3.49	Crossplot of $R_p$ and $R_s$ for the linear $V_p$ versus $V_s$ model.....	77
Figure 3.50	Crossplot of intercept and gradient for the linear $V_p$ versus $V_s$ model.....	78
Figure 3.51	Crossplot of $\Delta\lambda/(\lambda+2\mu)$ and $\Delta\mu/(\lambda+2\mu)$ for the linear $V_p$ versus $V_s$ model.....	78

Figure 3.52	Ray diagram for a) a given source and receiver, and b) a colocated source and receiver that defines the equivalent offset.....	80
Figure 4.1	Location map of 3C-2D seismic line 950278, well control and the incised valley isopach (Miller et. al., 1995).....	83
Figure 4.2	$V_p/V_s$ map from Lower Mannville to Wabamun (Yang et al, 1996).....	84
Figure 4.3	Log curves of well 04-16 and formation tops.....	91
Figure 4.4	Log curves of well 08-08 and the formation tops.....	92
Figure 4.5	Log curves of well 09-17 and formation tops.....	93
Figure 4.6	Log curves of well 12-16 and formation tops.....	94
Figure 4.7	Compressional and shear wave velocities for mud-rocks from in-situ sonic and field seismic measurements (Castagna et. al., 1985).....	95
Figure 4.8	Cross-plot of $V_p$ and $V_s$ of well 04-16 (all data above Mississippian formation).....	96
Figure 4.9	Cross-plot of $V_p$ and $V_s$ of well 04-16 (portion below 1000 meters and above Mississippian formation).....	96
Figure 4.10	Cross-plot of $V_p$ and $V_s$ of well 08-08 (portion below 1000 meters and above Mississippian formation).....	97
Figure 4.11	Cross-plot of $V_p$ and $V_s$ of well 09-17 (above Mississippian formation).....	97
Figure 4.12	Cross-plot of $V_p$ and $V_s$ of well 12-16 (portion above Mississippian formation).....	98
Figure 4.13	Cross-plot of $V_p$ and $V_s$ of four wells (portion above Mississippian formation).....	98
Figure 4.14	Cross-plot of $V_p$ and $V_s$ of four wells (portion above Mississippian formation).....	99
Figure 4.15	Well 0808 and synthetic gather from the well (Margrave et al, 1995, Potter et al, 1996).....	102
Figure 4.18	The analysis results of Blackfoot vertical seismic data.....	107
Figure 4.19	The inversion results from Figure 4.18.....	108
Figure 4.20	Statistical relationship between $V_p$ and $V_s$ from 04-16 well and $V_p$ 's deviations from this statistical relationship.....	112
Figure 4.21	Stack section of vertical component of 10Hz data.....	112
Figure 4.22	Extraction $P$ wave reflectivity section from vertical component.....	113
Figure 4.23	Extracted $S$ wave reflectivity from vertical component.....	114

Figure 4.24 Fluid factor section calculated from extracted $P$ wave and $S$ wave sections and the mud-rock line.....	115
Figure 4.25 Zooming of fluid factor section of Figure 4.24 with channel zone.....	116
Figure 4.26 Well logs, synthetics and $R_s$ extracted from vertical component.....	118
Figure 4.27 Well logs, synthetics and $R_s$ extracted from vertical component.....	118
Figure 4.28 Well logs and fluid factor extracted from vertical component.....	119
Figure 4.29 Fluid factor extracted from well logs and from vertical component.....	119
Figure 4.30 Extraction $P$ wave reflectivity section from CSP gathers of the vertical component.....	120
Figure 4.31 Extraction $S$ wave reflectivity section from CSP gathers of the vertical component.....	121
Figure 4.32 Fluid factor section calculated from $P$ and $S$ wave reflectivity sections from CSP gathers of the vertical component.....	121
Figure 4.33 Illustration of propagation of incidence and converted wave.....	121
Figure 4.35 Stack section of the radial component with the same muting gate as in the AVO extraction.....	122
Figure 4.36 The extracted $S$ wave normal incidence reflectivity from radial component.....	122
Figure A-1 Waves generated at an interface by an incident P-wave.....	135

## LIST OF SYMBOL DEFINITIONS

$\kappa$	bulk modulus
$\mu$	shear modulus or rigidity
$\lambda$	incompressibility
$V_p$	compressional wave velocity
$V_S$	shear wave velocity
$\rho$	density
$\Delta V_P$	difference of P velocities on both sides of an interface
$V_{Pa}$	average of P velocities on both sides of an interface
$\Delta F$	fluid factor
$i_1$	<i>P</i> wave incident angle and reflected angle
$i_2$	<i>P</i> wave transmitted angle
$j_1$	<i>S</i> wave reflected angle
$j_2$	<i>S</i> wave transmitted angle
$i$	$(i_1+i_2)/2$
$j$	$(j_1+j_2)/2$
$\alpha_1$	<i>P</i> wave velocity of upper side of the interface
$\alpha_2$	<i>P</i> wave velocity of lower side of the interface
$\beta_1$	<i>S</i> wave velocity of upper side of the interface
$\beta_2$	<i>S</i> wave velocity of lower side of the interface
$\rho_1$	density of upper side of the interface
$\rho_2$	density of lower side of the interface
$\Delta\alpha$	$\alpha_2 - \alpha_1$
$\Delta\beta$	$\beta_2 - \beta_1$
$\Delta\rho$	$\rho_2 - \rho_1$
$\alpha$	$(\alpha_2 + \alpha_1)/2$
$\beta$	$(\beta_2 + \beta_1)/2$
$\rho$	$(\rho_2 + \rho_1)/2$

$p$	ray parameter
$R_{PP}$	reflection coefficient at any incident angle for $P$ wave incidence and $P$ wave reflection
$R_{PS}$	reflection coefficient at any incident angle for $P$ wave incidence and $S$ wave reflection
$R_{SS}$	reflection coefficient at any incident angle for $S$ wave incidence and $S$ wave reflection
$R_{P0}$	normal incident $P$ wave reflectivity
$R_{S0}$	normal incident $S$ wave reflectivity
$\theta$	average of incident and transmitted angles of $P$ waves
$\sigma$	Poisson's ratio
$I_p$	$P$ wave impedance
$I_s$	$S$ wave impedance
$\kappa_W$	bulk modulus of the wet rock
$\kappa_S$	bulk modulus of the grains
$\kappa_D$	bulk modulus of the dry frame
$\kappa_F$	bulk modulus of the fluid,
$\mu_W$	shear modulus of the wet rock
$\mu_D$	shear modulus of the dry rock
$\rho_W$	density of the wet rock
$\rho_F$	density of the fluid
$\rho_S$	density of the grains
$\phi$	rock porosity
$A_{exp}$	average value of noise free samples
$D$	RMS deviation of noise data from noise free values
$h_e$	equivalent offset
$\gamma$	$V_p/V_s$ ratio
$R_P$	normal incident $P$ wave reflectivity
$R_S$	normal incident $S$ wave reflectivity

# CHAPTER 1 INTRODUCTION

Since Ostrander (1982) demonstrated that gas sand reflection coefficients vary in an anomalous fashion with increasing offset and showed how to utilize this anomalous behavior as a direct hydrocarbon indicator on real data, this methodology of amplitude variation with offset (AVO) analysis has come to be popularized. The potential of the analysis of offset-dependent reflectivity lies in that the reflection coefficient is the function of the incident angle and the variations in compressional wave velocity ( $V_P$ ), shear wave velocity ( $V_S$ ), and density ( $\rho$ ) across an interface of media. These variations in  $V_P$ ,  $V_S$ , and  $\rho$  are, in turn, dependent on rock property variations. In particular, an interface between gas-saturated and water-saturated unconsolidated or poorly consolidated sediments exhibits distinctive relationships between these parameters. AVO attributes, together with other information, can help the interpreters to understand rock properties better than the use of only seismic stack sections.

## 1.1. ROCK PROPERTIES INSIDE AVO

The reflections recorded in the exploration are closely related to subsurface rock properties. The strongest amplitude variations with offsets in the seismic data very often are caused by hydrocarbon saturation in the rocks. The essence of the matter for AVO is in the fact that the shear modulus or rigidity ( $\mu$ ) of a rock does not change when the fluid saturation is changed. However, the bulk modulus ( $\kappa$ ) does change significantly when the fluid saturation is changed (Gassman, 1951). The bulk modulus of a brine-saturated rock is greater than that of gas-saturated rock because brine is significantly tighter than gas. These elastic constants are linked to seismic wave velocities as the following relationships:

$$V_P = \sqrt{\frac{\kappa + \frac{4}{3}\mu}{\rho}} = \sqrt{\frac{\lambda + 2\mu}{\rho}}, \quad (1.1)$$

where  $\lambda$  is incompressibility.

$$V_S = \sqrt{\frac{\mu}{\rho}}. \quad (1.2)$$

$V_p$  of a gas-saturated rock is significantly less than  $V_p$  for the same rock if it were brine-saturated. The  $S$  wave velocity of a gas-saturated rock is slightly higher than  $V_S$  for the same rock if it were brine-saturated because the density of gas is lower than the density of brine. The  $V_p/V_S$  ratio of gas-saturated rock may be substantially different therefore from the  $V_p/V_S$  ratio for the same rock if it were brine saturated.

Although the fluid saturation causes obvious AVO phenomena, the lithologic changes may also cause amplitude variations versus offset. The lithology difference is closely linked to the rock property difference. Studying the AVO caused by lithologic change or by gas contents has practical implications.

The lithologic changes and fluids filling pores in the rock cause AVO phenomena. Therefore, by studying the AVO phenomena, it is possible to extract the rock properties and fluid contents in rocks from seismic data. In the AVO analysis, various methods may be employed to extract the elastic parameters from seismic data.

## **1.2. THEORY BASIS OF AVO ANALYSIS**

So far, the principles, on which AVO analysis is based, is the plane wave propagation crossing the media interface with physical property difference. Plane wave assumption is a simplification of complex subsurface media. The Zoeppritz equations describe the plane wave propagation in the ideal media.. They describe the reflections of incident, reflected, and transmitted P and S waves on both sides of an interface. Although this group of equations has the exact solutions for reflection coefficients, the equations are so complex algebraically that it is difficult to intuitively grasp the physics in both media cross the reflection interface. Fortunately, Aki and Richards (1980) provided approximations for reflection coefficients. In most contexts, those approximations, with good accuracy, are simpler and more practical than the Zoeppritz equations and become the basis of AVO analysis. Based on Aki and Richards' approximation, many forms of simplifications of the Zoeppritz equation of  $P$ - $P$  reflection coefficient have appeared in the literature and industrial practice (Aki and Richards, 1980, Shuey, 1985, Parson, 1986, Smith and Gidlow, 1989, Verm and Hilterman, 1994). Each of these simplifications from difference angles links reflection amplitudes with variations of rock properties. In this thesis, some of these forms are reviewed and compared.

In AVO analysis, some practices concentrate on finding more sensitive indicators of hydrocarbons and on extracting and exploiting anomalous variations between seismic data and these sensitive parameters. Some authors (Goodway et al 1997) showed the advantages of converting velocity measurements to Lamé's moduli parameters ( $\lambda$  and  $\mu$ ) to improve identification indicator of reservoir zones. In this thesis, the extraction of Lamé's parameters is studied. And sensitivities of different combination of Lamé's parameters are compared. Because of the complex nature of rock properties, simple and meaningful empirical relationships between rock physical parameters are usually very helpful to solve the problem and find the anomaly. The linear relationship between  $P$  and  $S$  wave velocities is observed by Castagna et al (1985). The linear relationship provides good empirical guidance for the study of the rock property using seismic data. Based on the linear relationship (also called the mud-rock line), Smith and Gidlow (1987) define the "fluid factor",  $\Delta F$ , as the difference between observed  $\Delta V_P/V_{Pa}$  and the predicted  $\Delta V_P/V_{Pa}$  from  $\Delta V_S/V_{Sa}$ , which implies the anomaly caused by reservoir or lithologies. Using the "mud-rock line" (Castagna et al., 1985) they have

$$\Delta F = \frac{\Delta V_P}{V_{Pa}} - 1.16 \left( \frac{V_S}{V_P} \right) \frac{\Delta V_S}{V_{Sa}}, \quad (1.3)$$

where  $V_S/V_P$  is the background  $S$  and  $P$  wave velocity ratio which can be predicted by application of the mud-rock trend to the interval velocities obtained from conventional velocity analysis or regional sonic logs. The fluid factor uses the  $P$  and  $S$  wave reflectivity to evaluate the anomalies resulting from lithologic changes or fluid contents.

### 1.3. P-S AVO ANALYSIS

In seismic exploration, most of the practice focuses on single component exploration. The AVO studies concentrate on the  $P$  wave reflection. Although multi-component exploration has been done in many areas, the study of multi-component AVO is limited. Of course, the processing of data other than the vertical component remains a challenging procedure. The redundancy of multi-component AVO measurements is advantageous. Additional  $S$  wave information, such as reflection time ratios, normal incidence amplitude ratios and  $S$  wave move-out, further constrains the analysis. Given that the AVO phenomena translate the sharing of the energy of the incident compressible wave between the

compressible and converted reflections, observation of the converted mode AVO is rendered redundant. In practice, a few years of experience in  $P$ -mode AVO observations may lead to different conclusions. In some privileged areas, the AVO of compressible waves effectively provides the expected results. In most cases, single fold data are not pure enough to provide reliable amplitude measurements, and inevitably the result is doubtful. In such cases, study of the AVO of the converted mode can be advantageous: when it is compatible with the  $P$ - $P$  AVO, it confirms it, and when it is not, it denounces unreliable information. Therefore, in areas with converted wave exploration, it is beneficial to study the AVO of converted waves.

Aki and Richard (1980) provide an approximation of the  $P$ - $S$  reflection coefficient. A rough approximation linking  $P$ - $S$  reflection coefficient with pure  $SH$  reflection coefficient also exists (Frasier and Winterstein, 1993, Stewart, 1995). Because of the challenges in the processing of the actual radial component data that are mainly  $P$ - $S$  reflections, applications of  $P$ - $S$  reflection coefficient and AVO analysis rarely appear in the literatures and practice. A  $P$ - $S$  reflection coefficient approximation that is accurate, and which is a ready linking of seismic with rock property changes is most desirable. In this thesis, the accuracy of the  $P$ - $S$  reflection coefficient approximations is studied. The formats that can be used in the  $P$ - $S$  data AVO analysis are studied. The AVO extraction is applied on one radial component seismic dataset.

#### **1.4. WHAT'S COVERED IN THE THESIS**

This thesis is divided into five chapters with this first chapter forming an introduction. Chapter 2 covers the basic principles of offset dependent reflection as applied to hydrocarbon exploration and discusses the approximations of the converted wave reflection coefficient. Chapter 3 deals with the methodology of AVO analysis. In Chapter 3 various AVO analysis methods are reviewed; the sensitivities of physical parameters in AVO analysis are compared and the noise issue is explored. In Chapter 4 the AVO analysis applied to Blackfoot 3C-2D line data is considered. The mud-rock line, the linear relationship between  $P$  wave velocity and  $S$  wave velocity, is obtained from well logs in Blackfoot. Lamé's parameters are extracted from vertical component data.  $P$  wave reflectivity and  $S$  wave reflectivity are extracted from vertical component data, CMP gathers and CSP gathers, and the fluid factor is calculated from extracted  $P$  and  $S$  wave reflectivities.  $S$  wave reflectivity extracted from radial component data is compared with that which is extracted from vertical component data.

## CHAPTER 2 REFLECTIVITY DEPENDENT ON INCIDENT ANGLES

### 2.1. COMPRESSIONAL WAVE PROPAGATION

In seismic exploration, the seismic waves propagate across complex underground media. Various energy reflections, transmissions, conversions and attenuations occur within this process, which may not be described in exact terms, given the complex nature of the physical properties of earth media. Some understanding of the phenomena observed in the seismic exploration may be derived from the use of simplified model. A layered earth model is usually assumed in the study of AVO phenomena and the single reflection interface is investigated as a starting point. In the conventional seismic exploration, waves that are generated by a source and reflected from subsurface are usually regarded as compressional ( $P$ ) waves. The compressional wave propagation becomes the fundamental in the AVO analysis.

### 2.2. SNELL'S LAW

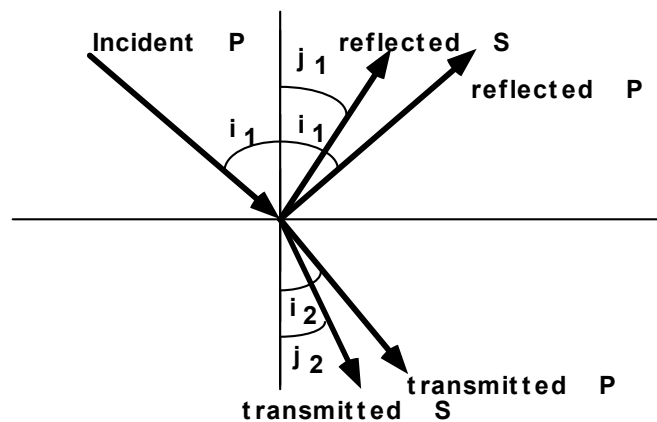


Figure 2.1. Waves generated by an incident P-wave at an interface between two infinite elastic half spaces.

When the compressional plane wave propagates across the media interface with different properties on both sides, the energy carried by the wave is reflected and transmitted in the form of compressional ( $P$ ) waves and converted shear ( $S$ ) waves.

Figure 2.1 illustrates the wave propagation of compressible wave at solid-solid interface between two infinite elastic half spaces. In Chapter 2, symbols are defined to follow the conventions of Aki and Richards (1980). The sine functions of the incident angle  $i_1$ , reflection angle  $i_1$  and  $j_1$ , and transmitted angles  $i_2$  and  $j_2$ , together with  $P$  wave velocities,  $\alpha_1$  and  $\alpha_2$ , and  $S$  wave velocities,  $\beta_1$  and  $\beta_2$ , of both sides, obey Snell's law as equation (2.1).

$$\frac{\sin(i_1)}{\alpha_1} = \frac{\sin(i_2)}{\alpha_2} = \frac{\sin(j_1)}{\beta_1} = \frac{\sin(j_2)}{\beta_2} = p, \quad (2.1)$$

where  $p$  is the ray parameter.

For the ideal interface and plane wave, Zoeppritz equations (Aki and Richard, 1980) describe the relationships among the incident waves, transmitted waves, and reflected waves. The Zoeppritz equations are described in Appendix A. In the solutions of Zoeppritz equations, the reflection coefficients are expressed as functions of incident, reflected, and transmitted angles and compressional and shear velocities and densities of both sides of the interface. Zoeppritz equations provide solution for any ideal plane wave propagation cases: 1) an incident  $P$  wave is converted into both reflected and transmitted  $P$  and  $S$  waves; 2) an incident  $S$  wave is converted into both reflected and transmitted  $P$  and  $S$  waves. In this thesis, only the reflected  $P$  wave and  $S$  wave from an incident  $P$  wave are studied.

## 2.3. AKI AND RICHARDS' APPROXIMATIONS

### 2.3.1. Simplified and meaningful equations

Although Zoeppritz equations have the exact solutions for reflection coefficients, it is not easy to directly apply Zoeppritz equations to the actual seismic data. One reason is that if the subsurface is to be solved from Zoeppritz equations, too many unknowns exist. Secondly, because of the complex nature of the earth, the seismic record is not composed of ideal reflected plane waves. Equations with a simple format and good accuracy are sought by researchers. Aki and Richards (1980) give approximations for reflection coefficients. These approximations are simpler and more practical than Zoeppritz equations. Equation (2.2) expresses the reflection coefficient for an incident

and reflected  $P$  waves. Equation (2.3) expresses the reflection coefficient for an incident  $P$  wave and reflected  $S$  wave. In these equations, Aki and Richards' conventions (1980) are followed. As shown on Figure 2.1,  $\alpha_1$ ,  $\beta_1$ , and  $\rho_1$  are  $P$  wave velocity,  $S$  wave velocity, and density of upper medium, while  $\alpha_2$ ,  $\beta_2$ , and  $\rho_2$  are  $P$  wave velocity,  $S$  wave velocity, and density of lower medium. The ray parameter  $p$  is defined by equation (2.1).

$$R_{PP} = \frac{1}{2}(1 - 4\beta^2 p^2) \frac{\Delta\rho}{\rho} + \frac{1}{2\cos^2 i} \frac{\Delta\alpha}{\alpha} - 4\beta^2 p^2 \frac{\Delta\beta}{\beta}. \quad (2.2)$$

$$R_{PS} = \frac{-p\alpha}{2\cos j} \left[ (1 - 2\beta^2 p^2 + 2\beta^2 \frac{\cos i}{\alpha} \frac{\cos j}{\beta}) \frac{\Delta\rho}{\rho} - (4\beta^2 p^2 - 4\beta^2 \frac{\cos i}{\alpha} \frac{\cos j}{\beta}) \frac{\Delta\beta}{\beta} \right]. \quad (2.3)$$

The elastic properties evident in the above equations are related as follows to those on each side of the interface:

$$\Delta\alpha = (\alpha_2 - \alpha_1), \quad (2.4.a)$$

$$\alpha = (\alpha_2 + \alpha_1)/2, \quad (2.4.b)$$

$$\Delta\beta = (\beta_2 - \beta_1), \quad (2.5.a)$$

$$\beta = (\beta_2 + \beta_1)/2, \quad (2.5.b)$$

$$\Delta\rho = (\rho_2 - \rho_1), \quad (2.6.a)$$

$$\rho = (\rho_2 + \rho_1)/2. \quad (2.6.b)$$

The angle  $i$  is the average of incident and transmitted P-wave angles, while  $j$  is the average of reflected and transmitted S-wave angles:

$$i = (i_1 + i_2)/2, \quad (2.7.a)$$

$$j = (j_1 + j_2)/2. \quad (2.7.b)$$

### 2.3.2. Ostrander's hypothetical gas sand model

Aki and Richards' approximations of reflection coefficients have good accuracy when the property contrasts and incident angles are small. The requirement of small property contrasts is generally satisfied in the real cases (usually less than 0.1). Ostrander (1984) devised a hypothetical gas sand model to analyze plane-wave reflection coefficients as a function of the angle of incidence and to test the accuracy of various approximations of reflection coefficients. Figure 2.2 shows Ostrander's model, a three-layer gas sand model with parameters that are typical for a shallow, young geologic section. Here, gas sand with a Poisson's ratio of 0.1 is embedded in shale having a Poisson's ratio of 0.4. There is a 20%  $P$  wave velocity reduction going into the sand, from 10,000 ft/s to 8,000 ft/s, a 10% density reduction from 2.40 g/cm<sup>3</sup> to 2.14 g/cm<sup>3</sup>, and a change of  $S$  wave velocity from 4082 ft/s to 5333 ft/s. The Poisson's ratio is changed to 0.4 if there is no gas in the sand layer, thus simulating the case of low-velocity brine-saturated young sandstone embedded in shale.

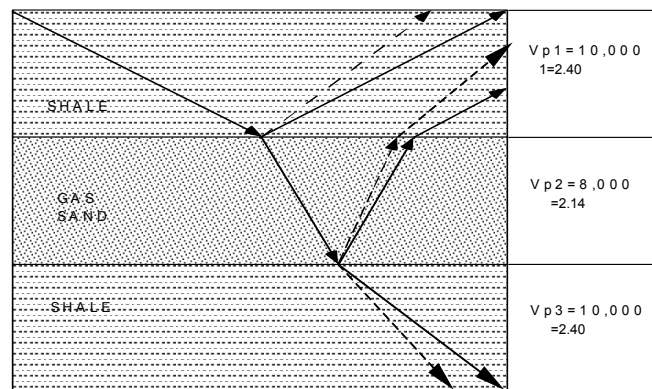


Figure 2.2. Three-layer hypothetical gas sand model (Ostrander, 1984)

### 2.3.3. Accuracy of Aki and Richards' approximations

Before applying the approximation on the real world, the accuracy of the approximation is tested. In Figure 2.3, the exact reflection coefficients as defined by Zoeppritz equation and approximated reflection coefficients are compared for the media with the elastic properties specified in Figure 2.2. The solid lines represent the exact reflection coefficients and the dash lines represent Aki-Richards' approximations of reflection coefficients. The cases without gas in the sand of the second layer as shown in

Figure 2.2 are also presented in Figure 2.3, using a Poisson ratio of 0.4. Panel (a) shows  $P$ - $P$  reflection coefficients for the two interfaces in Figure 2.2 and for two cases—one with and one without gas in the sand. Panel (b) shows  $P$ - $S$  reflection coefficients for the two interfaces in Figure 2.2 and for two cases—one with and one without gas in the sand. After comparing panel (a) and panel (b), the following points may be observed:

- At the normal incidence at the interface with elastic property variation,  $P$ - $S$  reflection coefficient is zero and  $P$ - $P$  reflection coefficient is not zero. This can be explained by the zero ray parameter at the normal incidence in equation (2.3) and by reference to the solution of Zoeppritz equation in Appendix A.
- In the small incident angle case, the magnitude of  $P$ - $P$  reflection coefficient is bigger than the magnitude of  $P$ - $S$  reflection coefficient. Correspondingly, the small ray parameter results in a small value of  $P$ - $S$  reflection at the small incident angles.
- Aki-Richards' approximation of  $P$ - $S$  reflection coefficient in equation (2.3) admits greater relative errors than the approximation of  $P$ - $P$  reflection coefficient, as exhibited in the model cases in Figure 2.2, especially those related to gas-filled sand.

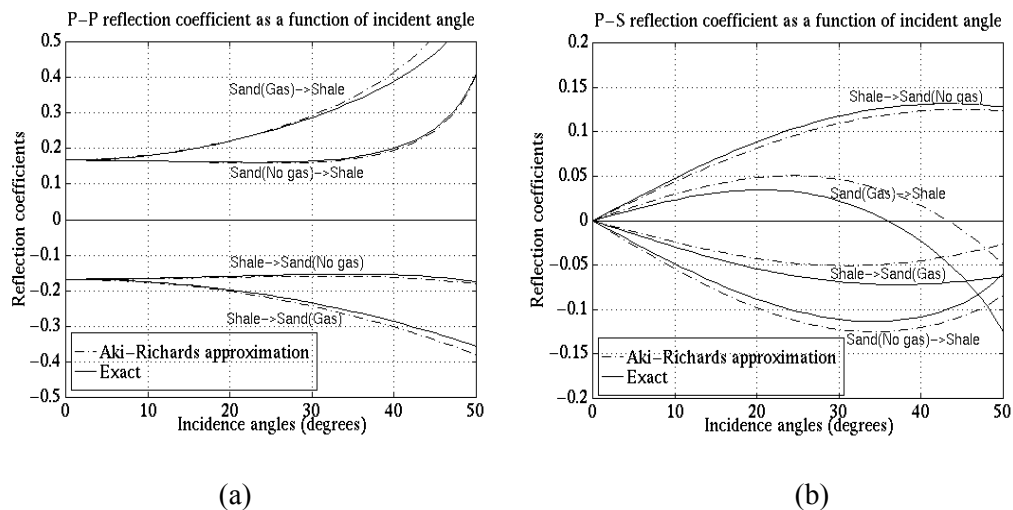


Figure 2.3. The exact and approximated reflection coefficients in the media with elastic properties specified in Figure 2.2. The solid lines are for the exact reflection coefficients and the dash lines are for Aki-Richards' approximations of reflection coefficients.

Many researchers have studied Aki-Richards' approximation of  $P$ - $P$  reflection coefficients. These approximations demonstrate sufficient accuracy for AVO analysis under certain assumption and conditions. In Chapter 3, some of these approximations of  $P$ - $P$  reflection coefficient will be reviewed and compared.

In seismic exploration, the reflected  $S$  wave energy from incident  $P$  waves is also recorded and utilized, especially in multi-component seismic exploration. The  $P$ - $S$  reflections exhibit different AVO nature from  $P$ - $P$  reflection. One of the topics in this thesis is studying the feasibility of extracting elastic wave information from  $P$ - $S$  reflection. The analysis methodologies of  $P$ - $P$  AVO analysis are applied to the  $P$ - $S$  data in the thesis. In the beginning, the approximation of  $P$ - $S$  reflection coefficients will be discussed. In the remainder of this chapter, the comparisons between approximations and the exact equation are made, along with a simpler approximation that is more insightful.

## 2.4. MORE ACCURATE APPROXIMATIONS OF $P$ - $S$ REFLECTION COEFFICIENT

### 2.4.1. Higher order truncation

One observation on the comparison between approximations of  $P$ - $S$  and  $P$ - $P$  reflection coefficients is made in section 2.3.3, saying that the relative errors in Aki-Richards' approximation of  $P$ - $S$  reflection coefficient equation are greater than errors in the approximation of  $P$ - $P$  reflection coefficient. The accuracy of the approximation of  $P$ - $S$  reflection coefficient will be studied in details in the following. At first, a more accurate approximation of  $P$ - $S$  reflection coefficient is to be derived from Zoeppritz equation, using the method by Aki and Richards of keeping higher order terms. In the derivation, the definitions in the equations (2.4.a), (2.4.b), (2.5.a), (2.5.b), (2.6.a), (2.6.b), (2.7.a), and (2.7.b) are used. Terms with higher order than  $(\frac{\Delta\alpha}{\alpha})^2, (\frac{\Delta\beta}{\beta})^2, \frac{\Delta\alpha}{\alpha} \frac{\Delta\beta}{\beta}, \frac{\Delta\alpha}{\alpha} \frac{\Delta\rho}{\rho}, \frac{\Delta\beta}{\beta} \frac{\Delta\rho}{\rho}$ , and  $(\frac{\Delta\rho}{\rho})^2$  are truncated. By expanding the exact reflection coefficient from Zoeppritz equations (see Appendix A), the higher order approximation for  $P$ - $S$  reflection coefficient is obtained as

$$R_{PS} = A \left[ C_1 \frac{\Delta\rho}{\rho} + C_2 \frac{\Delta\beta}{\beta} + D_1 \left( \frac{\Delta\rho}{\rho} \right)^2 + D_2 \left( \frac{\Delta\rho}{\rho} \frac{\Delta\alpha}{\alpha} \right) + D_3 \left( \frac{\Delta\rho}{\rho} \frac{\Delta\beta}{\beta} \right) + D_4 \left( \frac{\Delta\alpha}{\alpha} \frac{\Delta\beta}{\beta} \right) + D_5 \left( \frac{\Delta\beta}{\beta} \right)^2 \right] , \quad (2.8)$$

where

$$A = -\frac{1}{2} \frac{\sin i}{\cos j} ,$$

$$C_1 = 1 - 2 \sin^2 j + 2 \frac{\beta}{\alpha} \cos i \cos j ,$$

$$C_2 = -(4 \sin^2 j - 4 \frac{\beta}{\alpha} \cos i \cos j) ,$$

$$D_1 = \frac{1}{2} - 3 \sin^2 j - \frac{\beta}{\alpha} \cos i \cos j - 4 \frac{\beta}{\alpha} \sin^2 j \cos(i - j) ,$$

$$D_2 = \frac{1}{2} \tan^2 i \cos 2j - \frac{\beta}{\alpha} \cos i \cos j ,$$

$$D_3 = \frac{1}{2} + 16 \frac{\beta}{\alpha} \sin^2 j \cos(i - j) - \frac{\beta}{\alpha} \frac{\cos i}{\cos j} (1 + \cos^2 j) - 7 \sin^2 j ,$$

$$D_4 = -2 \tan^2 i \sin^2 j - 2 \frac{\beta}{\alpha} \cos i \cos j ,$$

and

$$\boxed{\phantom{0}} .$$

In the derivation, the assumption of small physical properties is made.

#### 2.4.2. Comparisons of various expressions using models

Using the model in Figure 2.2, the accuracy of equation (2.8) is compared with the accuracy of the Zoeppritz equation and Aki-Richards' approximation equation (2.3). In Figure 2.4, the reflection coefficients and relative errors of approximations versus incident angles are plotted. The velocities and densities for the model in Figure 2.2 are used to calculate the  $P$ - $S$  reflection coefficients. Figure 2.4 demonstrates that the higher

order approximation is much more accurate than Aki-Richard's approximation for the model Ostrander defined.

In the AVO analysis, the simplest expressions are pursued to enhance robustness of analysis, to lend stronger physical meaning to the expressions and to expedite the extraction of information from seismic data. In this thesis, several expressions of approximations of  $P$ - $S$  reflection coefficient are reformatted. Because Aki-Richards' approximation is the first order approximation in terms of physical property contrasts, its format is much simpler than higher order approximation, although Aki-Richards' approximation is not as accurate as higher order approximations. Aki-Richards' approximation can be reformatted into simpler formats. In the following, two-term equation is pursued, because the stability of the AVO analysis is closely related to the number of unknowns. More unknowns, less stable, given the current acquisition geometry and noise level. The two-term approximation is usually preferred by AVO analysis.

Aki-Richard's approximation in equation (2.3) can be rewritten as polynomials of  $\cos(i+j)$ , or  $\sin^2 j$  as equation (2.9) and equation (2.10).

$$R_{PS} = A[P_0 + P_1 \cos(i + j)] \quad (2.9)$$

where

$$A = -\frac{\sin i}{2 \cos j} = -\frac{1}{2} \frac{\alpha}{\beta} \tan j, \quad P_0 = \frac{\Delta \rho}{\rho}, \quad P_1 = 2 \frac{\beta}{\alpha} B, \quad \text{and} \quad B = \frac{\Delta \rho}{\rho} + 2 \frac{\Delta \beta}{\beta}.$$

If we notice that  $\frac{\Delta \mu}{\mu} = \frac{\Delta \rho}{\rho} + 2 \frac{\Delta \beta}{\beta}$ , when  $\mu$  is shear modulus, equation (2.9) can

be expressed as an equation with clear physical meaning if  $\frac{\beta}{\alpha} \approx \frac{1}{2}$ , i.e.,

$$R_{PS} \approx A \left[ \frac{\Delta \rho}{\rho} + \frac{\Delta \mu}{\mu} \cos(i + j) \right]. \quad (2.9.a)$$

With Snell's law and truncation after  $\sin^4 j$ , equation (2.9) is expanded as:

$$R_{PS} = A[C_0 + C_1 \sin^2 j + C_2 \sin^4 j] \quad (2.10)$$

where

$$C_0 = \frac{\Delta\rho}{\rho} + 2\frac{\beta}{\alpha}B, \quad C_1 = -\frac{\beta}{\alpha}B\left(\frac{\alpha}{\beta} + 1\right)^2, \quad \text{and} \quad C_2 = -\frac{1}{4}\frac{\beta}{\alpha}B\left(\frac{\alpha^2}{\beta^2} + 1\right)^2.$$

Further approximation of equation (2.10) may be obtained by dropping the  $\sin^4 j$  term to give the equation (2.11), and the accuracy of the latter equation equals to that of equation (2.10) for the small and intermediate incident angles.

$$R_{PS} = A(C_0 + C_1 \sin^2 j). \quad (2.11)$$

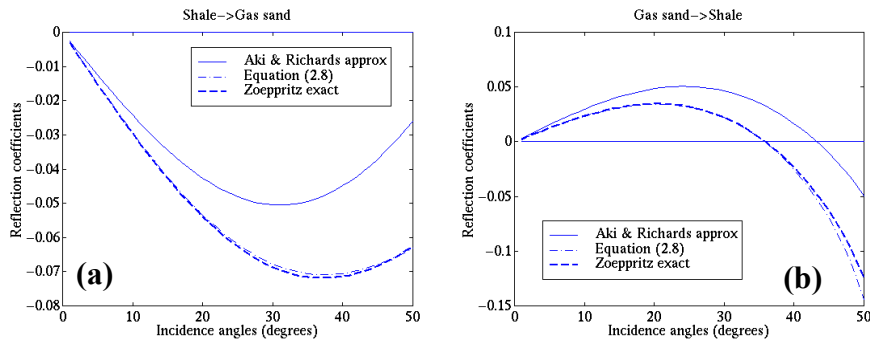
If we expand term  $A$  in equation (2.11) in terms of  $\sin j$ , we obtain:

$$R_{PS} = D_1 \sin j + D_2 \sin^3 j, \quad (2.12)$$

where

$$D_1 = -\frac{1}{2}\frac{\alpha}{\beta}C_0 \quad \text{and} \quad D_2 = -\frac{1}{2}\frac{\alpha}{\beta}\left(\frac{1}{2}C_0 + C_1\right).$$

Equation (2.9) is the rearranged format from Aki-Richards' approximation. Equations (2.10), (2.11), and (2.12) are further approximated by dropping the smaller term after expanding Aki-Richards' approximation as a polynomial of sine functions of incident angles. The accuracy of equations (2.10), (2.11), and (2.12) are comparable with Aki-Richards' approximation. Figure 2.5 shows the comparisons of equations (2.10), (2.11), and (2.12), Aki-Richards' approximation, and the Zoeppritz equations.



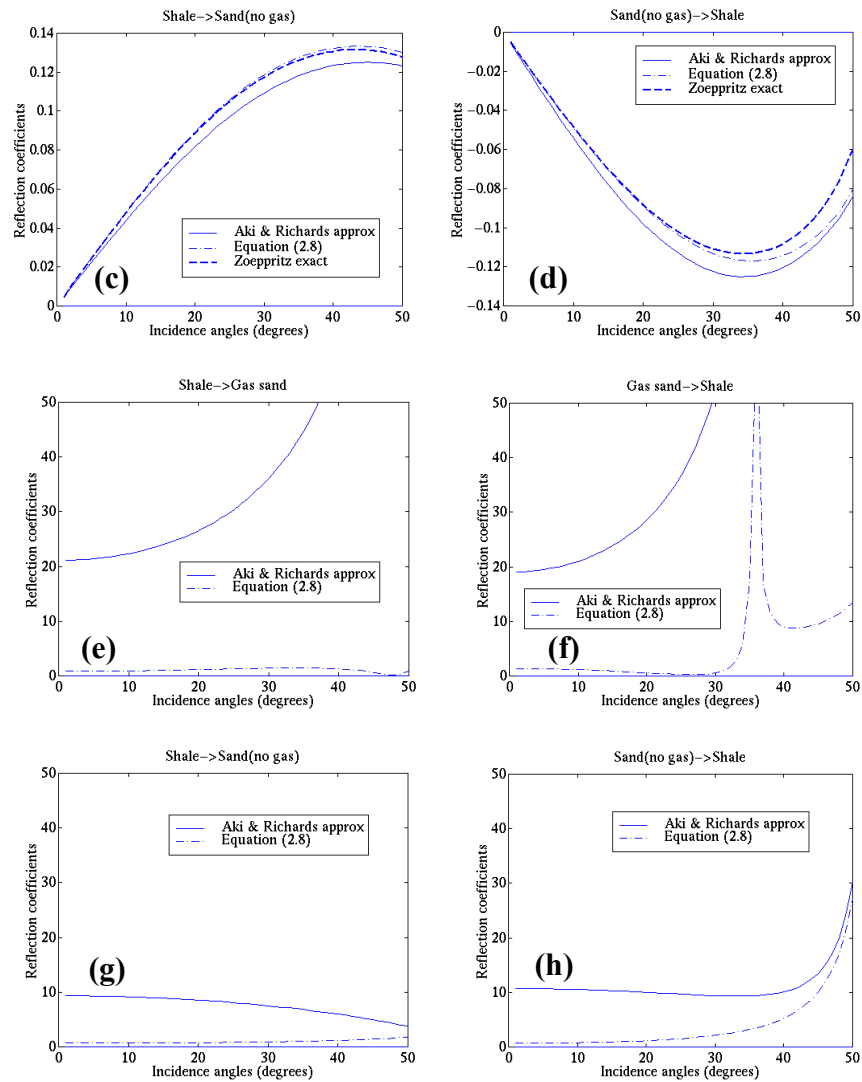


Figure 2.4. Comparisons of the exact  $P$ - $S$  reflection coefficients, Aki-Richards approximation (2.3), and equation (2.8), for the three-layer sand model in Figure 2.2. The reflection coefficients versus incident angles are indicated in (a), (b), (c), and (d). The relative errors expressed as percentages versus incident angles are indicated in (e), (f), (g), and (h).

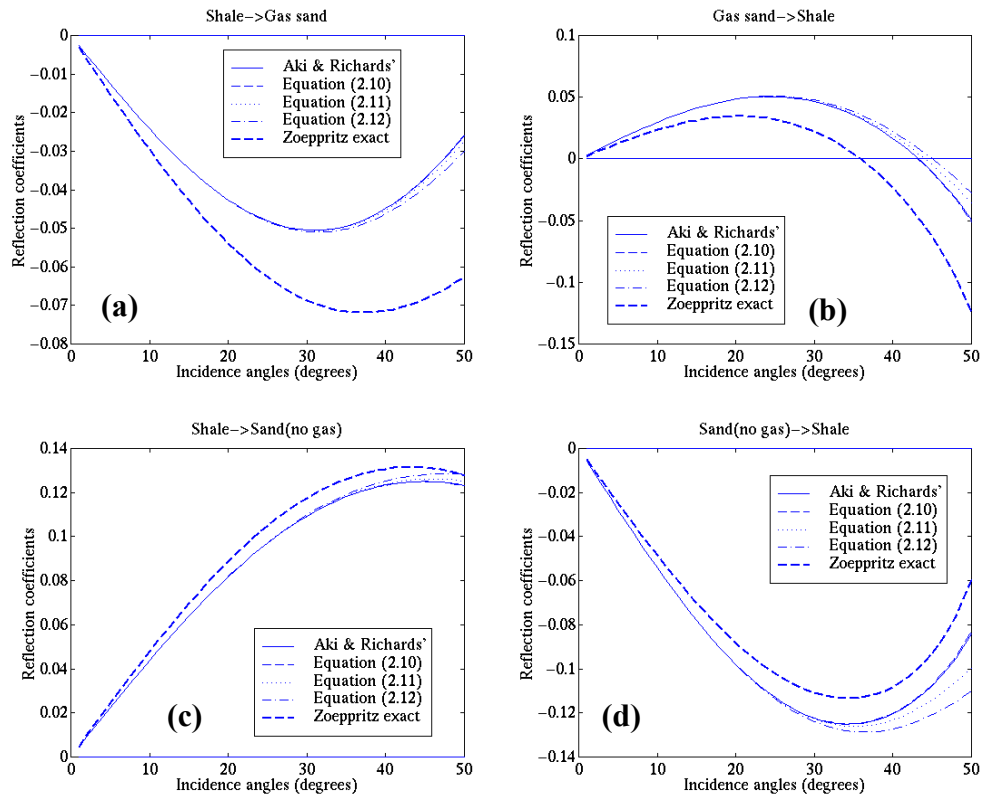


Figure 2.5. Comparisons of the exact  $P$ - $S$  reflection coefficients, Aki-Richards' approximation (2.3), equations (2.10), (2.11), and (2.12), for the three-layer sand model in Figure 2.2. On each panel, the curve for equation (2.10) overlaps with the curve for Aki-Richards' approximation, due to the close accuracies of both.

### 2.4.3. Corrections of the first order approximations

Comparing the curves in Figure 2.4 and Figure 2.5 demonstrates that the Aki-Richards' approximations of  $P$ - $S$  reflection coefficient as equation (2.3) or equations (2.9) – (2.12) contain significant errors for the models. Figure 2.6 compares equation (2.3) with equation (2.8) having been divided by  $\tan j$  to emphasize the main difference in the approximation. Plotting in this manner shows that the error in Aki-Richards' approximation induces similar errors for different incident angles. The accuracy of Aki-Richards' approximation may, however, be improved by correcting  $P_0$  in equation (2.9) or  $C_0$  in equation (2.10). If  $P_0$  or  $C_0$  is corrected using equation (2.8), the approximations are rendered more accurate. Equation (2.13) and equation (2.14) demonstrate the corrected formulas of equation (2.9) and equation (2.10).

$$R_{PS} = A[P_0 + P_1 \cos(i + j)], \quad (2.13)$$

where

$$A = -\frac{\sin i}{2 \cos j} = -\frac{1}{2} \frac{\alpha}{\beta} \tan j,$$

$$P_0 = \frac{\Delta\rho}{\rho} (1 + R_{ss}) - 2 \frac{\beta}{\alpha} B R_{pp},$$

$$P_1 = 2 \frac{\beta}{\alpha} B,$$

$$R_{s0} = \frac{1}{2} \left( \frac{\Delta\rho}{\rho} + \frac{\Delta\beta}{\beta} \right),$$

$$R_{p0} = \frac{1}{2} \left( \frac{\Delta\rho}{\rho} + \frac{\Delta\alpha}{\alpha} \right),$$

and

$$B = \frac{\Delta\rho}{\rho} + 2 \frac{\Delta\beta}{\beta} = 2R_{s0} + \frac{\Delta\beta}{\beta}.$$

$$R_{PS} = A[C_0 + C_1 \sin^2 j + C_2 \sin^4 j] \quad (2.14)$$

where

$$C_0 = \frac{\Delta\rho}{\rho} (1 + R_{ss}) + 2 \frac{\beta}{\alpha} B (1 - R_{pp}),$$

$$C_1 = -\frac{\beta}{\alpha} B \left( \frac{\alpha}{\beta} + 1 \right)^2, \text{ and } C_2 = -\frac{1}{4} \frac{\beta}{\alpha} B \left( \frac{\alpha^2}{\beta^2} + 1 \right)^2.$$

In Figure 2.7, equation (2.13) and equation (2.14) are compared with Aki-Richards' approximation, equation (2.8), and Zoeppritz equation. It can be seen that equations (2.13) and (2.14) are closer to the exact than Aki-Richards' approximation.

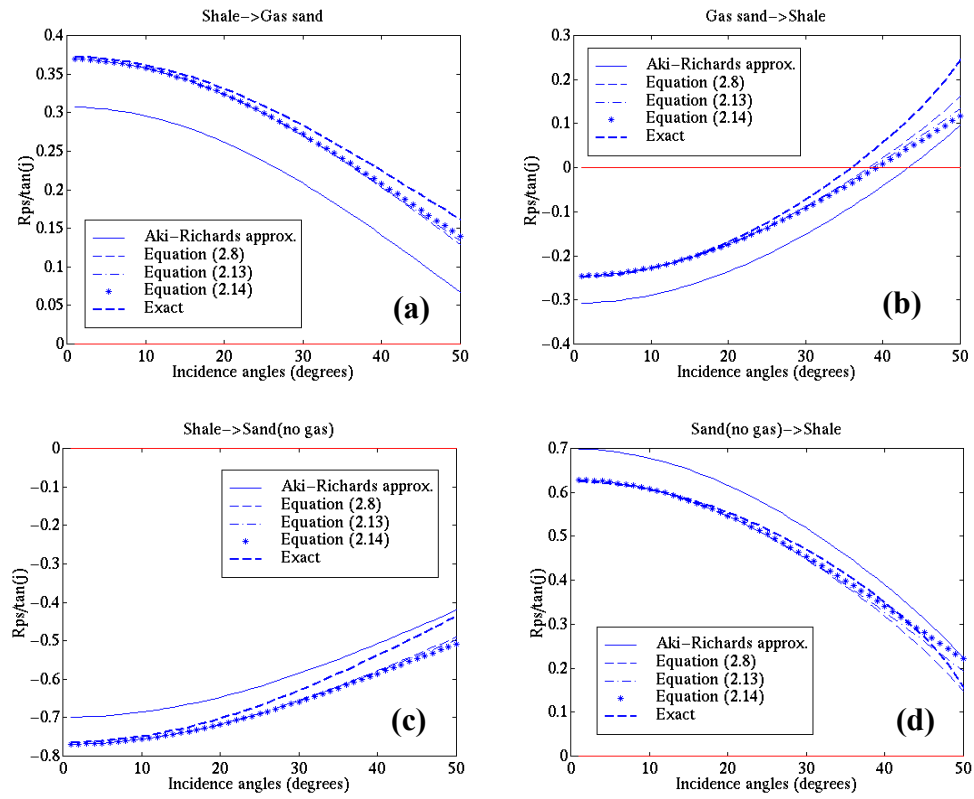


Figure 2.6. Plots of equations (2.3), (2.8), (2.13) and (2.14) after division by  $\tan j$  versus incident angle.

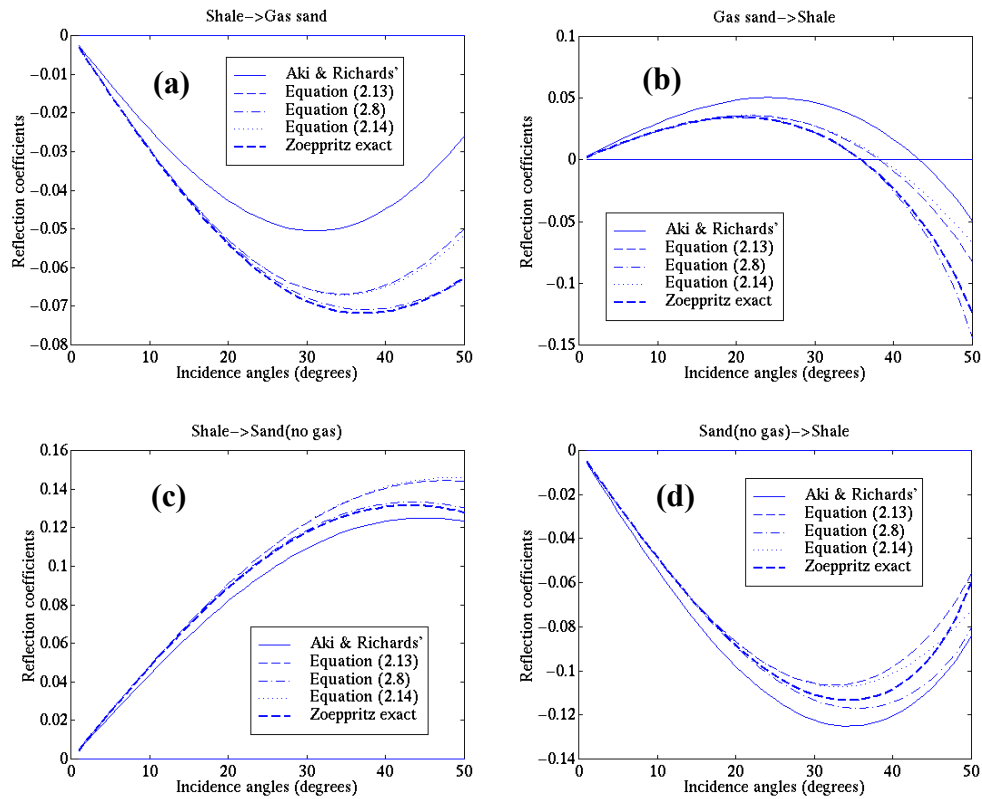


Figure 2.7. Comparisons of the exact  $P$ - $S$  reflection coefficients, Aki-Richards' approximation (2.3), equation (2.8), equation (2.13) and equation (2.14) for the three-layer sand model in Figure 2.2.

#### 2.4.4. Comparisons using other models

The model used in Figure 2.2 is a young gas sand model with sizeable  $S$  wave property change at the interface. In Table 2.1 another gas sand model with properties of overburden shale and gas sand is investigated.

Table 2.1. Property of second gas sand model.

	Vp (m/s)	Vs (m/s)	Density (g/cc)	Poisson's ratio
Shale	3811	2263	2.40	0.363
Gas sand	3453	2302	2.10	0.10

Figure 2.6 shows the comparison of approximations and exact reflection coefficients for the model in Table 2.1. The Aki-Richards' approximation exhibits good accuracy for this model in which shear wave velocities demonstrate smaller changes.

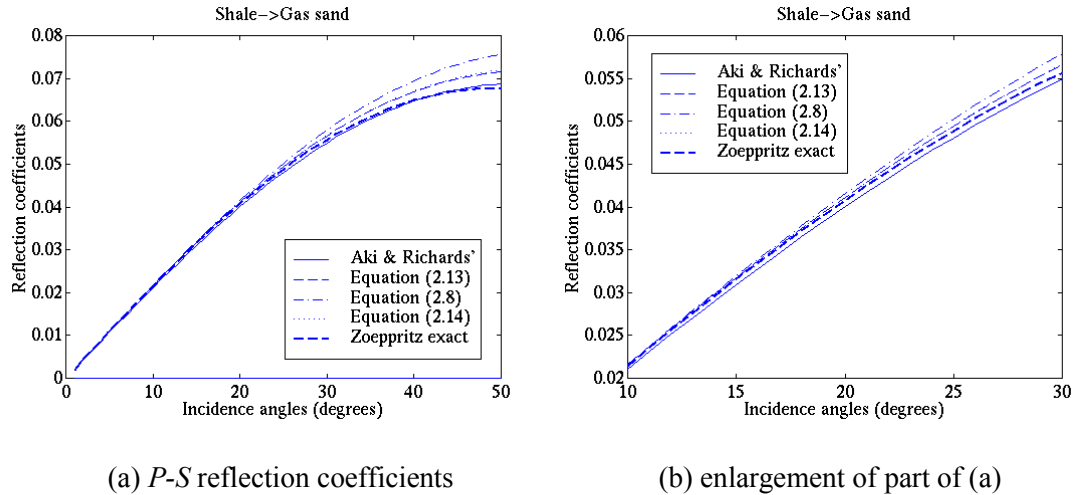


Figure 2.8. Comparison of the approximations and exact  $P$ - $S$  reflection coefficients for gas sand model in Table 2.1.

Errors of Aki-Richards' approximation are tested by the real well logs, which are closed to real cases. The average relative errors of Aki-Richards' approximation for  $P$ - $S$  reflection coefficients on the interfaces of the macro layers extracted from one well in the Blackfoot area studied in the thesis, which is mentioned in Chapter 1 and studied in Chapter 4, are calculated and shown on Figure 2.9, given the incident angle range of 1-40 degrees. With the exception of the top of Mississippian at 1615m, most of the relative errors are less than 10%, the biggest being 7.5%.

Although the Aki-Richards' approximation of  $P$ - $S$  reflection coefficient contains significant errors with sizeable physical property contrasts, as in the unconsolidated gas sand model, the Aki-Richards' approximation, as the function of the first order of property contrasts, provides a practical format for the general cases. Noises and other factors involved in the AVO analysis should be, however, taken into considerations to enhance the accuracy of the approximation. The Aki-Richards' approximation of  $P$ - $S$  reflection coefficients can also be regarded as good for the small incident angles and small  $S$  wave property changes. The error of this approximation would be acceptable for

a large number of cases in the real world. Care should be taken in special cases for studies, which depend on the accuracy of the approximations.

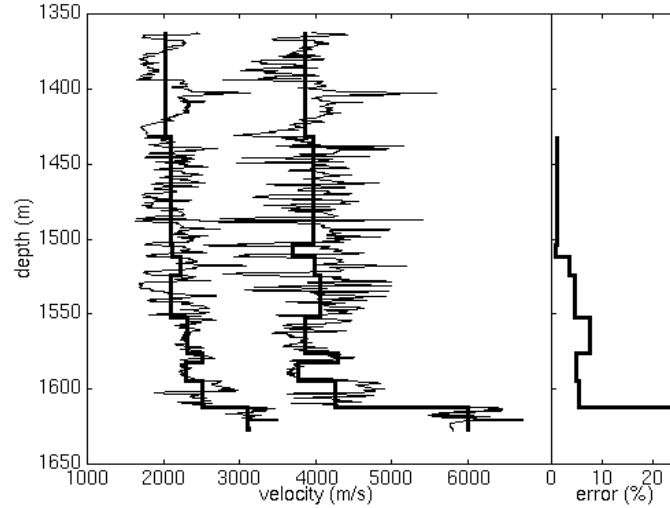


Figure 2.9. The average relative error of Aki-Richards' approximation for the macro layers from well logs (Blackfoot 0808 well).

## 2.5. RELATIONSHIP BETWEEN $R_{PS}$ AND $R_{SS}$

Stewart (1995) showed an approximate relationship between converted-wave reflectivity  $R_{PS}$  and pure  $S$  reflectivity  $R_{SS}$ . The equation that approximates the pure  $S$  reflectivity is given (Aki and Richards, 1980) as:

$$R_{SS} = -\frac{1}{2}(1 - 4\beta^2 p^2) \frac{\Delta\rho}{\rho} - \left(\frac{1}{2\cos^2 j} - 4\beta^2 p^2\right) \frac{\Delta\beta}{\beta}, \quad (2.15)$$

and the relationship between converted-wave reflectivity  $PS$  and pure  $S$  reflectivity  $SS$  is as:

$$R_{PS} = -\frac{p\alpha}{2\cos j} \left[ -8\frac{\beta}{\alpha} R_{SS} + \left(1 - 2\frac{\beta}{\alpha}\right) \frac{\Delta\rho}{\rho} \right]. \quad (2.16)$$

Now in areas where  $\frac{\beta}{\alpha} \sim \frac{1}{2}$ , the second term in the equation (2.16) is very small,

and

$$R_{PS} \approx 4 \tan j R_{SS}. \quad (2.17)$$

With the hypothetical model in Figure 2.2, the exact  $P$ - $S$  reflection coefficients, Aki-Richards' approximations and higher order approximation--equations (2.8) and (2.16) are compared. Figure 2.10 shows comparisons of the  $P$ - $S$  reflection coefficients of equations (2.3), (2.8), and (2.16) as a function of incident angle. The gas sand model in Table 1 is also used to test the equation (2.16), the comparison being shown in Figure 2.9. Equation (2.16) is generally as accurate as Aki-Richards' approximation except the extreme cases.

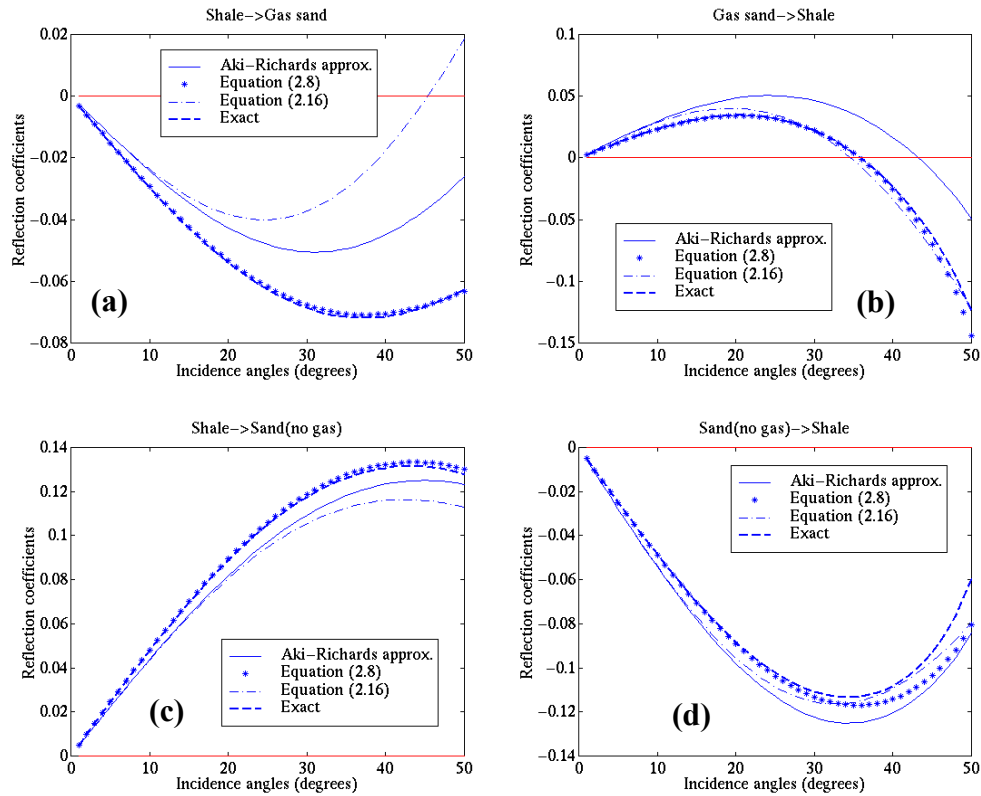


Figure 2.10. Comparisons of  $P$ - $S$  reflection coefficients in equation (2.8), Aki-Richards approximation--equations (2.3), (2.8), and (2.16)--relationship between  $P$ - $S$  and  $S$ - $S$ . The four panels demonstrate the  $P$ - $S$  reflection coefficients versus angle of incidence for the three-layer sand model in Figure 2.2.



# CHAPTER 3      **METHODOLOGY OF AVO**

## **ANALYSIS**

### **3.1. METHODS OF AVO ANALYSIS**

In seismic exploration, reflections are recorded as they arrive at the earth's surface at many source-receiver offset distances. A comparison of the amplitudes of these reflections leads to the expression "Amplitude Variation with Offsets" (AVO). Larger incident angles result from farther offsets. The recorded amplitudes closely relate to reflection coefficients of the subsurface interfaces and the offsets may be closely linked to the incident angles of the wave propagation. Since the reflection amplitudes depend on the incident angles, and the physical parameter changes, the physical parameters may be estimated from the seismic records.

When the compressional  $P$  waves descending from a typical source strike a reflective rock interface at a particular angle, a portion of the incident  $P$  wave energy is converted to a shear  $S$  wave.  $P$  and  $S$  waves are, subsequently, striking reflective rock surfaces and traveling through rock layers. Of greatest interest is the fact that  $P$  and  $S$  waves have different sensitivities to pore fluids. Upon the introduction of only a small amount of air or gas into the pore spaces of a rock,  $P$  waves may travel at a significantly reduced velocity. In contrast,  $S$  waves generally do not depend on the pore spaces of a rock, and travel via the rock framework, and are unaffected by gas or water filling the pore spaces producing little variation in velocity.

The different behavior of  $P$  and  $S$  waves, when gas is present in the pore spaces, makes AVO useful as a direct hydrocarbon indicator in clastic rocks. A change in amplitude on the far offsets, relative to the near offsets may be observed on the seismic data in the form of e.g. a peak that brightens or dims with offset. A wide range of AVO responses is possible, depending on the geologic setting of the reservoir. Of most importance is the contrast between a gas sand and the encasing medium.

Detecting gas sand is the most promising application of AVO analysis. Gas sands with low  $V_p/V_s$  ratio as a character may be differentiated from other subsurface layers with low impedance such as coals and porous brine sands. The success of AVO is indicated in a  $V_p/V_s$  ratio change. Lithology discrimination may be achieved by inspecting  $V_p$  and  $V_s$  trend curves. For example, an incised sand channel has low  $V_p/V_s$  ratio, while other lithology present higher  $V_p/V_s$  ratio, therefore, to be delimited by AVO analysis.

AVO analysis solves the inverse problem of wave propagation. The lithology change or hydrocarbon saturation causes the amplitude variation with offsets recorded by seismic data. AVO analysis attempts to solve the lithology or saturation fluid. Zoeppritz equation tells one the reflection coefficient for a given set of physical parameters. The AVO analysis starts from Zoeppritz and extracts the physical parameters, using the information of seismic data.

### **3.1.1. Various AVO extraction methods**

Zoeppritz equation describes the relations of the incident, reflected and transmitted compressional and shear waves on both sides of an interface. A simpler equation is desired to relate the amplitude of a reflected  $P$  wave with the amplitudes of incident  $P$  wave amplitudes as a function of the angle of incidence. Aki and Richards (1980) provide such an equation, containing the following assumptions: the relative changes of property are sufficiently small; second-order terms can be neglected; and the incident angle does not approach the critical angle. These are reasonable assumptions for most reflection seismic surveys. Various researchers have re-arranged and simplified the Aki and Richards' approximation to solve something they believe to be geologically or geometrically meaningful.

The equations used by researchers in the AVO analysis have different emphases, and exhibit their own assumptions and limitations. In the following, some approximations of Zoeppritz equations for  $P$ - $P$  reflection coefficient are listed. The first users, solutions, assumptions and limitations are summarized. In the descriptions of the equations, symbols are used as the conventions in the publications and their meanings will be

defined when used first time. In all equations  $\theta$  is the average of incident and transmitted angles of P waves.

### 3.1.1.1. Shuey's simplification of Zoeppritz equation

Shuey (1985) presented a form of the Aki and Richards' approximation

$$R_{PP}(\theta) \approx R_{P0} + \left( A_0 R_{P0} + \frac{\Delta\sigma}{(1-\sigma)^2} \right) \sin^2 \theta + \frac{1}{2} \frac{\Delta V_P}{V_P} (\tan^2 \theta - \sin^2 \theta), \quad (3.1)$$

where  $R_{P0}$  is the normal incidence reflection coefficient,  $\sigma$  is Poisson's ratio, and  $A_0$  is given by

$$A_0 = 2(1 + B_0) \left( \frac{1 - 2\sigma}{1 - \sigma} \right)$$

and

$$B_0 = \frac{\frac{\Delta V_P}{V_P}}{\frac{\Delta V_P}{V_P} + \frac{\Delta\rho}{\rho}}.$$

The advantage of this form is that each term describes a different angular range of the offset curve. The first term in equation (3.1) is the normal incidence reflection coefficient, the second term predominates at intermediate angles, and the third term is dominant as the critical incidence is approached. Thus, for restricted angles of incidence far away from critical incidence, we drop the third term, giving an equation that is linear in  $\sin^2 \theta$ .

$$R_{PP}(\theta) \approx R_{P0} + B \sin^2 \theta. \quad (3.2)$$

$B$  in this equation is often called the "AVO gradient".  $R_{P0}$  is the normal incident  $P$  wave reflectivity. Equation (3.2) is accurate for a certain range of incident angles, usually up to 25 degrees, but unstable for use beyond this angle. In its application, it is often assumed to be  $V_P/V_S \sim 2$ . Normal incident  $S$  wave reflectivity  $R_{S0}$  can therefore be solved as

$$R_{S0} = \frac{1}{2}(R_{P0} - B)$$

### 3.1.1.2. Hilterman's approximation

Hilterman (1989) rearranged Shuey's equation to another convenient approximation to solve for delta Poisson ratio reflectivity.

$$R_{PP}(\theta) = R_{P0} \cos^2 \theta + \frac{\Delta\sigma}{(1-\sigma)^2} \sin^2 \theta. \quad (3.3).$$

The delta Poisson's ratio reflectivity in equation (3.3) has the following relationship:

$$\frac{\Delta\sigma}{(1-\sigma)^2} = 8 \left( \frac{V_S}{V_P} \right)^2 (R_{P0} - R_{S0}),$$

where  $R_{P0}$  and  $R_{S0}$  are the normal incident reflectivities of  $P$  and  $S$  waves respectively.

Equation (3.3) is based on Shuey's equation. It assumes  $V_P/V_S \sim 2$  and ignores big incident angles. The Poisson's ratio changes, which may indicate fluid contents or lithology changes, are emphasized.

### 3.1.1.3. Smith & Gidlow's weight stack method

Smith and Gidlow (1987) reduce Aki-Richards' approximation to a two-term equation as in equation (3.4). In the derivation, an exponential relationship like Gardner's empirical relationship between  $P$  wave velocity and density is used to convert the term of density change to that of  $P$  wave velocity change.

$$R_{PP}(\theta) = \frac{1}{2} \left[ (1 + \tan^2 \theta) + g \left( 1 - 4 \left( \frac{V_S}{V_P} \right)^2 \sin^2 \theta \right) \right] \frac{\Delta V_P}{V_P} - 4 \left( \frac{V_S}{V_P} \right)^2 \sin^2 \theta \frac{\Delta V_S}{V_S}, \quad (3.4)$$

where  $g$  is 0.25, if Gardner's empirical relationship between density and velocity is used as

$$\rho = a V_P^g.$$

Smith and Gidlow also introduce a computationally simple procedure for conducting the data fitting, achieved by a weighted stacking of the traces in the CMP gather. The two sets of weights to be applied to the samples of the CMP gather traces (to produce the  $P$  and  $S$  reflectivity traces) are computed from the  $V_p/V_s$  ratio function, the angles of incidence and fold. The weights vary with offsets and times. The NMO-corrected traces in a CMP gather are multiplied by the weights and summed. This weighting and stacking is done using the  $P$  wave solution weights and the  $S$  wave solution weights. The resulting traces are the zero offset  $P$  wave reflection trace and the zero offset  $S$  wave reflection trace, where the two-way times of the events are the  $P$  wave two-way times.

Equation (3.4) has physical meaning with the separation of  $P$  and  $S$  wave velocity changes. In addition, it is applicable for any incident angle before critical incidence. However, the exponential relationship between  $P$  wave velocity and density in many cases has poor confidence. As a result, equation (3.4) may exhibit sizeable error at small incident angles.

#### 3.1.1.4. Fatti et al.'s method

Aki-Richards' approximation is rearranged into equation (3.5) by Fatti et al (1994).

$$R_{PP}(\theta) = \frac{1}{2}(1 + \tan^2 \theta) \frac{\Delta I_p}{I_p} - 4 \left(\frac{V_s}{V_p}\right)^2 \sin^2 \theta \frac{\Delta I_s}{I_s} - \left[\frac{1}{2} \tan^2 \theta - 2 \left(\frac{V_s}{V_p}\right)^2 \sin^2 \theta\right] \frac{\Delta \rho}{\rho} \quad (3.5)$$

After the third term in equation (3.5) is dropped, equation (3.6) is obtained (Fatti et al., 1994). Equation (3.6) is very good approximation comparable with equation (3.5). The third term in equation (3.5) is much smaller than the other two terms because 1)  $\sin(\theta) \sim \tan(\theta)$  at the small incident angle;  $V_p/V_s$  is close to 2; and 2) density change relative to density absolute value is not as significant as  $P$  velocity change and  $S$  velocity change.

$$R_{PP}(\theta) = \frac{1}{2}(1 + \tan^2 \theta)^2 \frac{\Delta I_P}{I_P} - 4 \left( \frac{V_S}{V_P} \right)^2 \sin^2 \theta \frac{\Delta I_S}{I_S} \quad (3.6)$$

Equations (3.5) and (3.6) have no incident angle limitation, and, for most cases they are reasonably accurate for angles up to critical incidence.

### 3.1.1.5. *Lame's parameters extraction*

Goodway et al. (1997) examined the sensitivity analysis of Lamé's parameters (incompressibility-- $\lambda$  and shear modulus-- $\mu$ ) to the presence of hydrocarbon and concluded that incompressibility ( $\lambda$ ) and ratio of incompressibility and shear modulus ( $\mu$ ) are all very sensitive to hydrocarbon saturation. To obtain this type of information from seismic data,  $P$  and  $S$  wave reflectivities are extracted from AVO responses using equation (3.6), the reflectivities are inverted to the impedance using well sonic log as constraints, and  $\lambda/\mu$  is calculated from the relationships between Lamé's parameters and impedance. These relationships are summarized in the following.

$$V_P = \sqrt{\frac{\lambda + 2\mu}{\rho}}$$

$$V_S = \sqrt{\frac{\mu}{\rho}}$$

$$I_P^2 = (V_P \rho)^2 = (\lambda + 2\mu)\rho$$

$$I_S^2 = (V_S \rho)^2 = \mu\rho$$

$$\boxed{\lambda\rho = I_P^2 - 2I_S^2}$$

$$\boxed{\mu\rho = I_S^2}$$

$$\boxed{\lambda/\mu = (\lambda\rho)/(\mu\rho) = (I_P^2 - 2I_S^2)/(I_S^2)}$$

Usually, the gas sand exhibits low  $\lambda\rho$  and  $\lambda/\mu$  ratio.

### 3.1.1.6. Xu and Bancroft's extraction

Xu and Bancroft (1997, 1998) derived equations (3.7) and (3.8) (see Appendix B) from Aki-Richards' approximation and used it to directly extract Lamé's parameters from seismic. The equations are:

$$R_{pp}(\theta) = \frac{1}{4}(1 + \tan^2 \theta) \frac{\Delta(\lambda + 2\mu)}{(\lambda + 2\mu)} - \sin^2 \theta \frac{\Delta 2\mu}{(\lambda + 2\mu)} + \frac{1}{4}(1 - \tan^2 \theta) \frac{\Delta \rho}{\rho} \quad (3.7)$$

$$R_{pp}(\theta) = \frac{1}{4}(1 + \tan^2 \theta) \frac{\Delta(\kappa + \frac{4}{3}\mu)}{(\kappa + \frac{4}{3}\mu)} - \sin^2 \theta \frac{\Delta 2\mu}{(\kappa + \frac{4}{3}\mu)} + \frac{1}{4}(1 - \tan^2 \theta) \frac{\Delta \rho}{\rho} \quad (3.8)$$

Equations (3.7) and (3.8) have no explicit  $V_p/V_s$  requirements making them different from other extraction methods. To make the extraction stable, both equations have to be approximated into two term equations. The density term in both equations can be incorporated into other two terms using the Gardner's velocity-density relationship allowing the density term to be dropped.

$\frac{\Delta(\lambda + 2\mu)}{\lambda + 2\mu}$  and  $\frac{\Delta\mu}{\lambda + 2\mu}$  or  $\frac{\Delta(\kappa + \frac{4}{3}\mu)}{\kappa + \frac{4}{3}\mu}$  and  $\frac{\Delta\mu}{\kappa + \frac{4}{3}\mu}$  are extracted from seismic data.  $\frac{\Delta\lambda}{\lambda + 2\mu}$  can be calculated by  $\frac{\Delta(\lambda + 2\mu)}{\lambda + 2\mu} - \frac{2\Delta\mu}{\lambda + 2\mu}$ ;  $\frac{\Delta\kappa}{\kappa + \frac{4}{3}\mu}$  can be calculated by

$\frac{\Delta(\kappa + \frac{4}{3}\mu)}{\kappa + \frac{4}{3}\mu} - \frac{4}{3} \frac{\Delta\mu}{\kappa + \frac{4}{3}\mu}$ . The following two equations can be used to extract  $\frac{\Delta\lambda}{\lambda + 2\mu}$ ,

$\frac{\Delta\mu}{\lambda + 2\mu}$ ,  $\frac{\Delta\kappa}{\kappa + \frac{4}{3}\mu}$ ,  $\frac{\Delta\mu}{\kappa + \frac{4}{3}\mu}$ . However, the former approach is preferred, considering the

stability of the extraction.

$$R_{pp}(\theta) = \frac{1}{4}(1 + \tan^2 \theta) \frac{\Delta\lambda}{(\lambda + 2\mu)} - (\sin^2 \theta - \frac{1}{4} \tan^2 \theta - \frac{1}{4}) \frac{\Delta 2\mu}{(\lambda + 2\mu)} + \frac{1}{4}(1 - \tan^2 \theta) \frac{\Delta \rho}{\rho} \quad (3.7)$$

$$R_{PP}(\theta) = \frac{1}{4} \left(1 + \tan^2 \theta\right) \frac{\Delta\left(\kappa + \frac{4}{3}\mu\right)}{\left(\kappa + \frac{4}{3}\mu\right)} - \left(\sin^2 \theta - \frac{1}{6} \tan^2 \theta - \frac{1}{6}\right) \frac{\Delta 2\mu}{\left(\kappa + \frac{4}{3}\mu\right)} + \frac{1}{4} \left(1 - \tan^2 \theta\right) \frac{\Delta\rho}{\rho} \quad (3.8)$$

In the application of this extraction,  $\lambda$ ,  $\mu$ , and  $\kappa$ , are used to indicate the anomalies caused by lithology and the presence of hydrocarbons. To use the existing algorithms of inversion to solve  $\lambda$ ,  $\mu$ , and  $\kappa$ , the ratios  $\frac{\Delta\lambda}{\lambda}$ ,  $\frac{\Delta\mu}{\mu}$ , and  $\frac{\Delta\kappa}{\kappa}$  are required. These reflectivities are calculated after extracting  $\frac{\Delta\lambda}{\lambda + 2\mu}$ ,  $\frac{\Delta\mu}{\lambda + 2\mu}$ , and  $\frac{\Delta\kappa}{\kappa + \frac{4}{3}\kappa}$  using relationship

$$\frac{\Delta\lambda}{\lambda + 2\mu} = \frac{(V_P / V_S)^2 - 2}{(V_P / V_S)^2} \cdot \frac{\Delta\lambda}{\lambda} \quad (3.9)$$

and

$$\frac{\Delta\mu}{\lambda + 2\mu} = \frac{V_S^2}{V_P^2} \cdot \frac{\Delta\mu}{\mu} \quad (3.10)$$

This method and its application to Blackfoot data will be discussed in more detail in Chapter 4.

### 3.1.1.7. Gray's extraction

Gray (1999) expressed Aki-Richards approximation as functions of explicit  $\lambda$  and  $\mu$  reflectivity, in the following equations:

$$R_{PP}(\theta) = \left(\frac{1}{4} - \frac{1}{2} \frac{\beta^2}{\alpha^2}\right) \sec^2 \theta \frac{\Delta\lambda}{\lambda} + \frac{\beta^2}{\alpha^2} \left(\frac{1}{2} \sec^2 \theta - 2 \sin^2 \theta\right) \frac{\Delta\mu}{\mu} + \left(\frac{1}{2} - \frac{1}{4} \sec^2 \theta\right) \frac{\Delta\rho}{\rho} \quad (3.11)$$

$$R_{PP}(\theta) = \left(\frac{1}{4} - \frac{1}{3} \frac{\beta^2}{\alpha^2}\right) \sec^2 \theta \frac{\Delta\kappa}{\kappa} + \frac{\beta^2}{\alpha^2} \left(\frac{1}{3} \sec^2 \theta - 2 \sin^2 \theta\right) \frac{\Delta\mu}{\mu} + \left(\frac{1}{2} - \frac{1}{4} \sec^2 \theta\right) \frac{\Delta\rho}{\rho} \quad (3.12)$$

In equations (3.11) and (3.12), the reflectivity or the relative change of  $\lambda$ ,  $\mu$ , and  $\kappa$  is expressed explicitly. In equations (3.7) and (3.8), there are no explicit forms of reflectivity of  $\lambda$ ,  $\mu$ , and  $\kappa$ . However, using equations (3.9) and (3.10), equations (3.11) and (3.12) can be derived from equations (3.7) and (3.8) using the  $Vp/Vs$  ratio.

In the expressions of (3.7) and (3.8),  $Vp/Vs$  ratio does not appear explicitly. In the extraction of  $\frac{\Delta\lambda}{\lambda+2\mu}$ ,  $\frac{\Delta\mu}{\lambda+2\mu}$ , and  $\frac{\Delta\kappa}{\lambda+\frac{4}{3}\kappa}$  from seismic data, the background  $Vp/Vs$

model is not required. Now, however, the  $Vp/Vs$  ratio is necessary to calculate  $\frac{\Delta\lambda}{\lambda}$ ,  $\frac{\Delta\mu}{\mu}$ ,

and  $\frac{\Delta\kappa}{\kappa}$  from  $\frac{\Delta\lambda}{\lambda+2\mu}$ ,  $\frac{\Delta\mu}{\lambda+2\mu}$ , and  $\frac{\Delta\kappa}{\lambda+\frac{4}{3}\kappa}$  using equations (3.9) and (3.10).

Using (3.11) and (3.12),  $\frac{\Delta\lambda}{\lambda}$ ,  $\frac{\Delta\mu}{\mu}$ , and  $\frac{\Delta\kappa}{\kappa}$  can be extracted in one step. The errors of the  $Vp/Vs$  ratio or  $S$  information model are involved in the extraction. These errors spread into the extraction's coefficient matrix of linear equation system and the data fitting procedure.

### 3.1.2. Methodology of AVO extraction

Using the theory of wave propagation, physical parameter changes can be solved from the seismic records, which are related to reflection coefficient and angles of incidence. AVO analysis extracts both  $P$  and  $S$  wave measurements from seismic processing. The extraction of AVO usually requires the following points to be taken into consideration:

- Regardless of which approximation is used, an equation must establish a relationship between offset distance,  $x$ , and angle of incidence,  $\theta$ . To do this, a geologically meaningful velocity field must be constructed. The relationship between  $x$  and  $\theta$  is then determined by iterative ray tracing through the velocity layers. Ray tracing yields angle of incidence as a function of offset and zero-offset two-way time. A change in velocity in any interval and in particular, a change in surface can significantly affect

the angles. It is, therefore, important to use an accurate and geologically meaningful interval velocity field.

- $S$  velocity information, with the exception of Xu-Bancroft's equations, must be provided to solving the linear equations in the extraction of  $P$  and  $S$  wave information. The  $P$  wave sonic log is employed to define an interval  $P$  velocity model of the earth.  $S$  wave velocity profiles are generated from shear sonic logs, or from empirical  $V_p/V_s$  relationships, such as local 'mud-rock' lines, or the typical  $V_p/V_s$  for different lithology. The preliminary  $V_p/V_s$  is required in order to solve the equations in the last section.
- The seismic data must include a minimum range of angles for AVO extraction. As a general guideline, coverage to at least 25 degrees is necessary in the zone of interest in order to suppress noises and enhance robustness for seismic data.
- For all of the methods, fitting of the seismic data (usually CDP gathers) to the equation is performed.
- All of the equations used in the extraction have the virtue of simplicity for enabling a ready understanding of the physics involved. All of them indicate that the reflections do not depend on absolute values of rock properties, but are dependent only on certain differences in properties. Absolute values of  $V_p$ , etc., may be found by integrating (through travel time) the difference  $\Delta V_p/V_p$ , etc., found at reflecting events.
- The AVO extractions attempt the utilization of a two-term formula reduced from the three-term Aki-Richards' expression. Further unknowns are unstable if singularity of the problem is taken into account and the noises are involved in the analysis.

### 3.1.3. Fluid factor

In equation (3.4), a factor  $V_S^2/V_P^2$  occurs in the second term. Since the seismic trace is not expected to give us absolute values of  $V_P$  and  $V_S$ , a relation for water-saturated clastic silicate rocks is taken to be the mud-rock line given in Castagna, Batzle, and Eastwood (1985) as

$$V_P = 1360 + 1.16V_S. \quad (3.13)$$

This, together with the smooth  $P$  wave interval velocity function, provides a value of  $V_S/V_P$  for each time sample of the CMP gather. Equation (3.13) is a "universal" equation and a different relation may be more appropriate for a specific area. Such a relationship may be derived from cross-plots of borehole measurements, using one of the shear wave logging techniques currently available. If carbonates are present, equation (3.13) will almost certainly be inappropriate. However, many hydrocarbon provinces are characterized by interbedded sand, silt, and shale, and linear relation such as equation (3.13) will adequately predict  $V_P/V_S$ . It is fortunate that sands, silts, and shales fall on a single line on a  $V_S$ - $V_P$  cross plot (Castagna, Batzle, and Eastwood 1985).

Smith & Gildow introduced the term, fluid factor, to use the extracted  $\Delta V_P/V_P$  and  $\Delta V_S/V_S$  sections. The interpreter can extract lithological or fluid-content information from fluid factor.

All water-bearing clastic silicates usually lie close to the mud-rock line. The substitution of gas for water reduces the  $P$  wave velocity, but it hardly affects the  $S$  wave velocity, and a "fluid factor" can thus be defined as

$$\Delta F = \frac{\Delta V_P}{V_P} - 1.16 \frac{\Delta V_S}{V_S}. \quad (3.14)$$

The second term is the value of  $\Delta V_P/V_P$  predicted from  $\Delta V_S/V_S$  using the mud-rock line.  $\Delta F$  will be close to zero for all water-bearing rocks, but will be negative at the top and positive at the bottom of gas-filled sand.

The fluid factor has proved successful in detecting a gas reservoir (Smith & Gildow, 1987). In Chapter 4 of this thesis, the fluid factor method will be applied to describing a sand channel.

### 3.2. SENSITIVITIES OF ELASTIC PARAMETERS IN AVO ANALYSIS

In this section, some observations by author in the studying will be discussed.

Rocks are composed of particles that make up the rock framework, and pore spaces that fill in the spaces between the particles. The pore spaces are filled by some pore fluid, usually brine (salt water). How the rock will behave when subjected to longitudinal and tangential shearing forces is described by elastic constants  $\kappa$ , the bulk modulus, and  $\mu$ , the shear modulus. These physical properties are related to the rock's ability to propagate seismic waves with velocities of  $V_p$  and  $V_s$  given by:

$$V_s = \sqrt{\frac{\mu}{\rho}},$$

$$V_p = \sqrt{\frac{\kappa + \frac{4}{3}\mu}{\rho}},$$

$V_p$  can also be expressed as

$$V_p = \sqrt{\frac{\lambda + 2\mu}{\rho}},$$

where  $\lambda$  is incompressibility.

The essence of AVO analysis lies in the fact that the shear modulus  $\mu$  of a rock does not change when the fluid saturant is changed. However, the bulk modulus  $\kappa$  changes significantly when the fluid saturant is changed (Gassman, 1951). The bulk modulus of a brine-saturated rock is greater than that of gas-saturated rock brine being significantly stiffer than gas. These elastic constants are linked to seismic velocity, as shown in the above relations and result in the  $V_p$  of a gas-saturated rock being significantly less than the  $V_p$  for the same rock if it were brine-saturated. The  $S$  wave velocity ( $V_s$ ) of a gas-saturated rock is slightly higher than  $V_s$  for the same rock if it were brine-saturated, the density of gas being lower than the density of brine. The  $V_p/V_s$  ratio of gas saturated rock can thus be substantially different from the  $V_p/V_s$  ratio for the same rock if it were brine saturated.

Considering that the  $P$  and  $S$  wave velocities are determined by rock's elastic properties, there are advantages in linking them with seismic. Stewart (1995) advises that  $\lambda/\mu$  might have less influence of lithology and highlight pore-fill changes. Goodway et al. (1997) observes that the conversion from velocity measurements to Lamé's moduli parameters of rigidity ( $\mu$ ) and incompressibility ( $\lambda$ ) improves identification of reservoir zones. Cases by Goodway et al. (1997) indicate that the moduli ratio of  $\lambda/\mu$  is a sensitive hydrocarbon indicator. Starting with the brief review of the conclusions in the rock physics, sensitivity of Lamé's parameters to fluid content will now be discussed.

### 3.2.1. Dry rock line

Castagna et al. (1985) summarizes the following relationships between compressible and shear wave velocities in clastic silicate rocks:

(1) Given the compressional and shear wave velocities obtained in the laboratory for dry sandstones, the following equations may be utilized (Gassmann, 1951) to compute velocities when these rocks are saturated with water.

$$\kappa_W = \kappa_S \frac{\kappa_D + Q}{\kappa_S + Q}, \quad (3.15a)$$

$$\text{where } Q = \frac{\kappa_F(\kappa_S - \kappa_D)}{\phi(\kappa_S - \kappa_F)}, \quad (3.15b)$$

$$\mu_W = \mu_D, \quad (3.15c)$$

and

$$\rho_W = \phi\rho_F + (1 - \phi)\rho_S, \quad (3.15d)$$

where  $\kappa_W$  is the bulk modulus of the wet rock,  $\kappa_S$  is the bulk modulus of the grains,  $\kappa_D$  is the bulk modulus of the dry frame,  $\kappa_F$  is the bulk modulus of the fluid,  $\mu_W$  is the shear modulus of the wet rock,  $\mu_D$  is the shear modulus of the dry rock,  $\rho_W$  is the density of the wet rock,  $\rho_F$  is the density of the fluid,  $\rho_S$  is the density of the grains, and  $\phi$  is the porosity. In equation (3.15b),  $Q$  is an expression to simplify equation (3.15a).

(2) As in Figure 3.1 (a), the dry line established with laboratory data ( $V_p/V_s > 1.5$ ) means that the dry bulk modulus ( $\kappa_D$ ) is approximately equal to dry rigidity ( $\mu_D$ )

$$\mu_D \approx \kappa_D. \quad (3.16)$$

These are exactly equal when

$$V_p^D / V_s^D = 1.53. \quad (3.17)$$

From equation (3.15c) it follows that

$$\kappa_D \approx \mu_D = \mu_W. \quad (3.18)$$

Poisson's ratio is defined as a ratio of a fractional transverse contraction to the fractional longitudinal extraction. The Poisson's ratio is close to 0.1 in the dry rock and independent of  $P$  wave velocity (see Figure 3.1 (b)).

(3) Water-saturation causes the bulk modulus to increase. This effect is most pronounced at higher porosity (lower moduli). Water-saturated bulk modulus normalized by density is linearly related to compressible velocity (see Figure 3.1 (c)).

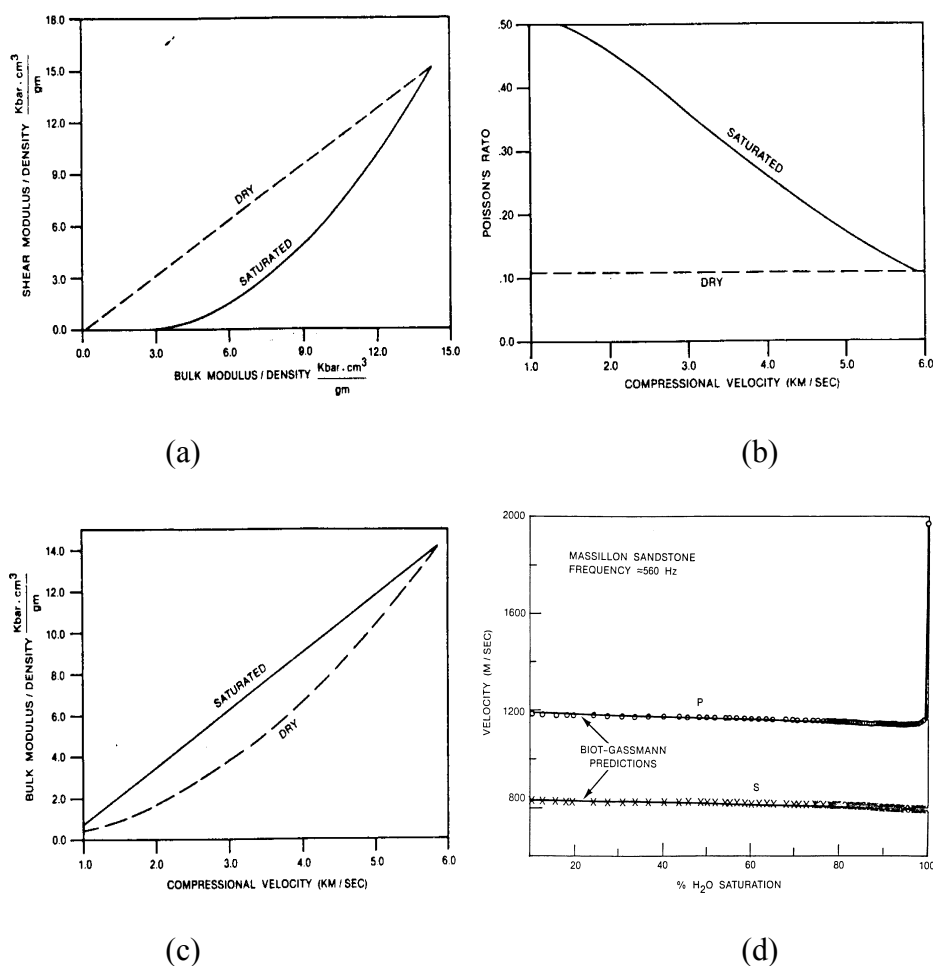


Figure 3.1. Relationships of clastic rocks (Castagna, 1985). (a) The computed relationships between the bulk and shear moduli (normalized by density) based on the observed  $V_s$  and  $V_p$  trends. (b) The computed relationships between Poisson's ratio and  $V_p$  based on the observed  $V_s$  and  $V_p$  trends. (c) The computed relationships between the bulk modulus (normalized by density) and  $V_p$  based on the observed  $V_s$  and  $V_p$  trends. (d) Gassmann's equation prediction and observed  $V_p$  and  $V_s$ .

### 3.2.2. $\kappa-\mu$ as direct hydrocarbon indicator

Compared with the grain and frame bulk moduli, the bulk modulus of gas is small enough to be ignored and, consequently, the  $Q$  term in equation (3.15b) is approximated to zero. This means that the gas-saturated rock behaves as dry rock and that  $(\kappa-\mu)$  is close to zero for gas sand. In Figure 3.1 (a), there are always big differences between the bulk moduli of water-saturated rock and dry rock, when  $V_p < 6\text{km/s}$ . Therefore,

$(\kappa-\mu)$  should be very sensitive to the existing gas. In addition, the partially water-saturated rocks behave as dry rocks. The Gassmann equation and laboratory results in Figure 3.1 (d) support this assumption.

Figures 3.2, 3.3 and 3.4 are crossplots of elastic parameters for certain rock samples, as used by Goodway et al (1997). Figure 3.2 shows the crossplot of the product of incompressibility and density ( $\lambda\rho$ ) and the product of shear modulus and density ( $\mu\rho$ ), resulting from Goodway et al (1997). The threshold cutoff for porous gas sand is shown. In Figure 3.3, the product of bulk modulus and density ( $\kappa\rho$ ) and that of shear modulus and density ( $\mu\rho$ ) are cross-plotted, with the gas sand and shaly gas sand samples lying around the dry rock line. In Figure 3.4,  $((\kappa-\mu)\rho)$  and  $(\mu\rho)$  are cross-plotted. The threshold cutoff for porous gas sand represented by the  $(\kappa-\mu=0)$  line is easily determined, in that the gas sand and shaly gas sand gather around it. In Figures 3.2, 3.3, and 3.4, the carbonate samples may easily be separated from shale and sand samples.

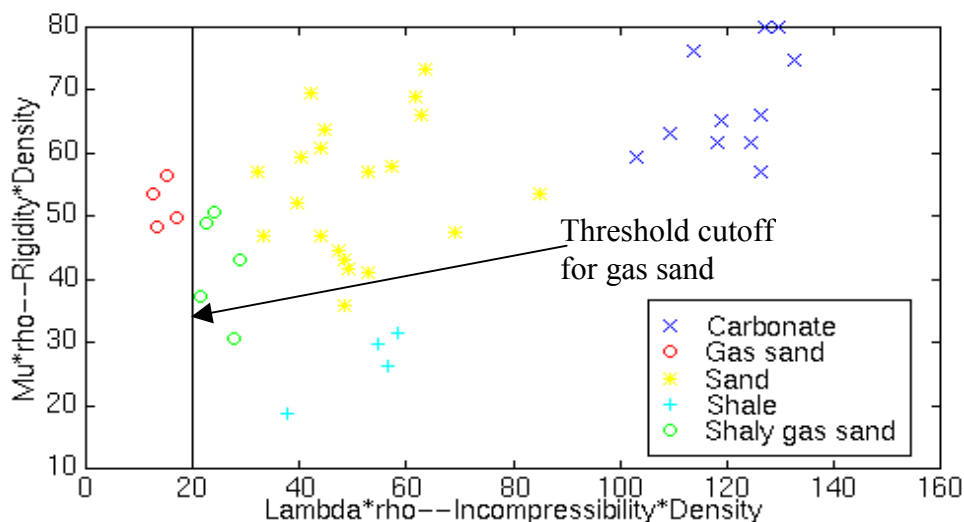


Figure 3.2.  $\mu\rho$  vs  $\lambda\rho$  crossplot of Gas well log data (Goodway et al, 1997)

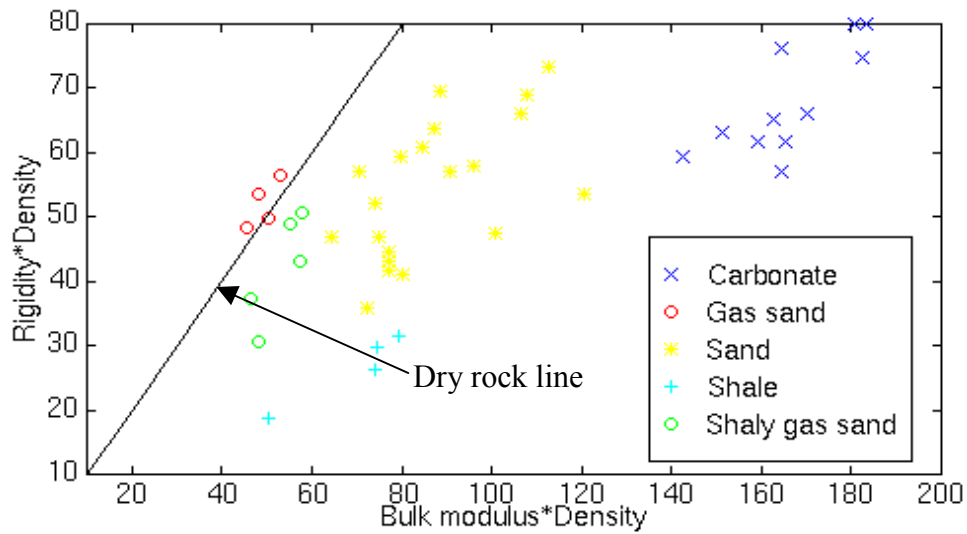


Figure 3.3.  $\mu\rho$  vs  $\kappa\rho$  crossplot of gas well log data.

Since the fact that gas causes  $\kappa$  in wet rock to change significantly, and that  $\mu$  does not change as gas fills the dry rock frame, the sensitivity of  $(\kappa-\mu)$  may be utilized to detect the gas existing in rocks. Table 3.1 contains various rock property values, which are the gas reservoir log data (Goodway et al, 1997), and average percentage changes. Since  $\kappa=\lambda+2/3\mu$ ,  $\kappa$  is not as sensitive to detect fluid saturation as  $\lambda$ , the sensitivity of  $\kappa$  being diluted by  $2/3\mu$  (i.e. non-pore fluid). However, the  $(\kappa-\mu)=(\lambda-1/3\mu)$  is more sensitive than  $\lambda$  in detecting the gas existing in the rock frames. Quantitatively speaking,  $(\kappa-\mu)$  has a value around zero when gas is in the rock. In Table 3.2, actual  $V_p$ ,  $V_s$ , and  $\rho$  values from a shallow well have been combined to give various rock property values. With the exception of  $\kappa$ ,  $\kappa-\mu$ ,  $(\kappa-\mu)/\mu$ , all other values given are quoted from Goodway et al.'s paper (1997). By comparing the average % changes of  $\lambda$  and  $\kappa-\mu$ , it is evident that  $\kappa-\mu$  is more sensitive than  $\lambda$  to variations in rock properties that range from capping shale to gas sand. It may also be noted that the average % change of the  $(\kappa-\mu)/\mu$  ratio is greater than the average % change of  $\lambda/\mu$ .

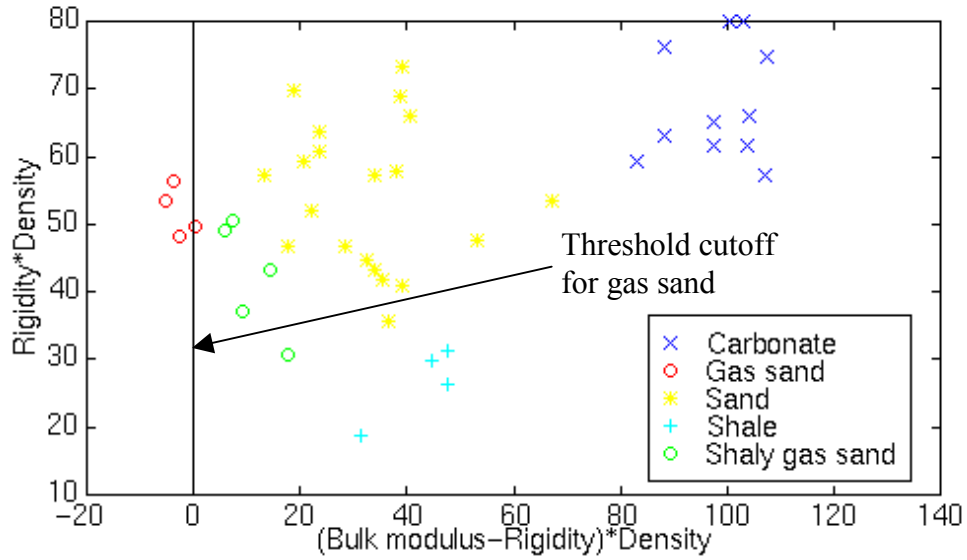


Figure 3.4.  $\mu\rho$  vs  $(\kappa-\mu)\rho$  crossplot of Gas well log data.

Table 3.1. Properties for a gas sand model

	$V_s$ (m/s)	$V_p$ (m/s)	$\rho$
Shale	1290	2898	2.425
Gas Sand	1666	2857	2.275
	$\Delta V_s/V_s=0.25$	$\Delta V_p/V_p=-0.014$	$\Delta\rho/\rho=-0.064$

Table 3.2. Shallow Gas Sand Log Measurements (Goodway et al, 1997)

	$V_p/V_s$	$(V_p/V_s)^2$	$\sigma$	$\lambda+2\mu$	$\lambda$	$\mu$	$\kappa$	$\lambda/\mu$	$\kappa-\mu$	$(\kappa-\mu)/\mu$
Shale	2.25	5.1	0.38	20.37	12.3	4.035	15.0	3.1	11	2.73
Gas sand	1.71	2.9	0.24	18.53	5.9	6.314	10.1	0.9	3.8	0.60
Av. % change	27	55	45	9.2	70	44	39	110	97	128

### 3.2.3. Cross-plots of well log elastic parameters

The sensitivities of different elastic parameters may be compared using well logs. Figure 3.5 shows cross-plots of well 08-08's attributes in the Blackfoot survey. The channel sand samples are circled in this figure. Figure 3.5a shows  $P$  and  $S$  velocities along with density. Figure 3.5b is the crossplot of  $S$  and  $P$  wave velocities showing the channel sand in the circle; Figure 3.5c is the crossplot of shear modulus ( $\mu$ ) and bulk modulus ( $\kappa$ ); the crossplot of incompressibility ( $\lambda$ ) and shear modulus ( $\mu$ ) is shown in Figure 3.5d. Figure 3.5e shows the crossplot of shear modulus ( $\mu$ ) and  $(\lambda+2\mu)$ . Figure 3.5f is the crossplot of shear modulus ( $\mu$ ) and  $(\kappa-\mu)$ . In Figure 3.5c it may be observed that the channel sand samples are close to the dry line, whereas in Figure 3.5d and 3.5f the samples outside the channel are more scattered. In Figure 3.5f, the  $(\kappa-\mu)$  of channel sand samples are close to threshold cutoff for gas existing.

In Figure 3.6, only the elastic parameters of Glauconitic channel sand in Blackfoot are cross-plotted. Rock samples are chosen from three wells, 08-08, 12-16, and 04-16. The samples of the well 08-08, which has oil indication, are separated from samples of other wells on each crossplot.

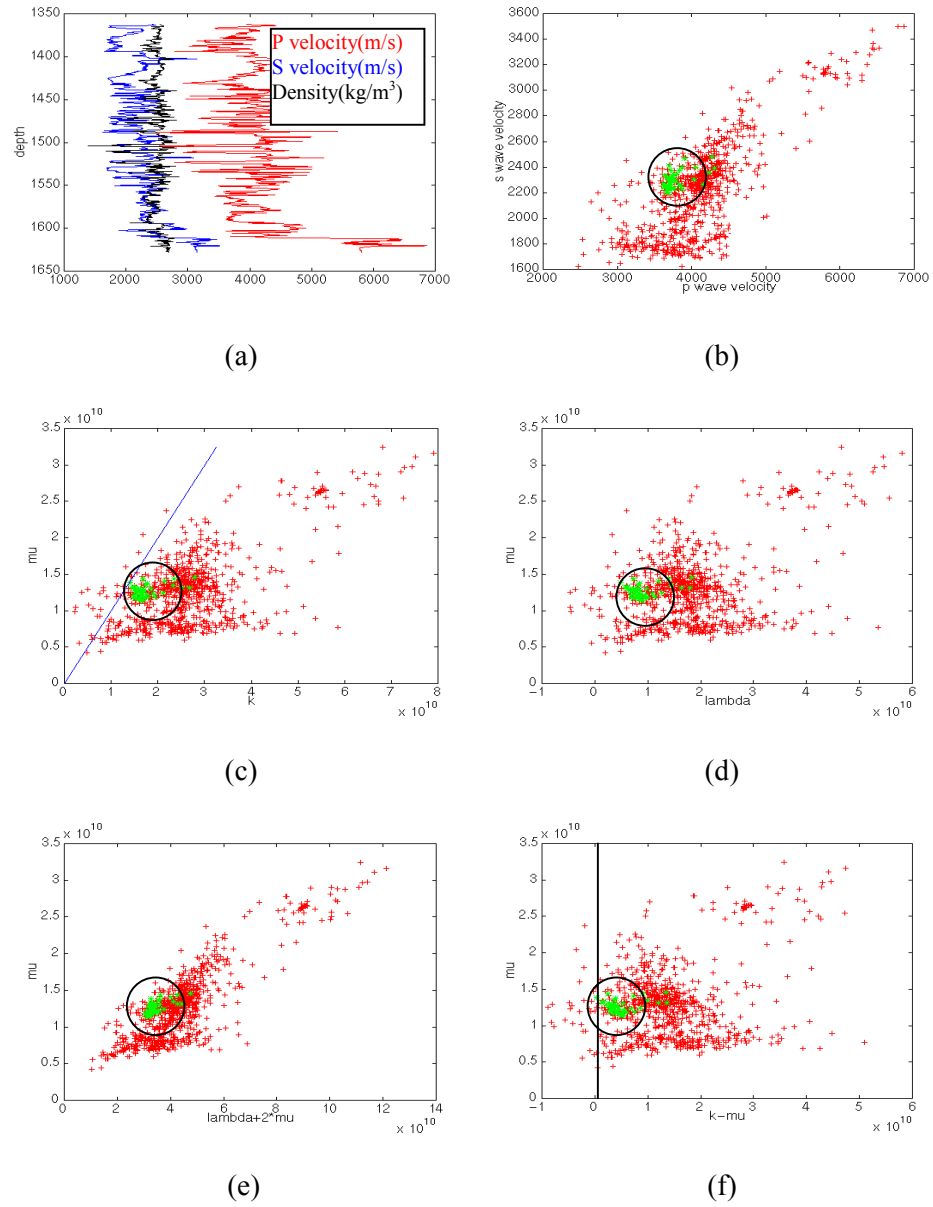


Figure 3.5. Cross-plots of well 08-08 in Blackfoot. In (c), the line stands for  $\mu = \kappa$ ; in (f) the line stands for  $\mu - \kappa = 0$ .

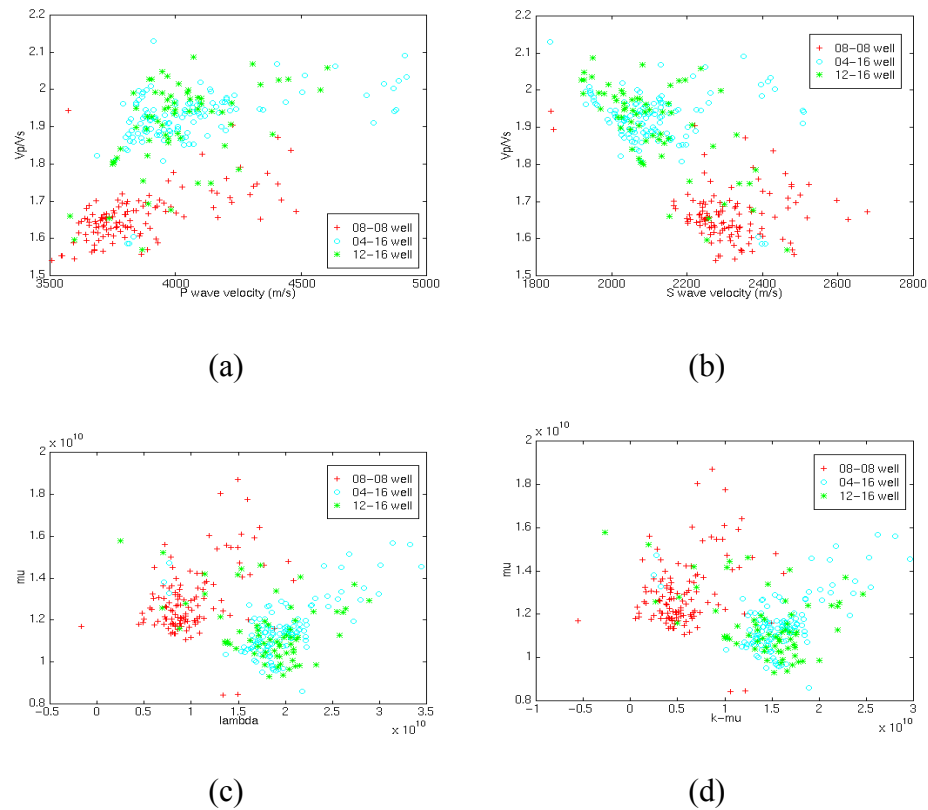


Figure 3.6. The cross-plots of elastic parameters of the Glauconitic formation

### 3.2.4. Relative changes of physical properties

Figures 3.5 and 3.6 cross-plot the properties of different lithologies, using samples from well logs. However, the seismic data acquired fails to provide rock information with a scale and resolution similar to the well log data. The ideal seismic data actually catalogues the reflectivities with a limited frequency band that limits the resolution. The reflectivities equal the contrasts of rock properties, e.g. the normal incidence  $P$  wave reflection coefficient,  $R_{P0}$ , is the contrast of impedance in the equation  $R_{P0} = \frac{I_2 - I_1}{I_2 + I_1}$ , where  $I$  is the impedance. The AVO response (see section 3.1) also depends only on certain differences in properties, instead of the absolute values, though the absolute value of the properties can be found by integrating the differences.

In Figure 3.7, a number of relative changes or contrasts relative to Lamé's parameters are plotted using a blocked well log model. Note the small relative change of density, compared to several forms of relative changes of  $\lambda$  and  $\mu$ . The relative changes of  $\lambda$  and  $\mu$  actually magnify the changes of  $V_p$  and  $V_s$ . The great change of  $\Delta\mu/\mu$  at the oil bearing layer (1580 meter) may also be noted.

The seismic reflectivity is actually directly relative to the impedance that is a product of velocity and density. In fact,  $\Delta\lambda/\lambda$  and  $\Delta\mu/\mu$  have relationships with  $\Delta V_p/V_p$  and  $\Delta V_s/V_s$  as follows.

$$\frac{\Delta V_p}{V_p} = \frac{1}{2} \left( 1 - 2 \frac{V_s^2}{V_p^2} \right) \frac{\Delta\lambda}{\lambda} + \frac{V_s^2}{V_p^2} \frac{\Delta\mu}{\mu} - \frac{1}{2} \frac{\Delta\rho}{\rho}$$

$$\frac{\Delta V_s}{V_s} = \frac{1}{2} \left( \frac{\Delta\mu}{\mu} - \frac{\Delta\rho}{\rho} \right)$$

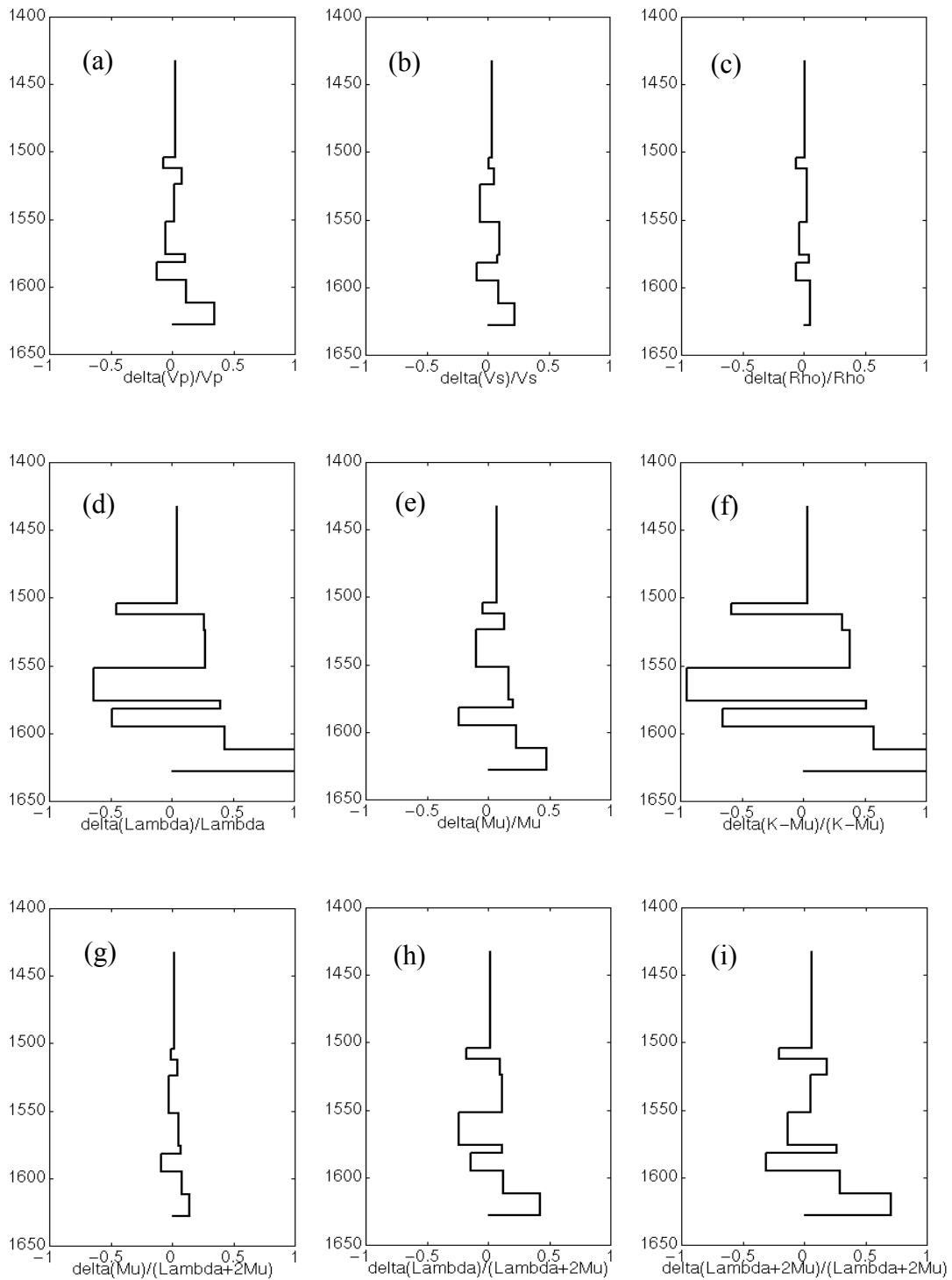


Figure 3.7. Comparisons of various relative changes of rock parameters from well 08-08 in Blackfoot survey. (a)  $\Delta V_p/V_p$ ; (b)  $\Delta V_s/V_s$ ; (c)  $\Delta \rho/\rho$ ; (d)  $\Delta \lambda/\lambda$ ; (e)  $\Delta \mu/\mu$ ; (f)  $\Delta(\kappa - \mu)/(\kappa - \mu)$ ; (g)  $\Delta \mu/(\lambda + 2\mu)$ ; (h)  $\Delta \lambda/(\lambda + 2\mu)$ ; (i)  $\Delta(\lambda + 2\mu)/(\lambda + 2\mu)$ .

### 3.3. NOISE IN AVO ANALYSIS

Many factors contribute to make the AVO analysis under-deterministic, e.g., poor signal to noise ratio ( $S/N$ ), low resolution, and insufficient incident angle range. The seismic data contains many different kinds of noise, however, only the primary reflections are regarded as signal for AVO analysis. If noise is involved in a random way, it proves less problematic than coherent noise. Coherent noise, such as ground roll and multiples, has spatially variant frequency in a gather and may bias AVO estimation if they are not attenuated properly. Techniques have been developed to suppress ground rolls and multiples, e.g., the F-K filter, which can get rid of linear noise such as ground roll; while the Radon transform is a strong tool to de-multiple. However, F-K filters and Radon transforms can destroy the true AVO phenomena caused by real lithology changes or fluid saturation and subsequently distort AVO responses. Short period multiples with small residual moveout create a false amplitude variation with offset and are extremely difficult to remove. In the work of this thesis, robust estimation is applied to extract elastic parameters from AVO gathers. Robust estimation is referenced in *Numerical Recipes* (Press, Flannery, Teukolsky, and Vetterling, 1986). One kind of robust estimation uses  $L1$  norm as the objective function, comparative with  $L2$  norm in least-square estimation. In the following subsections, theories of  $L1$  norm estimation are shown briefly and the  $L1$  and  $L2$  norm estimations are compared using simple models.

#### 3.3.1. Theory review of $L1$ and $L2$ norms

When we fit  $N$  data samples  $(x_i, y_i)$   $i=1, \dots, N$ , to a model having  $M$  adjustable parameters  $a_j$ ,  $j=1, \dots, M$ , the model to predict the relationship between measured independents and dependents is expressed as the function:

$$y(x) = y(x; a_1 \dots a_M).$$

The least square fitting tries to minimize the following objective function, equation (3.19), over  $a_1 \dots a_M$

$$\sum_{i=1}^N [y_i - y(x_i; a_1 \dots a_M)]^2. \quad (3.19)$$

The least square estimation minimizes the  $L2$  norm of residual, which is the squared difference between measured and calculated values. The least squares fitting is a maximum likelihood estimation of the fitted parameters if the measurement errors are independent and normal distributed with constant standard deviation (Gaussian distribution). However, some experimental points are deviated from normal distribution. They can easily turn a least squares fit into nonsense. Subsequently, minimizing  $L1$  norm is a better option for data containing large bursts of noise that are referred as outliers. The objective function of optimization of  $L1$  norm is as equation (3.20)

$$\sum_{i=1}^N |y_i - y(x_i; a_1 \dots a_M)|. \quad (3.20)$$

Minimizing equation (3.19) over  $a_1 \dots a_M$  is equivalent to solving the zero derivative of equation (3.19) over  $a_1 \dots a_M$ . The equation becomes

$$\sum_{i=1}^N [y_i - y(x_i)] \left( \frac{\partial y(x_i; a_1 \dots a_M)}{\partial a_k} \right) \quad k=1, \dots, M. \quad (3.21)$$

By contrast, the zero derivative of equation (3.20) over  $a_1 \dots a_M$  is

$$\sum_{i=1}^N \text{sgn}[y_i - y(x_i)] \left( \frac{\partial y(x_i; a_1 \dots a_M)}{\partial a_k} \right) \quad k=1, \dots, M. \quad (3.22)$$

Both  $[y_i - y(x_i)]$  in equation (3.21) and  $\text{sgn}[y_i - y(x_i)]$  in equation (3.22) work as weighting functions. Equation (3.21) tells that the more deviant the samples, the greater the weight. In comparison, all deviant points receive the same relative weight in equation (3.22), with only the sign information used. When prominent noise exists, equation (3.22) has advantages over equation (3.21).

Since  $\text{sgn}[y_i - y(x_i)]$  is discontinuous, there is no simple way to solve the  $L1$  norm optimization as solving a least squares system. In this thesis, the downhill simplex minimization algorithm (see *numerical recipes*) is applied. It does not make assumptions about continuity, however, it is much more expensive than solving least square system, and its running time greatly depends up on its starting value. In the thesis, the model

fitted by least square estimation is used as starting value in the downhill simplex minimization.

### 3.3.2. Comparison of $L1$ and $L2$ norm estimations

In the following, a model is made to evaluate the robust estimation. The model has only one reflector at 1.0 s. A geometry is formed to include 101 source-receiver pairs with CDP at the reflector. The reflection coefficients at all offsets are calculated using equation (3.23), which comes from equation (3.6) in section 3.1.

$$R_{PP}(\theta) = \frac{1}{2}(1 + \tan^2 \theta)^2 \frac{\Delta I_P}{I_P} - 4 \left( \frac{V_S}{V_P} \right)^2 \sin^2 \theta \frac{\Delta I_S}{I_S}. \quad (3.23)$$

$$\text{In fact } R_{P0} = \frac{1}{2} \frac{\Delta I_P}{I_P} \text{ and } R_{S0} = \frac{1}{2} \frac{\Delta I_S}{I_S}.$$

To create the data, the  $Rp$  and  $Rs$  are given. The  $\theta$  corresponding to each offset is calculated. The reflection coefficient at each offset is calculated using equation (3.23). The reflection coefficients are filtered by a band pass filter of 5-10-60-70 Hz to simulate seismic traces in the real world. The noise may be added on the traces. After that, the inverse problem is solved: do the curve fitting using equation (3.23) and solve  $Rp$  and  $Rs$ . The solved  $Rp$  and  $Rs$  may have difference from the true. To evaluate the error of the extraction, substitute the solved  $Rp$  and  $Rs$  into equation (3.23) and calculate reflection coefficient for each offset and obtain reconstructed data set. The difference between the reconstructed and the noise free data is evaluated. The following figures in this section are relate to the evaluation of the  $L1$  and  $L2$  norm fittings. In them, both unfiltered spikes and filtered CDP gathers are shown. Figure 3.8 shows the primary spikes and waveforms.

To evaluate the robustness of the estimations, three kinds of artificial noises are created: multiple, linear noise, and random noise.

#### 3.3.2.1. Multiple effects

The multiple "noise" is superposed close to the primary reflectivities and the new gathers are created as shown In Figures 3.9 to 3.22. In these figures, the multiples have different residual moveout.

From the gathers on each individual figure (3.9 to 3.22), amplitude of samples at 1.0s is picked to do least square and  $L1$  norm fitting. The fitted  $R_p$  and  $R_s$  (band pass filtered) are used to re-construct the response by equation (3.23).

The average value of the noise-free samples is estimated by

$$A_{\text{exp}} = \sum_{i=1}^N y_{\text{true}}(x_i) / N, \quad (3.24)$$

where  $N$  is the number of offsets,  $x$  is offset and  $y$  is the amplitude value at 1.0s.

The RMS deviations of noise data are calculated as

$$D = \sqrt{\sum_{i=1}^N (y_{\text{noisy}}(x_i) - y_{\text{true}}(x_i))^2 / N}, \quad (3.25)$$

where  $y_{\text{noisy}}$  is the amplitude at 1.0s with multiple contamination.  $D/A_{\text{exp}}$  can be used to denote the noise level. Table 3.3 shows the RMS deviations, and the errors of fitted  $R_p$  and  $R_s$  for Figures 3.9 to 3.22.

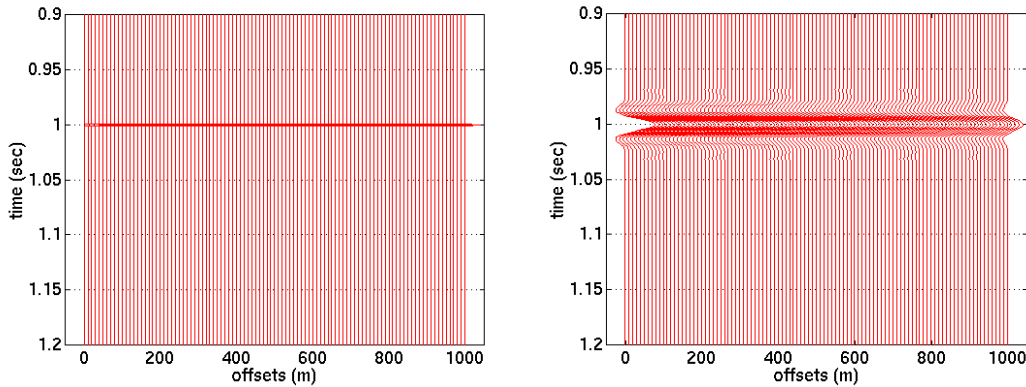


Figure 3.8. A primary reflection model. The reflectivities versus offsets are on the left side. The right side is the AVO gather created by convolution of reflectivities with bandpass filter of 5-10-60-70 Hz.

Table 3.3. The RMS deviations, errors of fitted  $R_p$  and  $R_s$  for Figures 3.9 to 3.22.

Figures of fitting	Figures of gather	Relative Deviations ( $D/A_{exp}$ )	Error of $R_p$ (L2 norm fitting)	Error of $R_s$ (L2 norm fitting)	Error of $R_p$ (L1 norm fitting)	Error of $R_s$ (L1 norm fitting)
Figure 3.10	Figure 3.9	23.5%	7.059%	13.53%	0.024%	0.012%
Figure 3.12	Figure 3.11	32.4%	16.47%	32.94%	0.000%	0.024%
Figure 3.14	Figure 3.13	39.7%	24.71%	50.00%	0.224%	0.365%
Figure 3.16	Figure 3.15	45.6%	34.12%	70.00%	16.42%	30.04%
Figure 3.18	Figure 3.17	50.0%	41.12%	83.53%	35.04%	68.86%
Figure 3.20	Figure 3.19	54.4%	49.41%	98.24%	44.51%	93.11%
Figure 3.22	Figure 3.21	100.0%	52.94%	101.8%	49.44%	101.5%

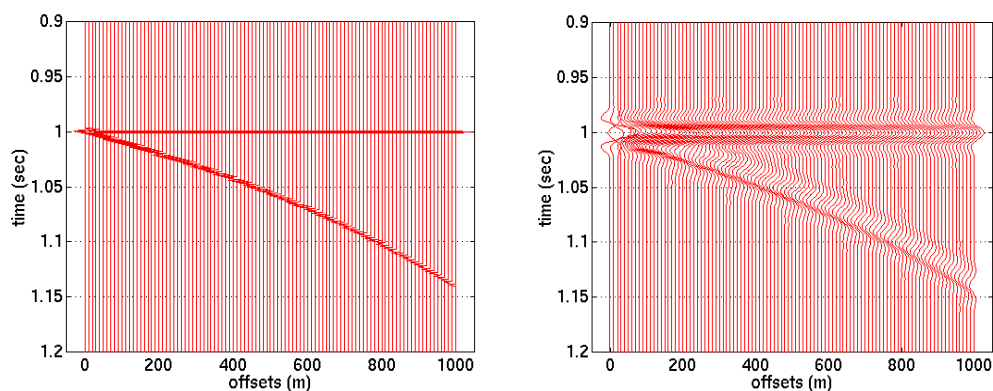


Figure 3.9. A reflection model with primary reflection contaminated by multiple. The reflectivities versus offsets are on left side. The right side is the AVO gather created by convolution of reflectivities with bandpass filter of 5-10-60-70 Hz. At 1.0s  $D/A_{exp}=23.5\%$ .

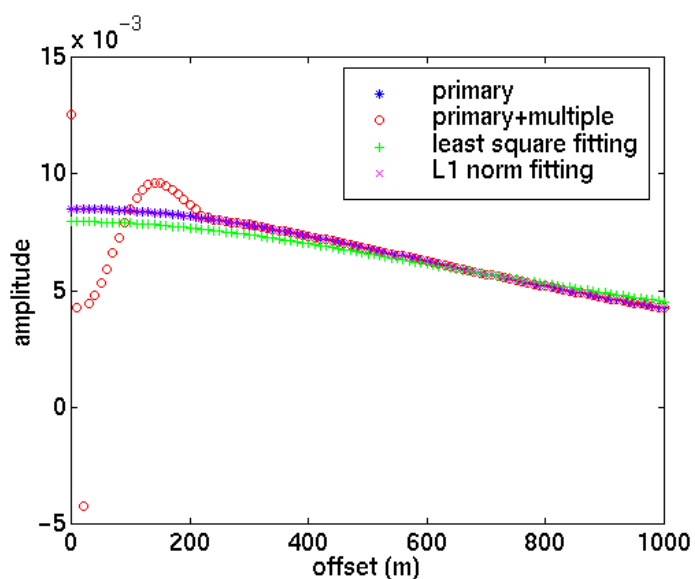


Figure 3.10. The exact primary reflection amplitude, multiple polluted primary reflection amplitude, recovered amplitude from extracted  $R_P$  and  $R_S$  using  $L1$ , and recovered amplitude from extracted  $R_P$  and  $R_S$  using  $L2$  norm fitting. The data used for extraction is shown in Figure 3.9. The amplitude at each offset at 1.0s is picked on noise free data, noise data, and reconstructed data from the extraction results. Same work is done for other similar plots.

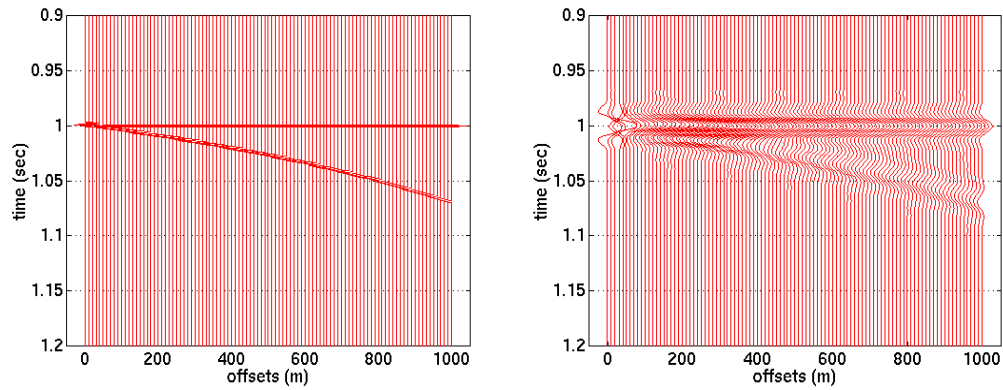


Figure 3.11. A reflection model with primary reflection contaminated by multiple. The reflectivities versus offsets are on left side. The right side is the AVO gather created by convolution of reflectivities with bandpass filter of 5-10-60-70 Hz. At 1.0s  $D/A_{exp}=32.4\%$ .

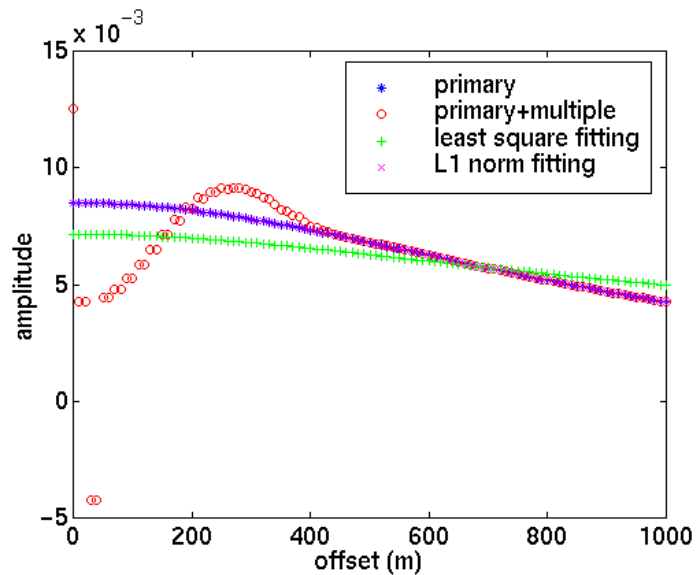


Figure 3.12. The exact primary reflection amplitude, multiple polluted primary reflection amplitude, recovered amplitude from extracted  $R_P$  and  $R_S$  using  $L1$ , and recovered amplitude from extracted  $R_P$  and  $R_S$  using  $L2$  norm fitting. The data used for extraction is shown in Figure 3.11.

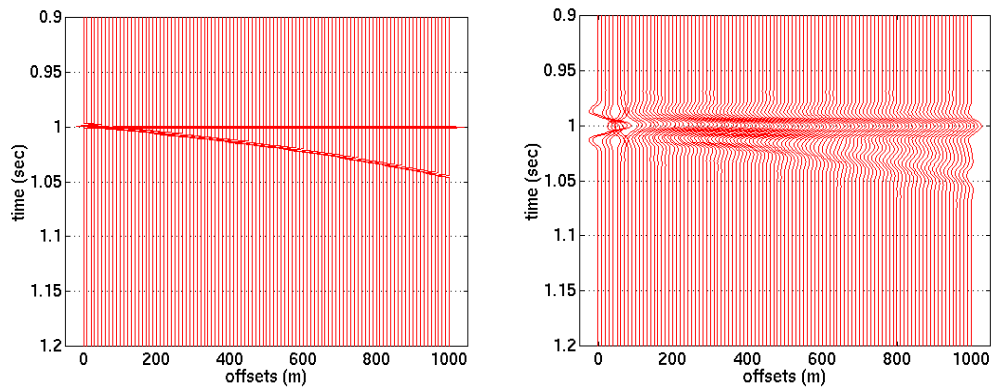


Figure 3.13. A reflection model with primary reflection contaminated by multiple. The reflectivities versus offsets are on left side. The right side is the AVO gather created by convolution of reflectivities with bandpass filter of 5-10-60-70 Hz. At 1.0s  $D/A_{exp}=39.7\%$ .

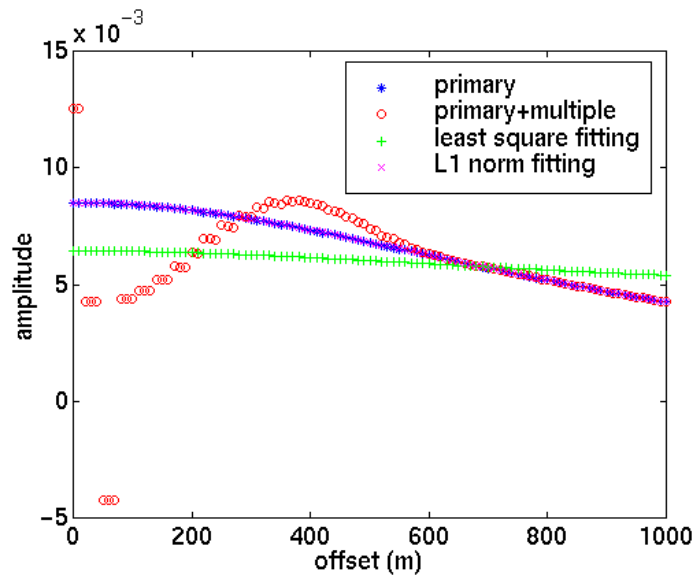


Figure 3.14. The exact primary reflection amplitude, multiple polluted primary reflection amplitude, recovered amplitude from extracted  $R_P$  and  $R_S$  using  $L1$ , and recovered amplitude from extracted  $R_P$  and  $R_S$  using  $L2$  norm fitting. The data used for extraction is shown in Figure 3.13.

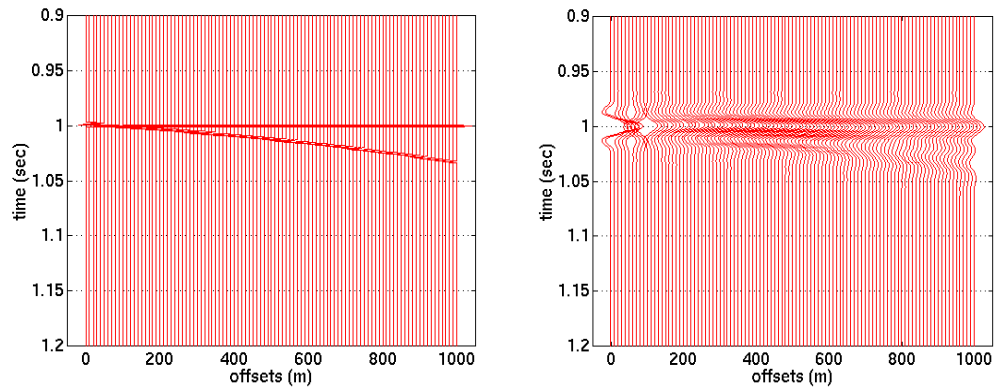


Figure 3.15 A reflection model with primary reflection contaminated by multiple. The reflectivities versus offsets are on left side. The right side is the AVO gather created by convolution of reflectivities with bandpass filter of 5-10-60-70 Hz. At 1.0s  $D/A_{exp}=45.6\%$ .

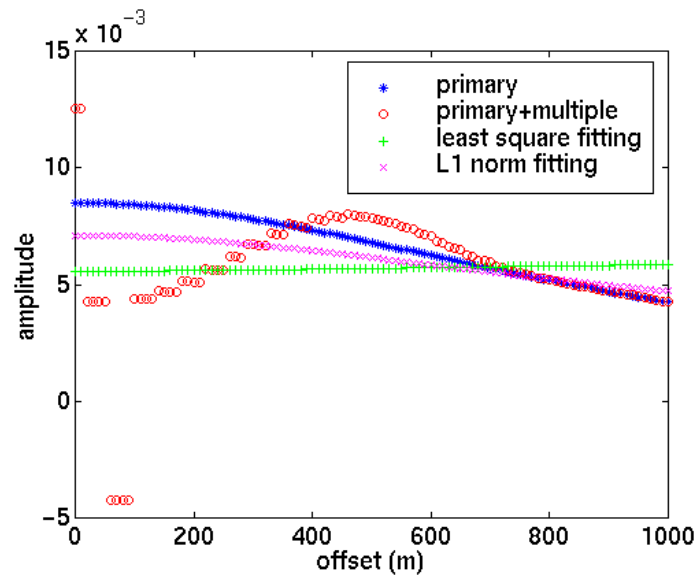


Figure 3.16. The exact primary reflection amplitude, multiple polluted primary reflection amplitude, recovered amplitude from extracted  $R_P$  and  $R_S$  using  $L1$ , and recovered amplitude from extracted  $R_P$  and  $R_S$  using  $L2$  norm fitting. The data used for extraction is shown in Figure 3.15.

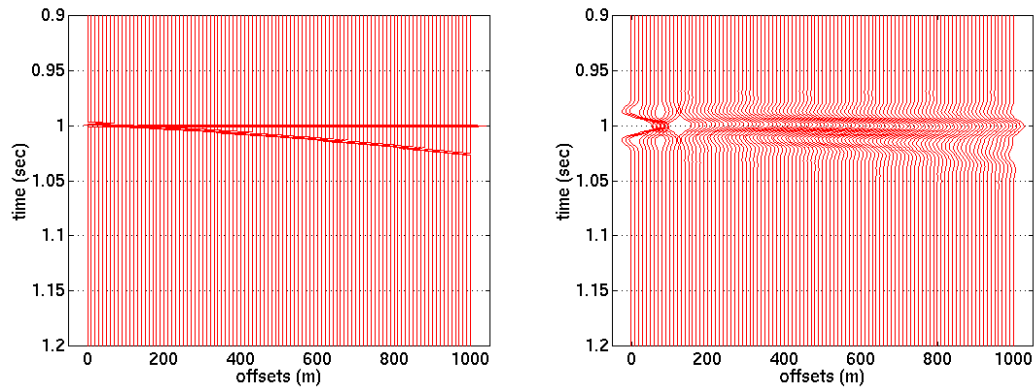


Figure 3.17. A reflection model with primary reflection contaminated by multiple. The reflectivities versus offsets are on left side. The right side is the AVO gather created by convolution of reflectivities with bandpass filter of 5-10-60-70 Hz. At 1.0s  $D/A_{exp}=50.0\%$ .

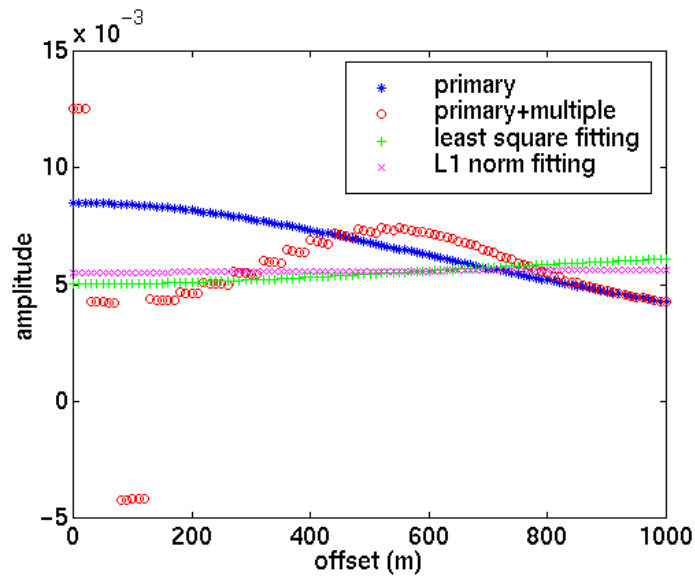


Figure 3.18. The exact primary reflection amplitude, multiple polluted primary reflection amplitude, recovered amplitude from extracted  $R_P$  and  $R_S$  using  $L1$ , and recovered amplitude from extracted  $R_P$  and  $R_S$  using  $L2$  norm fitting. The data used for extraction is shown in Figure 3.17.

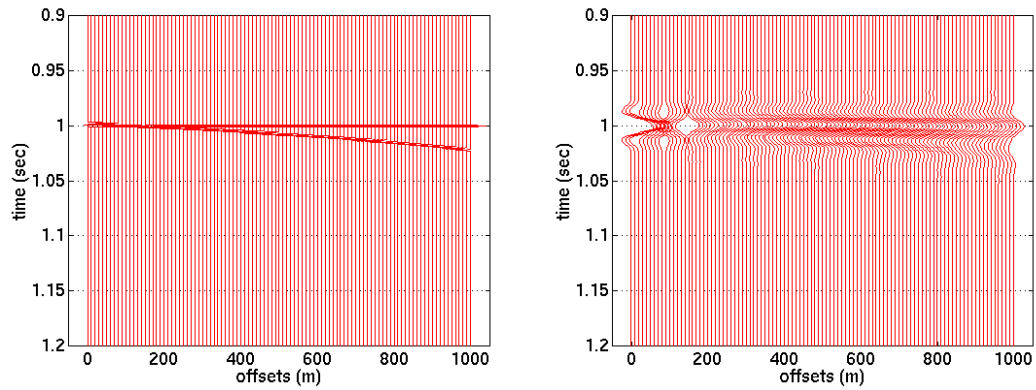


Figure 3.19. A reflection model with primary reflection contaminated by multiple. The reflectivities versus offsets are on left side. The right side is the AVO gather created by convolution of reflectivities with bandpass filter of 5-10-60-70 Hz. At 1.0s  $D/A_{exp}=54.4\%$ .

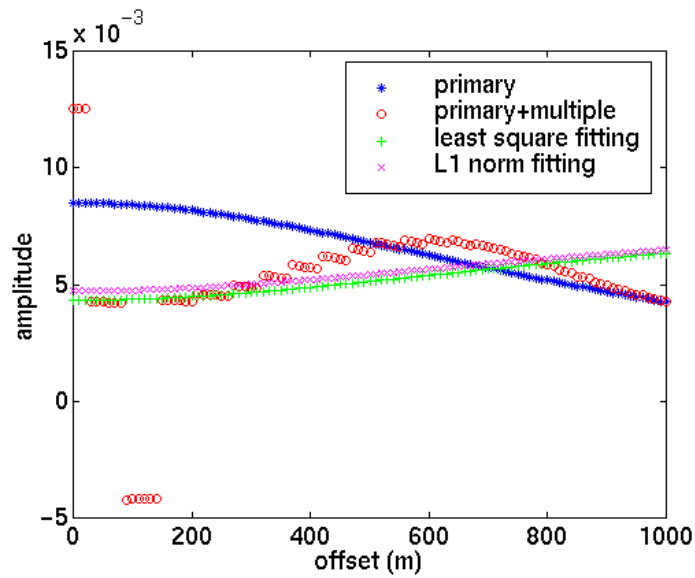


Figure 3.20. The exact primary reflection amplitude, multiple polluted primary reflection amplitude, recovered amplitude from extracted  $R_P$  and  $R_S$  using  $L1$ , and recovered amplitude from extracted  $R_P$  and  $R_S$  using  $L2$  norm fitting. The data used for extraction is shown in Figure 3.19.

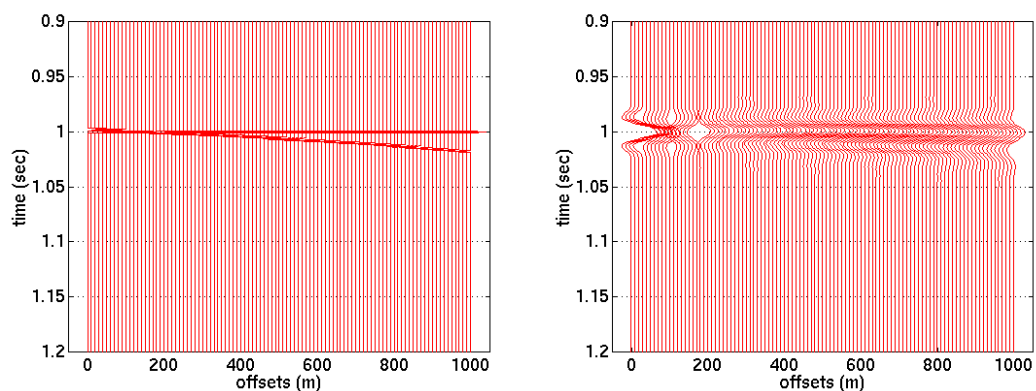


Figure 3.21. A reflection model with primary reflection contaminated by multiple. The reflectivities versus offsets are on the left side. The right side is the AVO gather created by convolution of reflectivities with bandpass filter of 5-10-60-70 Hz. At 1.0s  $D/A_{exp}=100.0\%$ .

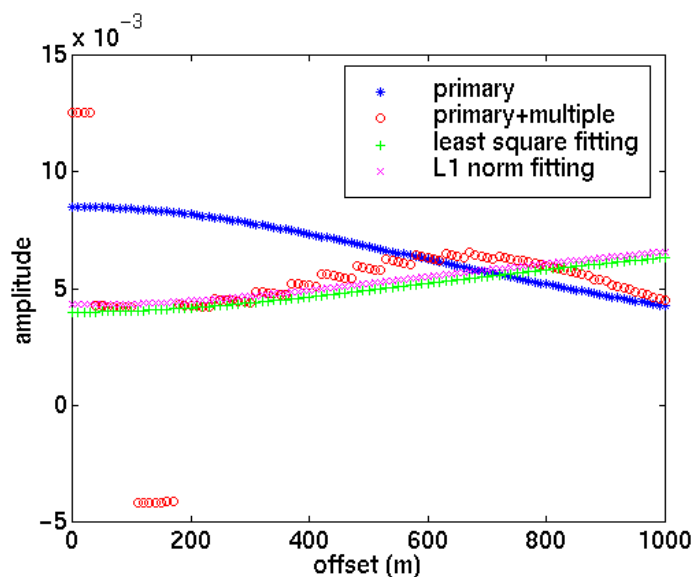


Figure 3.22. The exact primary reflection amplitude, multiple polluted primary reflection amplitude, recovered amplitude from extracted  $R_P$  and  $R_S$  using  $L1$ , and recovered amplitude from extracted  $R_P$  and  $R_S$  using  $L2$  norm fitting. The data used for extraction is shown in Figure 3.21.

The error of estimated parameters depends on the frequency band of the seismic data. If the seismic data has higher resolution, the estimation has smaller error. The model in Figures 3.21 and 3.22 is used to show this. This model has  $D/A_{exp}=100.0\%$  before the band pass filtered. Unfiltered data is used to solve the problem (i.e., the data in

the left side of Figure 3.21 are used as input). The relative errors of  $R_p$  and  $R_s$  by  $L1$  and  $L2$  norm estimations are listed in Table 3.4. By comparing this table with the last line in Table 3.3, we note that the unfiltered data produce much better result than the data after bandpass filter.

Table 3.4. The RMS deviations, errors of fitted  $R_p$  and  $R_s$  for the spikes before band pass filtering in Figure 3.21.

	Error of $R_p$	Error of $R_s$
$L1$ norm estimation	0.039%	0.103%
$L2$ norm estimation	26.5%	51.2%

After the comparisons of  $L1$  and  $L2$  norm fittings in this subsection, a few conclusions may be made:

- $L1$  norm works much better than  $L2$  norm on the data with coherent noise like multiples, even if the noise biases the data greatly.
- The error of both  $L1$  and  $L2$  norm fittings increases with the reduction of move-out of multiples.
- The fitted  $R_s$  has larger error than fitted  $R_p$ .

### 3.3.2.2. Linear noises

Artificial linear noises are created by superposing a slant event over primary reflection. Figures 3.23 to 3.34 test the cases with linear noise: one slant event at different offsets; and two slant events with different polarities. Table 3.5 presents the RMS deviations, and the errors of fitted  $R_p$  and  $R_s$  for Figures 3.23 to 3.34.

Table 3.5 The RMS deviations, and the errors of fitted  $R_p$  and  $R_s$  for Figures 3.23 to 3.34.

Figures of fitting	Figures of gather	Relative Deviations ( $D/A_{exp}$ )	Error of $R_p$ ( $L1$ norm fitting)	Error of $R_s$ ( $L1$ norm fitting)	Error of $R_p$ ( $L2$ norm fitting)	Error of $R_s$ ( $L2$ norm fitting)
Figure 3.24	Figure 3.23	36.8%	0.05%	0.2%	2.35%	24.1%
Figure 3.26	Figure 3.25	36.8%	0.035%	0.035%	5.88%	4.71%
Figure 3.28	Figure 3.27	36.8%	0.059%	0.094%	20.0%	40.6%
Figure 3.30	Figure 3.29	51.5%	0.624%	3.376%	15.29%	14.71%
Figure 3.32	Figure 3.31	51.5%	0.965%	3.441%	92.94%	58.82%
Figure 3.34	Figure 3.33	51.5%	0.671%	2.253%	24.71%	65.88%

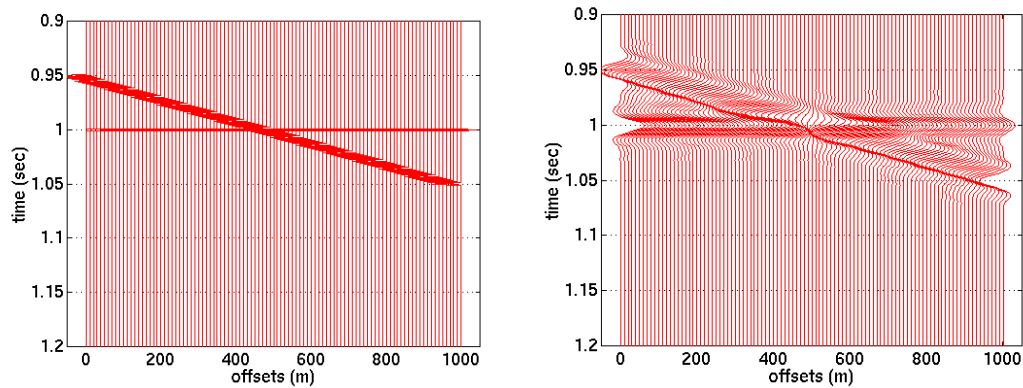


Figure 3.23. A reflection model with primary reflection contaminated by linear noise. The linear event crosses over primary reflection event at medium offsets. The reflectivities versus offsets are on the left side. The right side is the AVO gather created by convolution of reflectivities with bandpass filter of 5-10-60-70 Hz. At 1.0s  $D/A_{exp}=36.8\%$ .

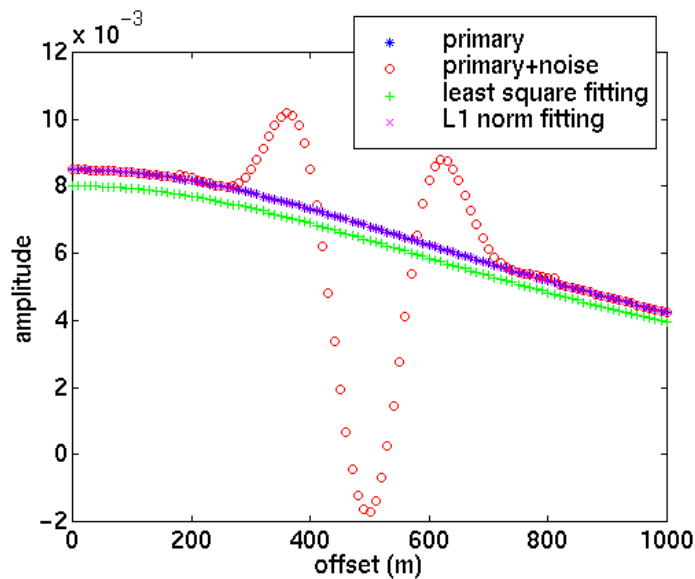


Figure 3.24. The exact primary reflection amplitude, linear noise polluted primary reflection amplitude, recovered amplitude from extracted  $R_P$  and  $R_S$  using  $L1$ , and recovered amplitude from extracted  $R_P$  and  $R_S$  using  $L2$  norm fitting. The data used for extraction is shown in Figure 3.23.

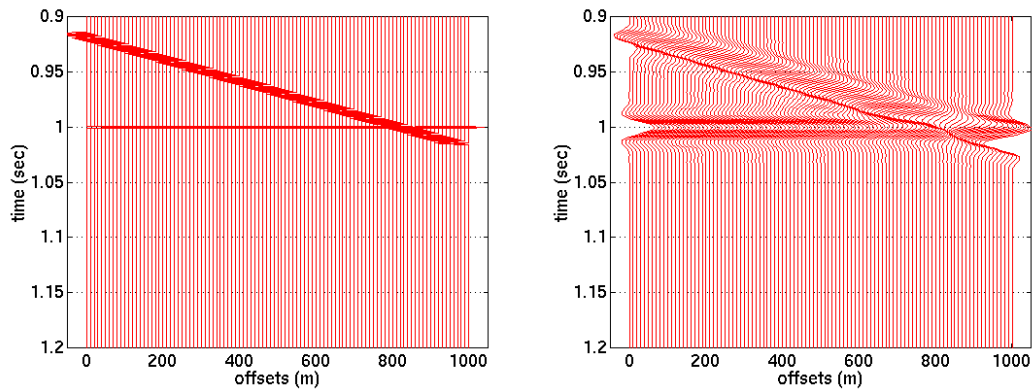


Figure 3.25. A reflection model with primary reflection contaminated by linear noise. The linear event crosses over the primary reflection event at far offsets. The reflectivities versus offsets are on the left side. The right side is the AVO gather created by convolution of reflectivities with bandpass filter of 5-10-60-70 Hz. At 1.0s  $D/A_{exp}=36.8\%$ .

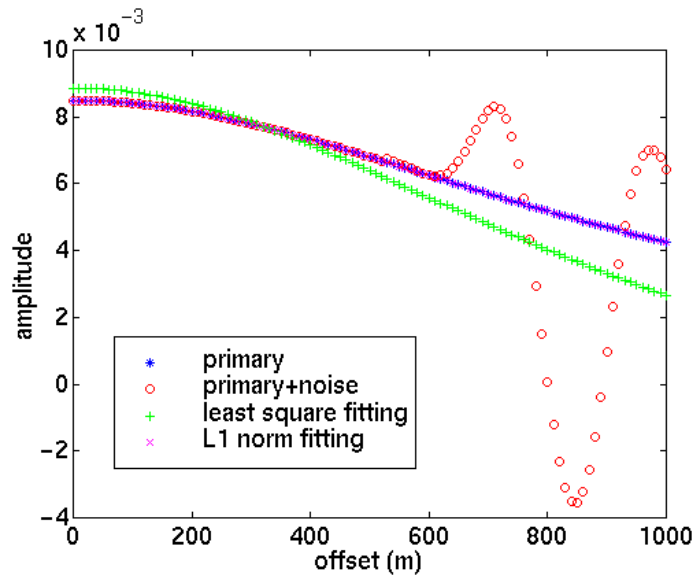


Figure 3.26. The exact primary reflection amplitude, linear noise polluted primary reflection amplitude, recovered amplitude from extracted  $R_P$  and  $R_S$  using  $L1$ , and recovered amplitude from extracted  $R_P$  and  $R_S$  using  $L2$  norm fitting. The data used for extraction is shown in Figure 3.25.

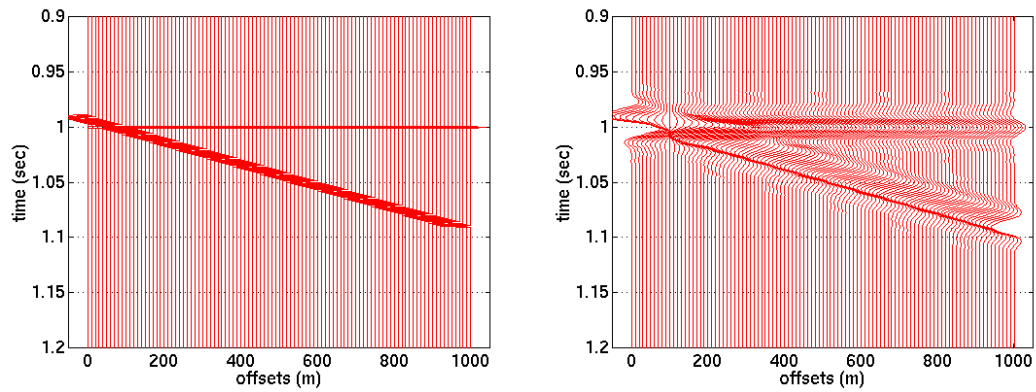


Figure 3.27. A reflection model with primary reflection contaminated by linear noise. The linear event crosses over primary reflection event at near offsets. The reflectivities versus offsets are on the left side. The right side is the AVO gather created by convolution of reflectivities with bandpass filter of 5-10-60-70 Hz. At 1.0s  $D/A_{exp}=36.8\%$ .

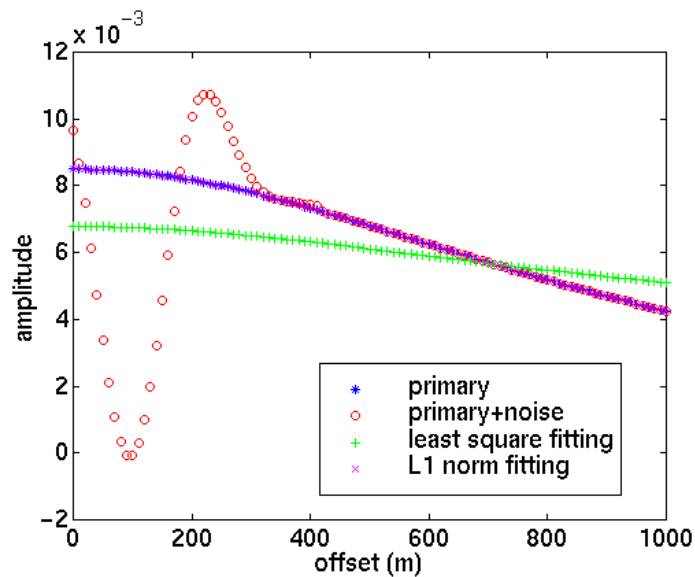


Figure 3.28. The exact primary reflection amplitude, linear noise polluted primary reflection amplitude, recovered amplitude from extracted  $R_P$  and  $R_S$  using  $L1$ , and recovered amplitude from extracted  $R_P$  and  $R_S$  using  $L2$  norm fitting. The data used for extraction is shown in Figure 3.27.

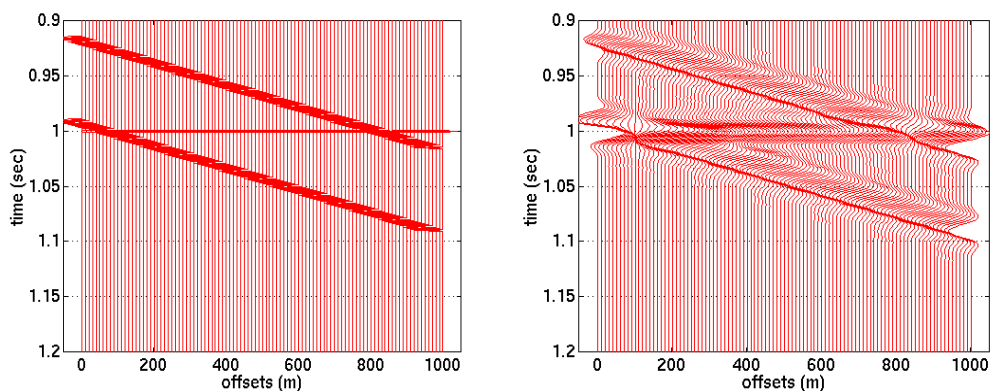


Figure 3.29. A reflection model with primary reflection contaminated by two linear noise events. The two linear events cross over the primary reflection event at the near and far offsets. The two linear events possess the same phase. The reflectivities versus offsets are on the left hand side. The right side is the AVO gather created by convolution of reflectivities, with bandpass filter of 5-10-60-70 Hz. At 1.0s  $D/A_{exp}=51.5\%$ .

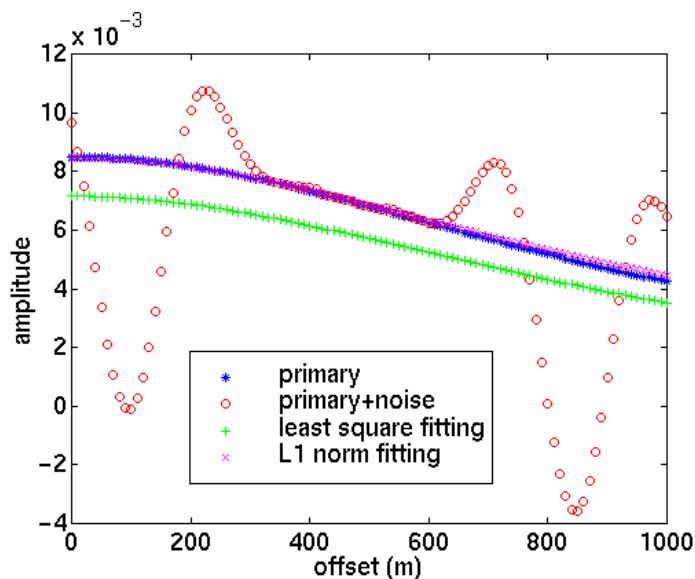


Figure 3.30. The exact primary reflection amplitude, linear noise polluted primary reflection amplitude, recovered amplitude from extracted  $R_p$  and  $R_s$  using  $L1$ , and recovered amplitude from extracted  $R_p$  and  $R_s$  using  $L2$  norm fitting. The data used for extraction is shown in Figure 3.29.

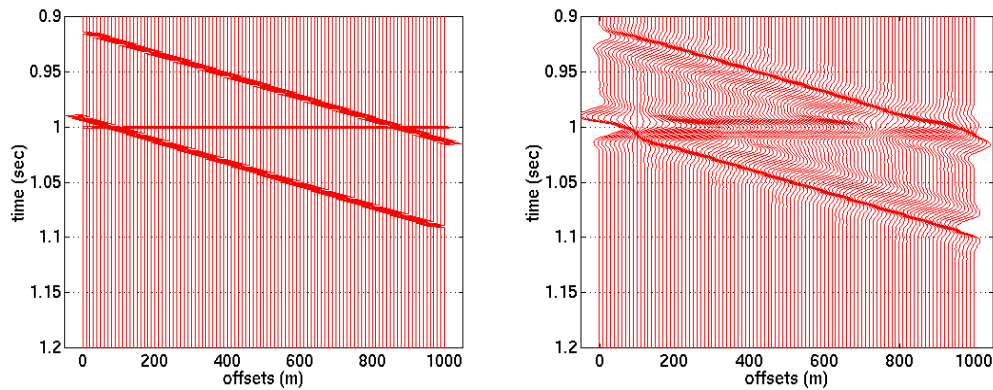


Figure 3.31. A reflection model with primary reflection contaminated by two linear noise events. The two linear events cross over the primary reflection event at the near and far offsets. The linear event at the near offset has reverse polarity compared with primary reflection. The far offset linear event has the same polarity as primary reflection. The reflectivities versus offsets are on the left hand side. The right hand side is the AVO gather created by convolution of reflectivities with bandpass filter of 5-10-60-70 Hz. At 1.0s  $D/A_{exp}=51.5\%$ .

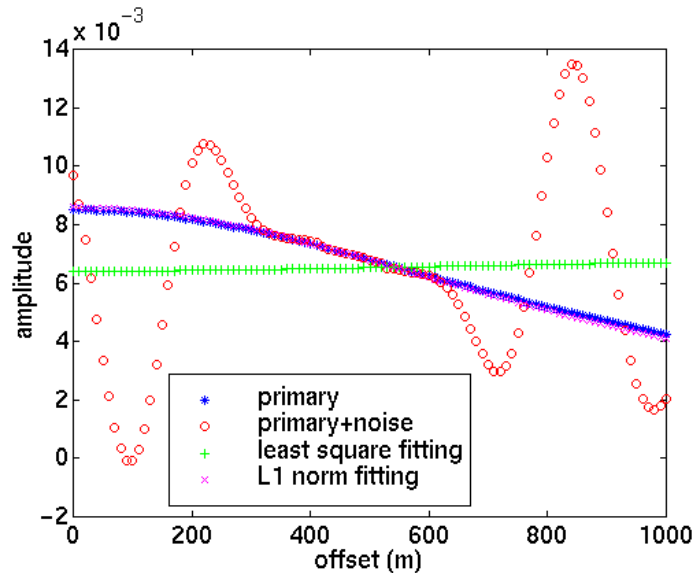


Figure 3.32. The exact primary reflection amplitude, linear noise polluted primary reflection amplitude, recovered amplitude from extracted  $R_P$  and  $R_S$  using  $L1$ , and recovered amplitude from extracted  $R_P$  and  $R_S$  using  $L2$  norm fitting. The data used for extraction is shown in Figure 3.31.

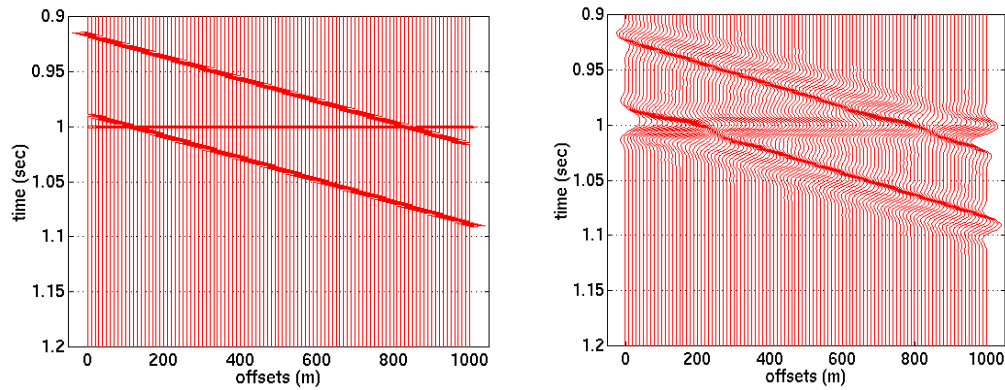


Figure 3.33. A reflection model with primary reflection contaminated by two linear noise events. The two linear events cross over the primary reflection event at the near and far offsets. The linear event at the near has the same polarity as primary reflection. The far offset linear event has reverse polarity. The reflectivities versus offsets are on left side. The right side is the AVO gather created by convolution of reflectivities with bandpass filter of 5-10-60-70 Hz. At 1.0s  $D/A_{exp}=51.5\%$ .

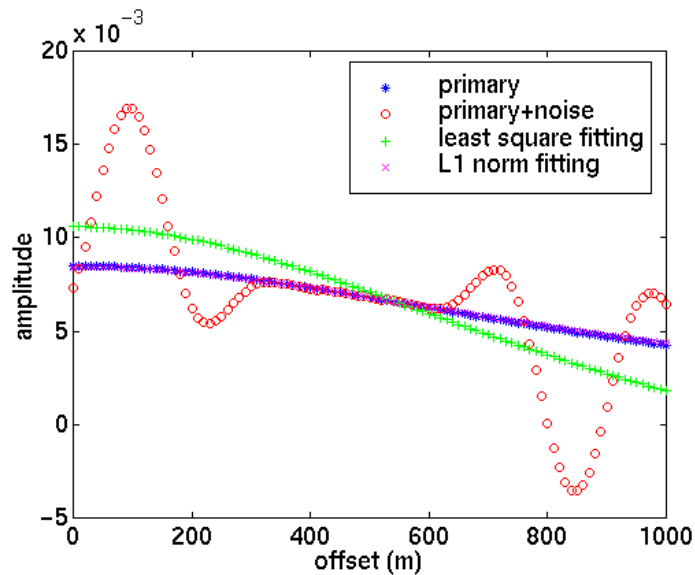


Figure 3.34. The exact primary reflection amplitude, linear noise polluted primary reflection amplitude, recovered amplitude from extracted  $R_P$  and  $R_S$  using  $L1$ , and recovered amplitude from extracted  $R_P$  and  $R_S$  using  $L2$  norm fitting. The data used for extraction is shown in Figure 3.33.

From the fittings of  $L1$  and  $L2$  norms in Figures 3.23 to 3.34, a few observations are found as

- Different linear event positions across the primary and the polarities of the linear event do not change the fitting results too much.
- $L1$  norm fitting does much better job than  $L2$  norm fitting with linear noise existing.
- The fitted  $R_s$  has larger error than fitted  $R_p$ .

### 3.3.2.3. Random noise

Random noise is superposed over the primary reflection. The random noise has uniform distribution. In Figures 3.35, 3.36, and 3.37, the maximum random noises are 10%, 30%, and 50% of the zero offset primary reflection coefficients. Table 3.6 lists the fitting results for these three random noise levels.

Table 3.6 The RMS deviations and errors of fitted  $R_p$  and  $R_s$  for Figures 3.35 to 3.37.

Figures of fitting	Relative Deviations ( $D/A_{exp}$ )	Error of $R_p$ ( $L2$ norm fitting)	Error of $R_s$ ( $L2$ norm fitting)	Error of $R_p$ ( $L1$ norm fitting)	Error of $R_s$ ( $L1$ norm fitting)
Figure 3.35	36.8%	0.271%	1.711%	1.176%	0.588%
Figure 3.36	36.8%	2.906%	5.952%	4.706%	2.94%
Figure 3.37	36.8%	5.306%	8.576%	1.176%	0.588%

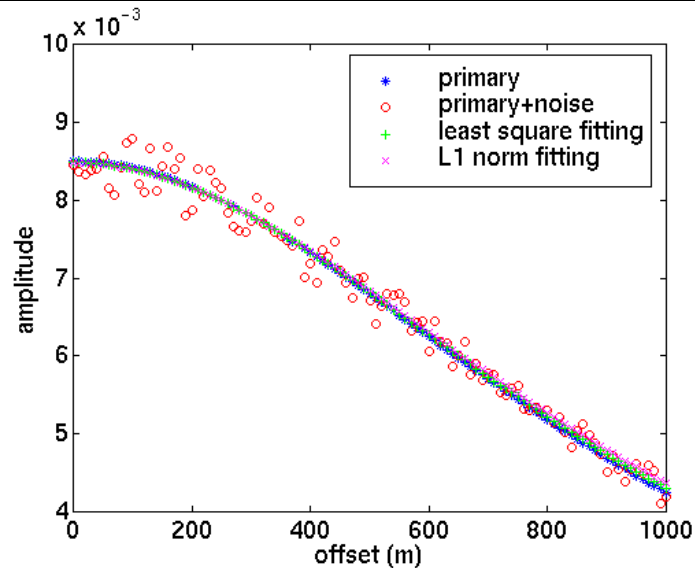


Figure 3.35. The exact primary reflection amplitude, 10% random noise polluted primary reflection amplitude, recovered amplitude from extracted  $R_p$  and  $R_s$  using  $L1$ , and recovered amplitude from extracted  $R_p$  and  $R_s$  using  $L2$  norm fitting.

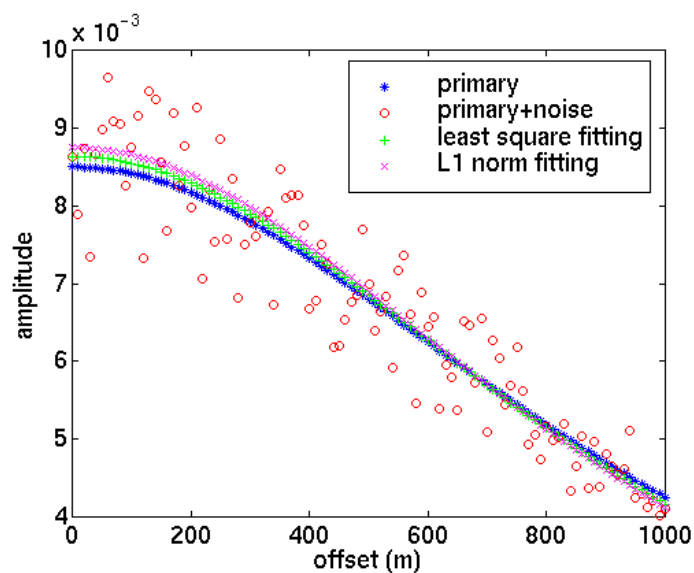


Figure 3.36. The exact primary reflection amplitude, 20% random noise polluted primary reflection amplitude, recovered amplitude from extracted  $R_P$  and  $R_S$  using  $L1$ , and recovered amplitude from extracted  $R_P$  and  $R_S$  using  $L2$  norm fitting.

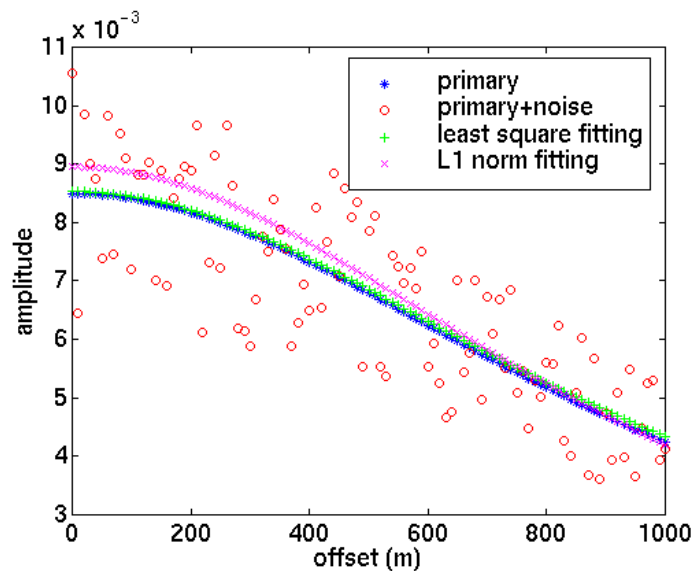


Figure 3.37. The exact primary reflection amplitude, 30% random noise polluted primary reflection amplitude, recovered amplitude from extracted  $R_P$  and  $R_S$  using  $L1$ , and recovered amplitude from extracted  $R_P$  and  $R_S$  using  $L2$  norm fitting.

In the fittings in Figures 3.35 to 3.37,  $L2$  norm fitting works better than  $L1$  norm fitting. The random noise added into the data is uniform distributed. For the Gaussian distribution random noise,  $L2$  norm fitting may work better.

The models used in this section to test  $L1$  and  $L2$  norm fittings are ideal and somewhat artificial. In real cases, the noises are much more complex than the examples shown in this section, e.g., the multiple in the real seismic data usually has more than 50%  $D/A_{exp}$ .  $L1$  norm estimation provides an approach which may help suppress multiples and linear noise, provided that the residual moveout of multiples is large and that the offset range on a CDP gather is big enough to make the multiple stand out.

### 3.4. DECOUPLING LITHOLOGY CHANGE BY CROSSPLOTTING $\frac{\Delta\lambda}{\lambda+2\mu}$ AND

$$\frac{\Delta\mu}{\lambda+2\mu}$$

Using Lamé's parameters ( $\lambda\rho$  and  $\lambda/\mu$ ) as direct hydrocarbon indicator was started by Goodway et al. (1997). In their realization, the  $P$  and  $S$  wave reflectivity is extracted using an approximation of reflection coefficient described by Fatti et al. (1994) (see equation 3.5). The  $P$  and  $S$  wave impedance are inverted from the reflectivity and the  $\lambda\rho$  and  $\lambda/\mu$  are calculated from inverted impedance. In the extraction of reflectivity, the background  $V_p/V_s$  ratio is required. In the realization, the validation background  $V_p/V_s$  ratio and non-uniqueness of the inversion algorithms have to be taken with caution. After Goodway et al., Xu and Bancroft seek to directly extract Lamé's parameters from seismic data (1997, 1998) without inversion of impedance. As described in section 3.1.1.7, they

obtained an intermediate result as  $\frac{\Delta\lambda}{\lambda+2\mu}$ ,  $\frac{\Delta\mu}{\lambda+2\mu}$ ,  $\frac{\Delta\kappa}{\kappa+\frac{4}{3}\mu}$ , and  $\frac{\Delta\mu}{\kappa+\frac{4}{3}\mu}$ . In the

extraction of above intermediate result, the background  $V_p/V_s$  ratio is not required. However, to invert these results to absolute value of Lamé's parameters, they used background  $V_p/V_s$  ratio to calculate reflectivities that may be inverted into absolute value using existing inversion algorithms. Although  $\frac{\Delta\lambda}{\lambda+2\mu}$  and  $\frac{\Delta\mu}{\lambda+2\mu}$  are intermediate results to obtain information comparable with well logs, the studies in this thesis show that they are good AVO attributes helpful to decouple the lithologies indicated by varying  $V_p/V_s$  ratios.

In terms of the *a priori* information, especially the  $V_p/V_s$  ratio background, used in the extraction methodologies, AVO attributes (extracted using equations after Shuey, Fatti et al., Smith & Gidlow, Xu & Bancroft, and Gray) can be classified into two kinds: with (class I) or without (class II) background  $V_p/V_s$  ratio in the extraction. Intercept and gradient attributes are extracted using Shuey's equation without such background

information required.  $\frac{\Delta\lambda}{\lambda+2\mu}$ ,  $\frac{\Delta\mu}{\lambda+2\mu}$ ,  $\frac{\Delta\kappa}{\kappa+\frac{4}{3}\mu}$ , and  $\frac{\Delta\mu}{\kappa+\frac{4}{3}\mu}$  extracted using Xu &

Bancroft's equation do not require  $V_p/V_s$  ratio information. However,  $V_p/V_s$  ratio background is needed for the inversion of absolute value of attributes. Other extraction methods need such a background, such as  $R_p$  and  $R_s$  (Fatti et al.),  $\Delta V_p/V_p$  and  $\Delta V_s/V_s$  (Smith & Gidlow), and  $\Delta\lambda/\lambda$  and  $\Delta\mu/\mu$  (Gray). The significance to emphasize such a classification is that the error of incorrect  $V_p/V_s$  ratio in the extraction may cause error of extracted attributes. Usually, a constant  $V_p/V_s$  ratio as 2 or a single  $V_p/V_s$  ratio time curve for whole seismic line may underestimate reservoir or overestimate the lithologic change, especially for the shallow sediments. For example, when the  $V_p/V_s$  ratio of 2 is for overburden shale and  $V_p/V_s$  ratio of 1.6 is for gas sand, the assumption of background  $V_p/V_s$  of 2 may cause more than 10% error for extracted S reflectivity, if two-term approximation as Fatti's approximation (equation 3.5) is used to do extraction. Such an error may underestimate the anomaly caused by reservoir.

Because of the above advantage of class II extractions, it is beneficial to study the intermediate extracted attributes from this kind of method (intercept and gradient,  $\frac{\Delta\lambda}{\lambda+2\mu}$  and  $\frac{\Delta\mu}{\lambda+2\mu}$ ,  $\frac{\Delta\kappa}{\kappa+\frac{4}{3}\mu}$  and  $\frac{\Delta\mu}{\kappa+\frac{4}{3}\mu}$ ). Intercept and gradient have been utilized since the early age of AVO techniques. The other four attributes mentioned in the above brackets are rarely used.

The framework for interpretation of intercept and gradient is given by Castagna et al. (1998). The guideline for crossplotting the intercept and gradient is given in their publication. In the following, the framework for crossplotting  $\frac{\Delta\lambda}{\lambda+2\mu}$  and  $\frac{\Delta\mu}{\lambda+2\mu}$  is tied to build. Crossplotting intercept and gradient is compared with crossplotting  $\frac{\Delta\lambda}{\lambda+2\mu}$  and  $\frac{\Delta\mu}{\lambda+2\mu}$  in terms of differentiation of lithology changes.

### 3.4.1 Crossplot of $\Delta\mu/(\lambda+2\mu)$ and $\Delta\lambda/(\lambda+2\mu)$ for 25 set of samples (Castagna, 1994)

Table 3.7 Properties for 25 set of sand and shale samples (Castagna et al., 1994)

Brine sand			shale			Gas sand		
Vp	Vs	$\rho$	Vp	Vs	$\rho$	Vp	Vs	$\rho$
km/s	km/s	g/cc	km/s	km/s	g/cc	km/s	km/s	g/cc
3.28	1.68	2.19	3.27	1.65	2.20	3.04	1.74	2.05
4.06	2.03	2.40	4.69	2.61	2.49	3.70	2.06	2.26
3.85	2.24	2.24	2.77	1.52	2.29	3.08	2.34	2.14
4.06	2.34	2.30	4.06	2.18	2.58	3.62	2.58	2.30
3.21	1.79	2.22	3.05	1.69	2.34	2.91	1.85	2.01
4.55	2.61	2.44	3.21	1.60	2.39	3.96	2.80	2.41
3.05	1.56	2.40	2.77	1.27	2.45	2.69	1.59	2.25
3.42	1.78	2.53	2.77	1.45	2.67	3.39	1.79	2.50
2.52	0.90	2.11	2.31	0.85	2.18	1.58	0.94	1.94
3.44	1.94	2.52	2.75	1.26	2.43	3.19	1.98	2.45
3.55	1.54	2.38	3.51	1.85	2.46	3.47	1.75	2.21
5.03	3.32	2.61	3.60	1.85	2.63	4.91	3.30	2.59
2.07	0.81	2.10	1.94	0.77	2.10	1.54	0.98	2.05
2.69	1.38	2.13	2.67	1.13	2.29	2.07	1.29	2.02
2.19	1.21	2.15	2.10	1.03	2.10	1.68	1.15	2.10
2.52	1.20	2.24	2.59	1.39	2.30	1.86	1.16	2.09
3.81	2.30	2.25	3.81	2.26	2.40	3.45	2.02	2.10
2.66	1.25	2.23	2.38	0.94	2.27	2.25	1.30	2.06
2.84	1.47	2.08	2.74	1.39	2.06	2.84	1.76	2.08
2.13	0.67	1.90	1.83	0.40	2.02	1.44	0.58	1.53
3.05	1.46	2.30	3.35	1.72	2.36	2.18	1.37	2.19
3.46	1.85	2.26	2.31	0.94	1.90	3.04	1.92	2.09
2.11	0.93	2.11	2.10	0.64	2.14	1.42	0.97	1.97
3.21	1.85	2.17	2.87	1.30	2.27	2.93	1.79	1.96
4.35	2.34	2.40	2.77	1.52	2.30	4.05	2.38	2.32

Castagna (1994, 1998) used 25 sets of brine sand, gas sand, and shale samples all over the world to test the guideline to crossplot intercept and gradient. These samples are referred in this thesis to crossplot the relative change of Lamé's parameters. Table 3.7 lists all the properties of 25 set samples for different rocks.

Using  $V_p$ ,  $V_s$  and density in table 3.7, Lamé's parameters ( $\lambda$  and  $\mu$ ) are calculated. The changes of Lamé's parameters ( $\Delta\lambda$  and  $\Delta\mu$ ) from shale to brine sand and from shale to gas sand are calculated also. The normalized changes of Lamé's parameters ( $\Delta\lambda/(\lambda+2\mu)$  and  $\Delta\mu/(\lambda+2\mu)$ ) are also calculated. Figure 3.38 shows the crossplot of  $\Delta\mu$  and  $\Delta\lambda$  for 25 sets of samples. The difference between shale and gas sand is greatly different from the difference between shale and brine sand in terms of  $\Delta\lambda$ . Most samples show negative  $\Delta\lambda$  when gas charges. The cyan lines in this figure connect samples from same area. Figure 3.39 is the crossplot of  $\Delta\mu/(\lambda+2\mu)$  and  $\Delta\lambda/(\lambda+2\mu)$  for 25 sets of samples. It shows the similar or seemly better separation of gas saturation from brine saturation, compared with Figure 3.38.

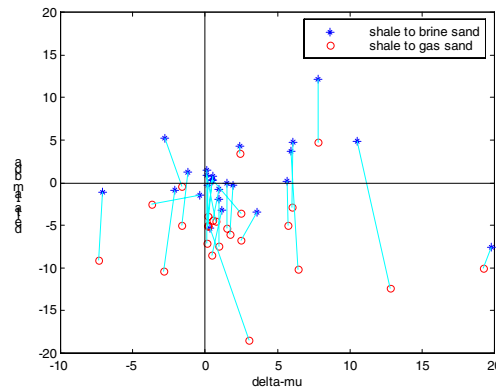


Figure 3.38. Crossplot of  $\Delta\mu$  and  $\Delta\lambda$  for 25 sets of samples.

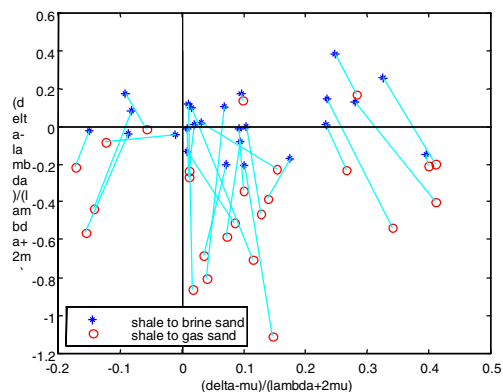


Figure 3.39. Crossplot of  $\Delta\mu/(\lambda+2\mu)$  and  $\Delta\lambda/(\lambda+2\mu)$  for 25 sets of samples.

Figure 3.40 and Figure 3.41 display  $\Delta\lambda$  and  $\Delta\mu$  in different manner from Figure 3.38 and Figure 3.39. Figure 3.40 shows that  $\Delta\lambda$  and  $\Delta\mu$  have similar size for different sets of samples of brine sand and shale, while  $\Delta\lambda$  and  $\Delta\mu$  exhibit much greater difference in Figure 3.41 when gas is charged in sand. Figure 3.42 and Figure 3.43 do the similar comparisons as Figure 3.40 and Figure 3.41 do, with the normalized Lamé's parameter changes ( $\Delta\mu/(\lambda+2\mu)$  and  $\Delta\lambda/(\lambda+2\mu)$ ) used and with slightly better separation effect.

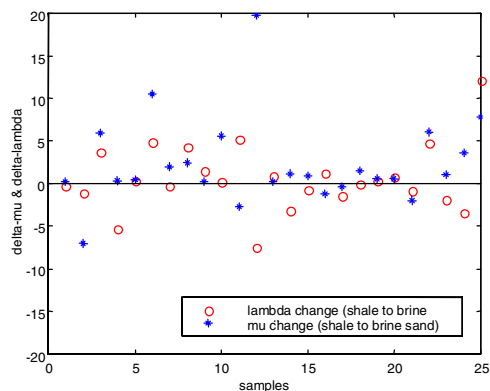


Figure 3.40.  $\Delta\mu$  and  $\Delta\lambda$  for 25 sets of samples (shale to brine sand).

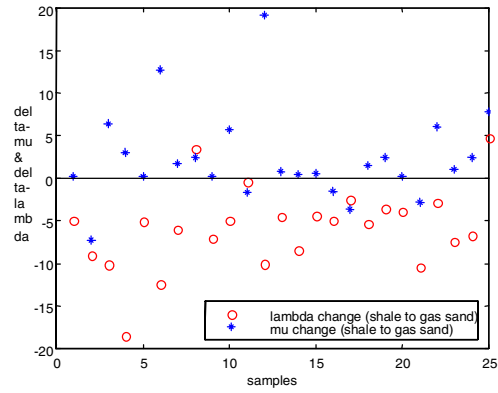


Figure 3.41.  $\Delta\mu$  and  $\Delta\lambda$  for 25 sets of samples (shale to gas sand).

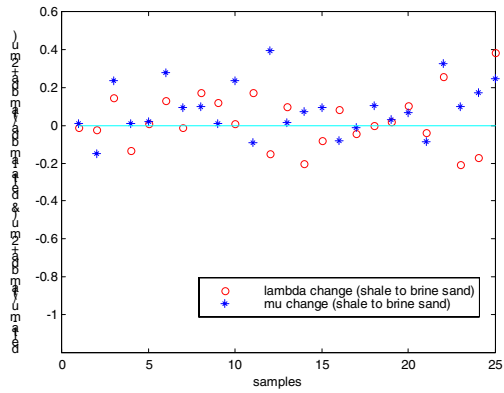


Figure 3.42.  $\Delta\mu/(\lambda+2\mu)$  and  $\Delta\lambda/(\lambda+2\mu)$  for 25 sets of samples (shale to brine sand).

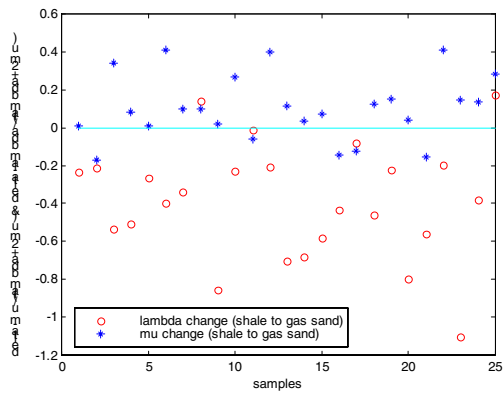


Figure 3.43.  $\Delta\mu/(\lambda+2\mu)$  and  $\Delta\lambda/(\lambda+2\mu)$  for 25 sets of samples (shale to gas sand).

### 3.4.2. Relationship between $\Delta\mu/(\lambda+2\mu)$ and $\Delta\lambda/(\lambda+2\mu)$

Interpreters are used to the linear relationships between  $V_p$  and  $V_s$ . Castagna et al. derived the guideline between intercept and gradient AVO attributes from such linear relationships and Gardner's relationship between  $V_p$  and density. In the similar manner, the relationship between  $\frac{\Delta\lambda}{\lambda+2\mu}$  and  $\frac{\Delta\mu}{\lambda+2\mu}$  may be derived from the correlation between  $V_p$ ,  $V_s$  and  $\rho$ , the deviation from which is attributable to hydrocarbons or unusual lithologies. In the following, the relationships between  $\frac{\Delta\lambda}{\lambda+2\mu}$  and  $\frac{\Delta\mu}{\lambda+2\mu}$  are given for three cases of the correlation between  $V_p$ ,  $V_s$  and  $\rho$ , which is commonly used in the practice.

#### 1) Constant $V_p/V_s$ and constant density:

The relationship between  $\Delta\mu/(\lambda+2\mu)$  and  $\Delta\lambda/(\lambda+2\mu)$  is

$$\frac{\Delta\lambda}{\lambda+2\mu} = \left( \frac{V_p^2}{V_s^2} - 2 \right) \frac{\Delta\mu}{\lambda+2\mu}$$

Figure 3.44 illustrates above relationship on the crossplot domain for different  $V_p/V_s$  ratios.

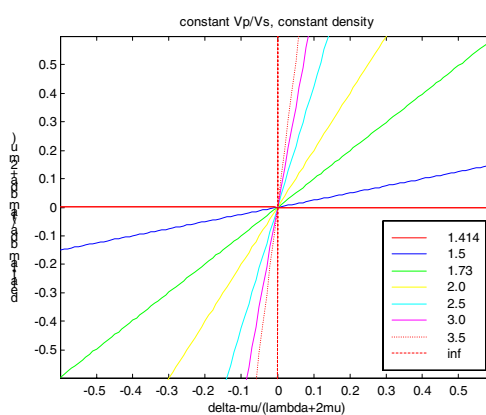


Figure 3.44.  $\Delta\mu/(\lambda+2\mu)$  and  $\Delta\lambda/(\lambda+2\mu)$  assuming constant  $V_p/V_s$  and constant density.  $V_p/V_s$  increase counterclockwise.

The distribution of  $\frac{\Delta\lambda}{\lambda+2\mu}$  and  $\frac{\Delta\mu}{\lambda+2\mu}$  occupies 1<sup>st</sup> and 3<sup>rd</sup> quadrants. Smaller

$V_p/V_s$ , closer to zero is  $\frac{\Delta\lambda}{\lambda+2\mu}$ .

2) Linear  $V_p$  versus  $V_s$  and constant density:

Suppose  $V_p$  and  $V_s$  has linear relationship as  $V_p = aV_s + b$ .

$$\frac{\Delta\lambda}{\lambda+2\mu} = \left(a \frac{V_p}{V_s} - 2\right) \frac{\Delta\mu}{\lambda+2\mu}$$

Figure 3.45 shows the distributions of  $\Delta\mu / (\lambda+2\mu)$  and  $\Delta\lambda / (\lambda+2\mu)$  for the assuming linear  $V_p$  versus  $V_s$  and constant density. It can be seen that the  $V_p/V_s$  ratios of around 2.0 take more area the other  $V_p/V_s$  ratio in this crossplot domain. This suggests that the  $V_p/V_s$  ratio may be well differentiated by such a crossplot for the common cases. Figure 3.45 also show the difference of slopes of  $V_p$  versus may not cause large change of the distribution of  $\Delta\mu / (\lambda+2\mu)$  and  $\Delta\lambda / (\lambda+2\mu)$ .

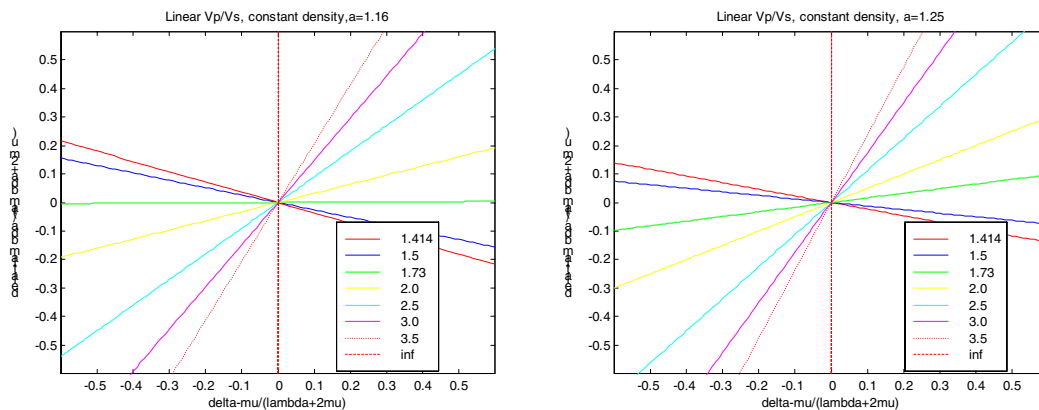


Figure 3.45.  $\Delta\mu / (\lambda+2\mu)$  and  $\Delta\lambda / (\lambda+2\mu)$  assuming linear  $V_p$  versus  $V_s$  and constant density.  $V_p/V_s$  increase counterclockwise. On the left, the slope of  $V_p$  versus  $V_s$  is 1.16; on the right the slope is 1.25.

3) Linear  $V_p$  versus  $V_s$ , and Gardner density

Suppose  $V_p$  and  $V_s$  has linear relationship as  $V_p = aV_s + b$ . and the Gardner's relationship is  $\rho = mV_p^g$

$$\frac{\Delta\lambda}{\lambda+2\mu} = C \frac{\Delta\mu}{\lambda+2\mu}$$

where

$$C = \frac{2}{2 + a^2 g \frac{V_S}{V_P}} \left( \left( a \frac{V_P}{V_S} - 2 \right) - a g \frac{V_P}{V_S} \left( 2 \frac{V_S^2}{V_P^2} - 1 \right) \right)$$

Figure 3.46 shows a similar map to Figure 3.45. The density versus P velocity relationship has small effect. This figure shows same suggestion as Figure 3.45.

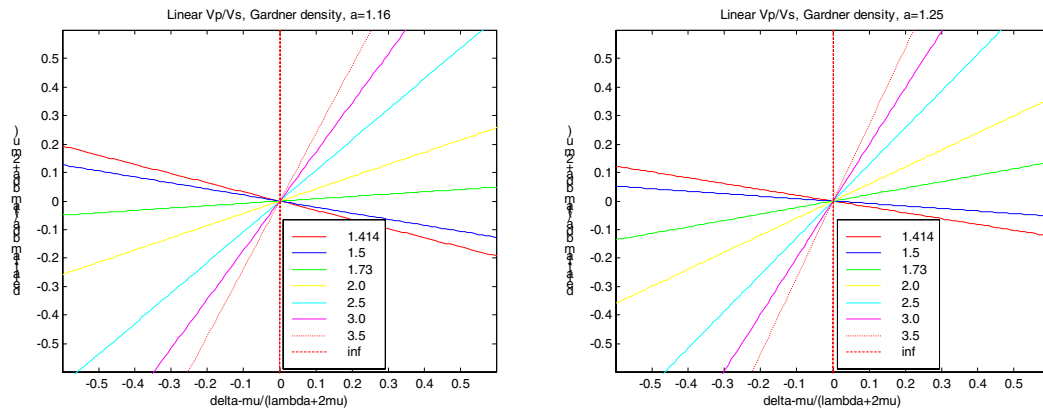


Figure 3.46.  $\Delta\mu/(\lambda+2\mu)$  and  $\Delta\lambda/(\lambda+2\mu)$  assuming linear Vp versus Vs and Gardner density ( $g=0.25$ ). Vp/Vs increase counterclockwise. On the left, the slope of Vp versus Vs is 1.16; on the right the slope is 1.25.

Figure 3.47 overlies the 25 sets of samples on the crossplot diagram assuming linear Vp versus Vs and Gardner density. The samples do not all fall into the areas delimited by the lines corresponding to the different Vp/Vs ratio. The reason is that the samples are from over all the world. It is not necessary the linear relationship between Vp and Vs suitable for all rocks. The gas saturation and brine saturation can be separated.

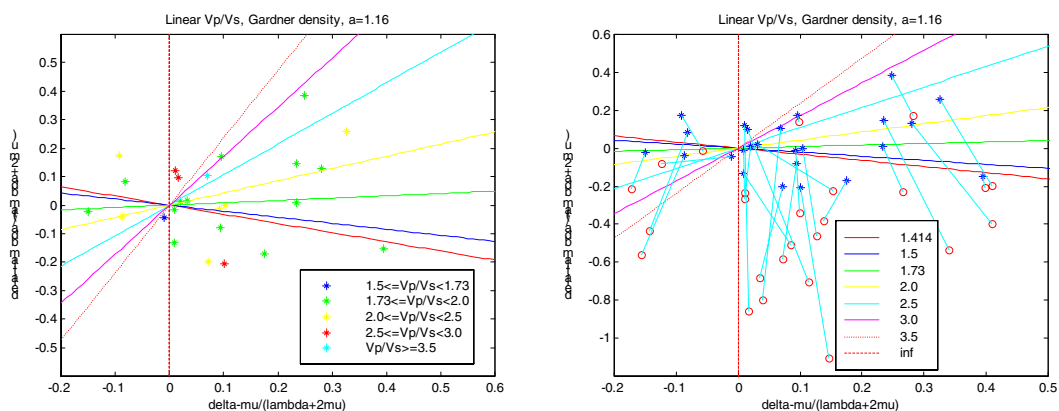


Figure 3.47. 25 sets of samples overlaid the relationship between  $\Delta\mu/(\lambda+2\mu)$  and  $\Delta\lambda/(\lambda+2\mu)$  assuming linear Vp versus Vs and Gardner density. The slope of Vp versus Vs is 1.16. On the right, the circles ('o') are for shale to gas sand; the '\*'s for shale to brine sand.

### 3.4.3. Decoupling of lithology by crossplotting

Examples are used in this subsection to demonstrate the crossplot of AVO attributes in terms of the differentiation of varying Vp/Vs ratio, which is usually an indicator of lithology changes.

The Vp velocity and density in the examples are obtained from well sonic logs, while the Vs is calculated from Castagna's mud-rock line:

$$V_p = 1.16 V_s + 1360.$$

Figure 3.48 shows the crossplot of Vp and Vs, which display a perfect line. Figure 3.49 displays the crossplot of reflectivities: Rp and Rs, and the intercept and gradient are crossplotted in Figure 3.50. At last,  $\Delta\mu/(\lambda+2\mu)$  and  $\Delta\lambda/(\lambda+2\mu)$  is crossplotted in Figure 3.51. The Vp/Vs ratios are displayed in different colors for each crossplot.

From the comparisons among Figures 3.49, 3.50, and 3.51, it is found that Vp/Vs ratio can not be differentiated on the crossplot of Rp and Rs or intercept and gradient, although crossplot of intercept and gradient is better than crossplot of Rp and Rs. However, Vp/Vs ratio is separated very well in the crossplot of  $\Delta\mu/(\lambda+2\mu)$  and  $\Delta\lambda/(\lambda+2\mu)$ .

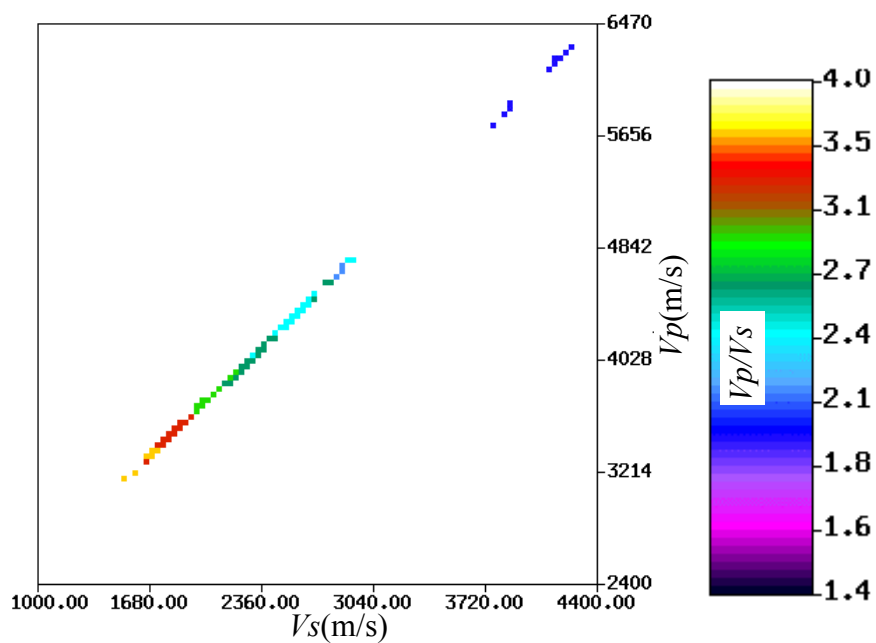


Figure 3.48. Crossplot of  $V_p$  and  $V_s$  for the linear  $V_p$  versus  $V_s$  model.

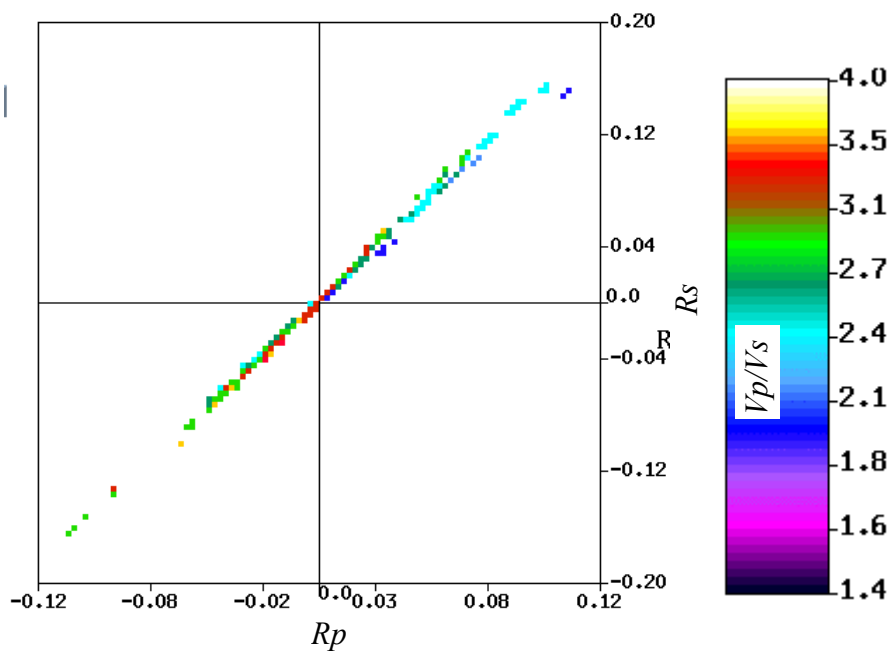


Figure 3.49. Crossplot of  $R_p$  and  $R_s$  for the linear  $V_p$  versus  $V_s$  model.

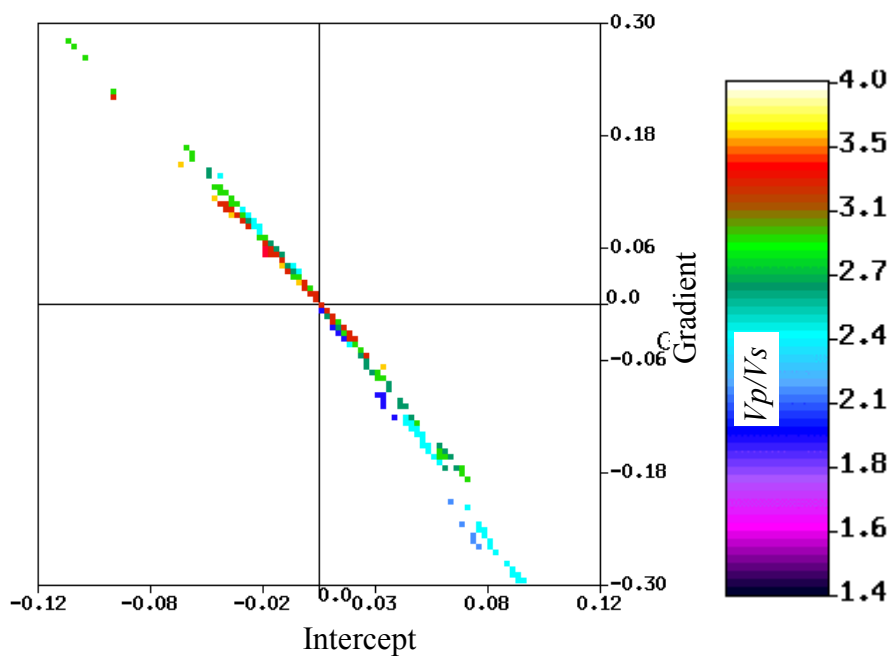


Figure 3.50. Crossplot of intercept and gradient for the linear  $V_p$  versus  $V_s$  model.

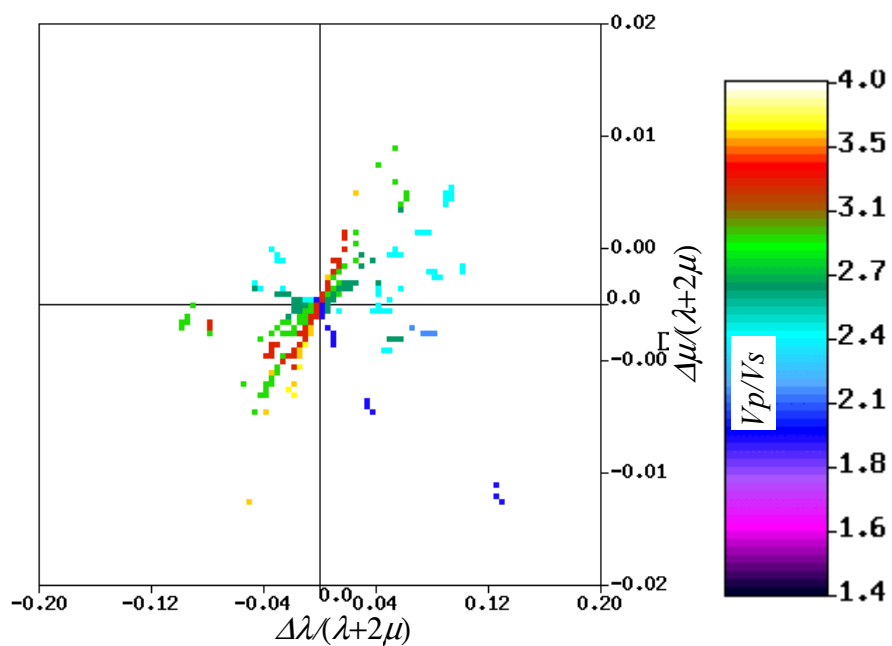


Figure 3.51. Crossplot of  $\Delta\lambda(\lambda+2\mu)$  and  $\Delta\mu(\lambda+2\mu)$  for the linear  $V_p$  versus  $V_s$  model.

### 3.5. AVO WITH EQUIVALENT OFFSET MIGRATION

AVO analysis is difficult for the data with geologic structures. It is ideal to apply migration before AVO analysis so that the amplitude may be preserved and the structure restored. In this thesis, the combination of AVO and equivalent offset migration is studied.

Bancroft et al. (1995) introduces a pre-stack migration method called equivalent offset migration EOM. EOM is a two step process: the first being a gathering process that forms common scatterpoint (CSP) gathers, and the second a simplified Kirchhoff NMO correction and stack to zero offset performed on the CSP gathers. CSP gathers contain a greater amount of information than conventional CMP gathers because they contain all input traces within the prestack migration aperture. These traces are sorted by an equivalent offset into bins in the CSP gather with no time shifting. The energy from these traces, which is typically associated with CMP gathers and poststack migration, is now combined into one CSP gather to produce a compounded distribution of energy. The AVO analysis, therefore, based on CSP gathers may have better effect than pre-migration CMP gathers, especially for the data set with geologic structures.

Common scatterpoint (CSP) gathers are formed at each output trace location similar to CMP gathers. The offset of each input trace is uniquely computed for each CSP location, and is based on the distance of the source and receiver relative to the CSP location. Figure 3.52 (a) shows the ray paths for a given source and receiver travelling to and from a scatter point. The source and receiver are collocated at an imaginary surface position that maintains the same time  $T$ , thus defining the equivalent offset  $h_e$ . Equating travel times gives

$$T = \left( T_0^2 + \frac{(x+h)^2}{V^2} \right)^{1/2} + \left( T_0^2 + \frac{(x-h)^2}{V^2} \right)^{1/2} = 2 \left( T_e^2 + \frac{h_e^2}{V^2} \right)^{1/2}, \quad (3.26)$$

where  $x$  is the surface distance from the CSP location to the CMP location,  $h$  the half source-receiver offset,  $T_0$  the vertical one-way traveltime, and  $V$  the RMS velocity defined at the scatter point. Solving for  $h_e$  gives

$$h_e^2 = x^2 + h^2 - \frac{4x^2h^2}{T^2V^2}. \quad (3.27)$$

The reflection point in Figure 3.52 (b) is observed to lie on a hyperbolic moveout path at the equivalent offset  $h_e$ , while still maintaining the original input time  $T$  as required by equation (3.26).

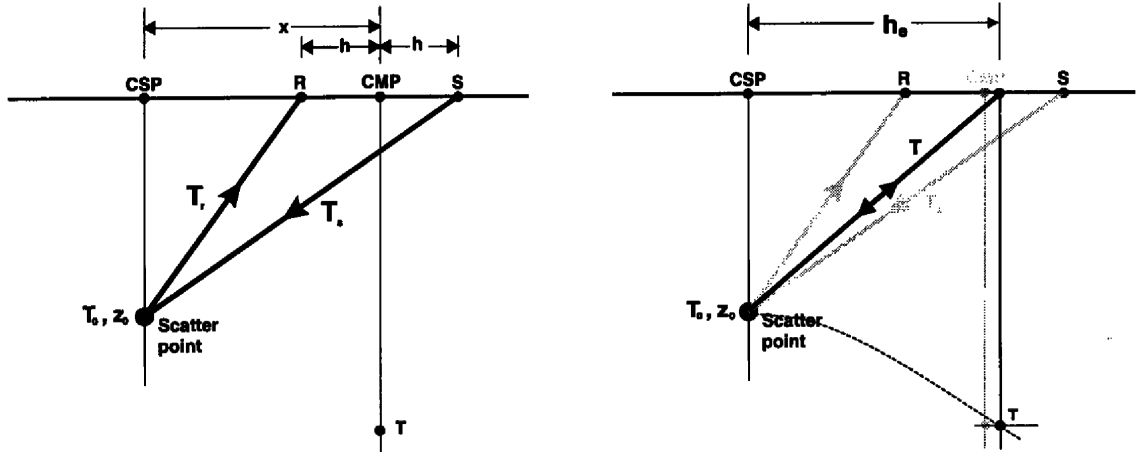


Figure 3.52. Ray diagram for a) a given source and receiver, and b) a collocated source and receiver that defines the equivalent offset.

The equivalent offset is defined from source and receiver locations to scatterpoints located below a surface position of the migrated output trace (Bancroft et al. 1996). Samples in each input trace, within the prestack migration aperture, are assigned an equivalent offset and then summed into offset bins of the CSP gather. The equivalent offset in equation (3.27) includes a time and velocity dependence which may spread an input trace across a number of offset bins. Equation (3.27) is only computed at the transition times where the input trace moves from one input bin to another.

In EOM, NMO correction and stacking of the CSP gathers completes the migration process. However, this process can not simply be regarded as an amplitude preserving process. The combination of EOM with elastic wave propagation theory may help solve this problem and further research is required. EOM is not done in common offset planes, so the information at different offset may interfere and distort the AVO response. In this thesis, the conventional AVO routine is applied to CSP gathers as done on CMP gathers and comparisons of both are made. Before AVO analysis is applied,

traces in the CSP gathers are energy-balanced over big time window that is within muting gate.

# **CHAPTER 4 AVO ANALYSIS OF 10HZ 3C-2D LINE IN BLACKFOOT**

## **4.1. BLACKFOOT SURVEY**

A 4.0 km 3C-2D broadband seismic line was acquired over the Blackfoot Field near Strathmore, Alberta, in the summer of 1995. The acquisition and subsequent processing of the data are discussed in CREWES research report (Gallant et al., 1995; Bertram et al., 1995; Gorek et al., 1995). This thesis discusses the AVO analysis of the vertical and radial components from this seismic line.

The Blackfoot Field is located in Township 23, Range 23, West of the 4th Meridian, in south central Alberta (Figure 4.1). The targets are Glauconitic incised valleys in the Lower Mannville Group of the Lower Cretaceous. The 3C-2D seismic line 950278 crosses one such valley, as shown in Figure 4.1. This map is an isopach of channel thickness based on well control and 3-D seismic data; it indicates gross thickness of the channel fill, but no lithologic distinctions (Politylo, A., 1995, personal communication). The channel facies consists primarily of very fine to medium grained quartz sandstone, with porosities averaging 18%, though it shales out in some locations.

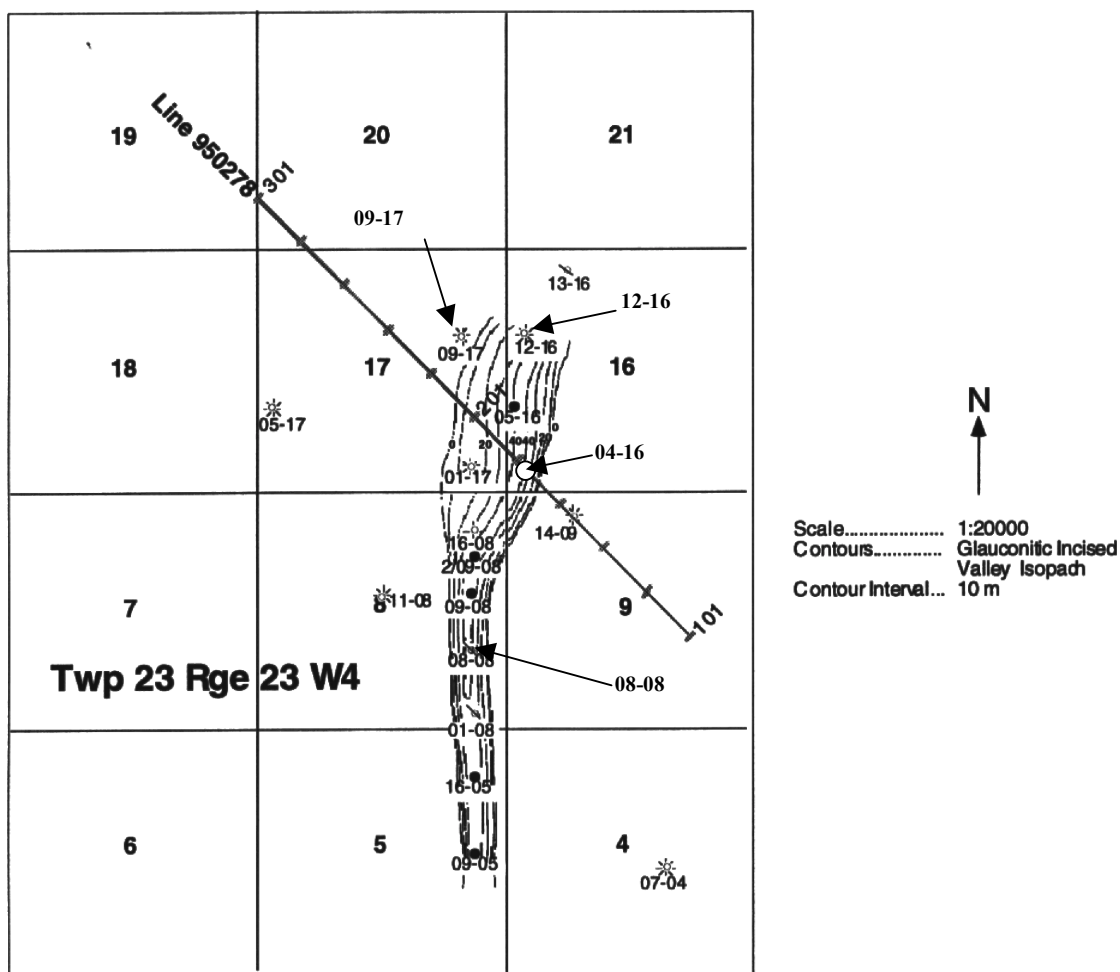


Figure 4.1. Location map of 3C-2D seismic line 950278, well control and the incised valley isopach (Miller et. al., 1995).

The 3-C survey had two primary exploration objectives: to distinguish channel from regional facies; and to determine sand/shale ratios within the incised valley systems. Additionally, this 2-D dataset served as a template for the acquisition, processing and interpretation of the 3C-3D seismic survey conducted over this same field in November, 1995. Modeling and interpretive studies of the broadband 3C-2D dataset have been done by researchers on the CREWES project. Work has also been done in the AVO analysis of this line. Vladan et al (1996), e.g., studied the AVO phenomena with AVO model and amplitude measurements of the real data, and Ferguson et al. (1996) inverted the vertical and the radial components to impedance domain.

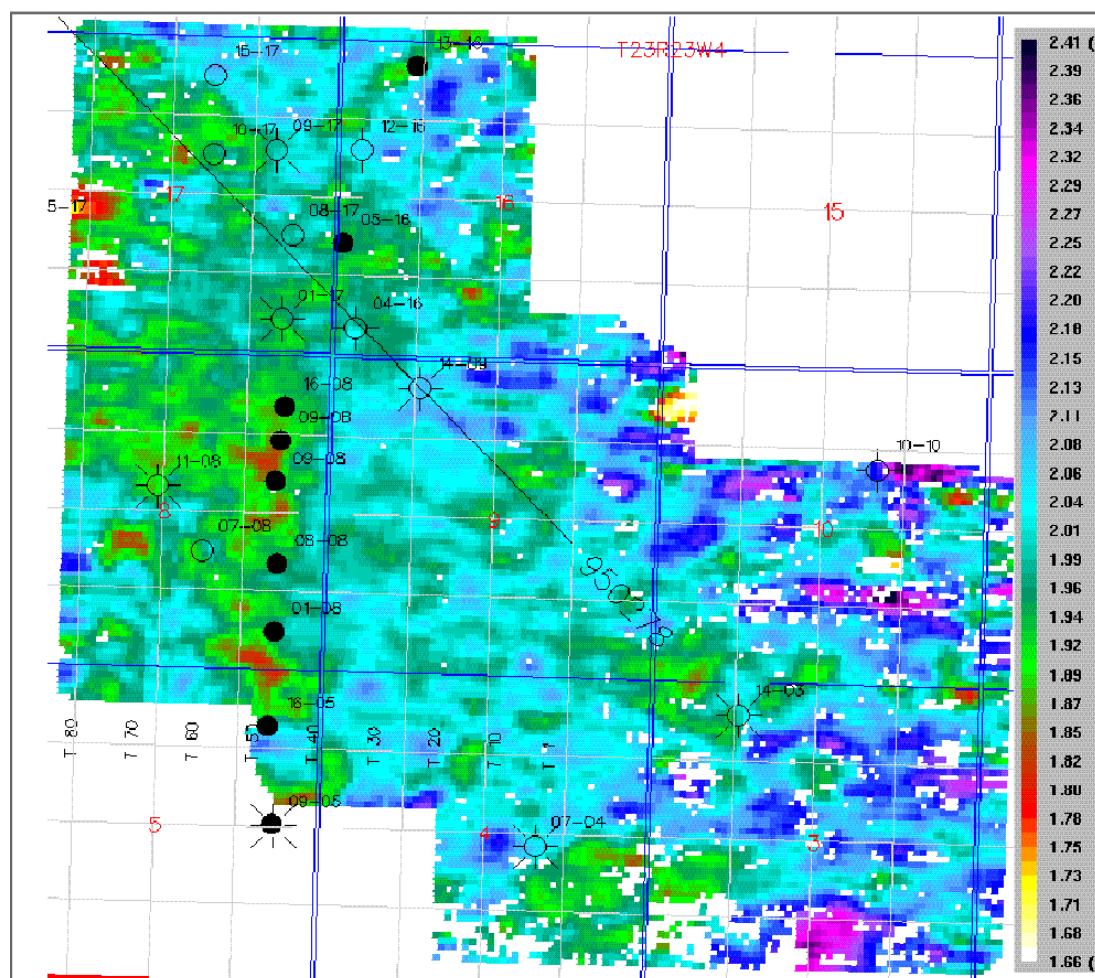


Figure 4.2.  $V_p/V_s$  map from Lower Mannville to Wabamun (Yang et al, 1996).

A 3C-3D seismic survey was also conducted in this area to evaluate the effectiveness of integrated  $P$ - $P$  and  $P$ - $S$  surveys for improved hydrocarbon exploration.  $V_p/V_s$  ratio analysis, using  $P$ - $S$  isochron and  $P$ - $P$  isochron, was done by Grace Yang and other staff on the CREWES project. Figure 4.2 presents the  $V_p/V_s$  map from Lower Mannville to Wabamun. On the map, the 3C-2D line crosses the higher  $V_p/V_s$  ratio zone of the incised valley.

In this thesis, both radial and vertical components of the 3C-2D line are studied. However, most attention is paid to the vertical component data, as it relates to  $P$ - $P$  reflection while the radial component relates to converted wave, or  $P$ - $S$  reflection. Data quality is one concern. The signal to noise ratio on radial component is worse than on the

vertical component. Also because of the nature of converted waves, the strength of the energy partitioned to converted wave is small.

In this chapter, the mud-rock line, the linear relationship between  $V_p$  and  $V_s$ , is analyzed using wells with shear sonic logs in Blackfoot. Lamé's parameters are extracted from vertical component.  $P$  and  $S$  wave reflectivities, which are also extracted from vertical component data, allow for calculation of the fluid factor. At the end of this chapter,  $S$  wave reflectivity is extracted from radial component data.

## 4.2. STATISTICAL RELATIONSHIP BETWEEN $V_P$ AND $V_S$ FROM WELL LOGS

### 4.2.1. Review of fluid factor method

As discussed in Chapter 3, the fluid factor method was developed to look for the anomalies that deviate from the statistical relationship between  $V_P$  and  $V_S$  (Smith and Gidlow, 1987). In this fluid factor method, the fluid factor is defined as

$$\Delta F = \frac{\Delta V_P}{V_P} - 1.16 \frac{V_S}{V_P} \frac{\Delta V_S}{V_S}. \quad (4.1)$$

Derivation of equation (4.1) uses Castagna's mud-rock line a statistical relationship between  $V_P$  and  $V_S$  (Castagna, et. al., 1985) and defined as

$$V_P = 1.16V_S + 1360, \quad (4.2)$$

where  $V_P$  and  $V_S$  are in m/sec.

Equation (4.2) is widely referred to by many authors; however, it should be tested when it is applied to a local area. If a locally generated relationship between  $V_P$  and  $V_S$  with a similar form to equation (4.2) exists in the survey, then the fluid factor or fluid stack will take advantage of this relationship.

In this thesis, the dipole sonic logs that were collected in the Blackfoot area are analyzed and used to fit the relationship between  $V_P$  and  $V_S$ .

### 4.2.2. Statistical relationship between $V_P$ and $V_S$

There are four wells with shear sonic logs in the survey: 04-16, 08-08, 09-17, and 12-16. Figure 4.1 shows the location of all the wells, including the four wells listed above. The map also shows the 3C-2D seismic line 950278 and the incised valley isopach. The four wells investigated have different depth intervals for the dipole sonics. The 04-16 well has a dipole sonic from the top to the bottom, while the other three have dipoles in the zone of interest. The following table lists the top and bottom depths of the dipole logs of each well.

Table 4.1. The top depth and bottom depth of the dipole logs of the four wells, 04-16, 08-08, 09-17, and 12-16.

Well name	Top (meters)	Bottom (meters)
04-16	135	1647
08-08	1362	1674
09-17	1440	1651
12-16	1229	1629

The compressional and shear wave velocities and the bulk density are plotted respectively for four wells in Figures 4.3 - 4.6. The formation tops are plotted on the well log curves. In this analysis, the samples to be used for each well have been selected carefully. Each well has touched Mississippian carbonate, but the data below the Mississippian formation have not been used in this analysis. Samples with extremely high or low velocity values have not been used. In Figure 4.4, at a depth of 1600 meters, the  $V_P$  is extremely high, but the  $V_S$  is normal. It would not be reasonable to use this small portion in the analysis. Consequently, the  $V_P$  value is limited to 1570 - 5000 m/sec and the shear wave velocity is limited to 500 - 3500 m/sec.

Castagna's mud-rock line equation (4.2) fits a great variety of rocks very well, as is evident from Figure 4.7, which is adapted from the paper of Castagna et. al. (1985). In this analysis, no attempt was made to derive more than one trend line for the selected samples and no further analysis was done to differentiate lithology of the selected samples.

The cross-plots of  $V_P$  and  $V_S$  for the 04-16 well are shown in Figures 4.8 and 4.9. In Figure 4.8, all selected samples above the Mississippian formation are plotted, and the linear relationship from least square fitting is presented as follows:

$$V_{P_{04-16.A}} = 1.30V_{S_{04-16.A}} + 1205. \quad (4.3)$$

In Figure 4.9, the analysis is limited to the data from 1000m to the Mississippian top. The selected data above Mississippian and below 1000 meters is plotted and the linear relationship is found to be:

$$V_{P_{04-16B}} = 1.34V_{S_{04-16B}} + 1150. \quad (4.4)$$

The cross plots on Figures 4.8 and 4.9 for the 04-16 well show good linear relationships between  $V_P$  and  $V_S$  both on full logs and on the limited length of logs. However, the slope of the linear relationship for the deep portion is slightly larger than the slope obtained from full logs. The former is 1.34, and the latter is 1.30. The intercepts of both equations are also slightly different. The intercept of equation (4.3) is 1205, and that of equation (4.4) is 1150.

Castagna's mud-rock line equation is plotted in both Figures 4.8 and 4.9. It can be seen that the selected samples with smaller values for  $V_P$  (2500m/s - 4000m/s) and  $V_S$  (1000m/s - 2000m/s) fit with the mud-rock line reasonably well and that the samples with higher  $V_P$  and  $V_S$  deviated from mud-rock line. Equation (4.3) fits mud-rock line better than equation (4.4), the latter equation being derived from the deep portion. Thus samples from the shallow portion (above 1000m) of the 04-16 well fit mud-rock line better than samples from the deeper portion.

Figure 4.10 cross-plots  $V_P$  versus  $V_S$  for the 08-08 well. The samples above the Mississippian formation, with the exception of samples with very high P-velocity and those within coal layers, are plotted in the figure. On the 08-08 well, there is hydrocarbon indication on the Glauconitic channel zone from 1552.5m to 1595m. The  $V_P/V_S$  ratio is low over this portion. In Figure 4.10, the samples with low  $V_P/V_S$  on the Glauconitic channel zone are circled and separated from other samples on the  $V_P$ - $V_S$  cross-plot. The trend-line for all selected samples is plotted in this figure, and its equation is

$$V_{P_{08-08}} = 0.95V_{S_{08-08}} + 1915. \quad (4.5)$$

This equation has smaller slope and higher intercept than Castagna's mud-rock line, drawn in Figure 4.10. Due to the samples on the channel zone, equation (4.5) does not reflect the trend of the samples that fall outside the Glauconitic channel zone.

Figure 4.11 shows the  $V_P$ - $V_S$  cross plot and the fitted trend line for the 09-17 well. The samples show a linear trend in the figure. The equation for the trend is

$$V_{P_{09-17}} = 1.74V_{S_{09-17}} + 272. \quad (4.6)$$

Equation (4.6) has a bigger slope than Castagna's mud-rock line equation, and has a much smaller intercept. It can be seen that the Castagna's mud-rock line is not as good as equation (4.6) at indicating the trend of the selected samples in Figure 4.11.

Figure 4.12 shows the  $V_P$ - $V_S$  relationship for the 12-16 well. The statistical relationship is

$$V_{P_{12-16}} = 0.97V_{S_{12-16}} + 1915. \quad (4.7)$$

In Figure 4.12, the samples show a linear trend between  $V_P$  and  $V_S$ . The slope of equation (4.7) is smaller than the slope of mud-rock line and the intercept of equation (4.7) is bigger than that of mud-rock line equation, which has also been drawn in this figure. It is clear that most of the selected samples fall above the mud-rock line.

All  $V_P$ - $V_S$  samples from the four wells are cross-plotted on Figure 4.13. The linear relationship is

$$V_{P_{all}} = 1.26V_{S_{all}} + 1282. \quad (4.8)$$

Compared with equations (4.4) to (4.7), the slope and the intercept of equation (4.8) are closer to the slope and the intercept of mud-rock line equation. This suggests that the population for statistical analysis in the 08-08, 09-17, and 12-16 wells is too small, and that a larger population is needed to compare to the mud-rock equation. However, in Figure 4.13, many samples with higher  $V_P$  ( $V_P > 3300\text{m/s}$ ) and  $V_S$  ( $V_S > 1700\text{m/s}$ ) deviate from the mud-rock line.

#### 4.2.3. Summary of the statistical analysis

The statistical relationships between  $V_P$  and  $V_S$ , which have been obtained by linear regression analysis of four wells with dipole sonic logs in Blackfoot are compared with Castagna's mud-rock equation. The 04-16 well shows good linear relationships between  $V_P$  and  $V_S$ . Samples on the reservoir channel zone on the 08-08 well indicate a

large deviation from the statistical trend. Wells, 08-08, 09-17, and 12-16, were edited to eliminate abnormal portions and all three show different fitted trends from each other and from the 04-16 well. These differences may reflect the subsurface lithology changes and poorly sampled populations. The available log portion lengths and the data quality may also affect the fitted trends and cause statistical trend differences. To obtain a reliable relationship between  $V_P$  and  $V_S$ , more careful interpretation of the well logs is required, alongside the examination of other wells where longer dipole sonics exist. All of the derived trend lines for each well exhibit differences from Castagna's mud-rock line equation. The large population analysis of the 04-16 well suggests that the samples with lower velocity fit Castagna's mud-rock line better than the samples with higher velocity, which deviate from mud-rock line.

The different lithology may have different mud-rock lines, and it seems, therefore, more reasonable to fit different lithology separately. In Blackfoot, the lithology above Mississippian formation is mostly clastic and encourages the fitting of shale and sand rocks separately. In Figure 4.14,  $P$  and  $S$  velocities are cross-plotted for the log portions above Mississippian from well 04-16. The gamma ray value for each sample is shown as different colors indexed as the color bar. Given that a lower gamma value indicates a more sandy sample and higher value indicates more shaly, it may be conclude that the sandy and shaly samples override together and that there is no obvious different mud-rock trends for higher or lower gamma values. Thus, it seems unnecessary to differentiate between them. The mud-rock line in Figure 4.9 is used in the AVO extraction.

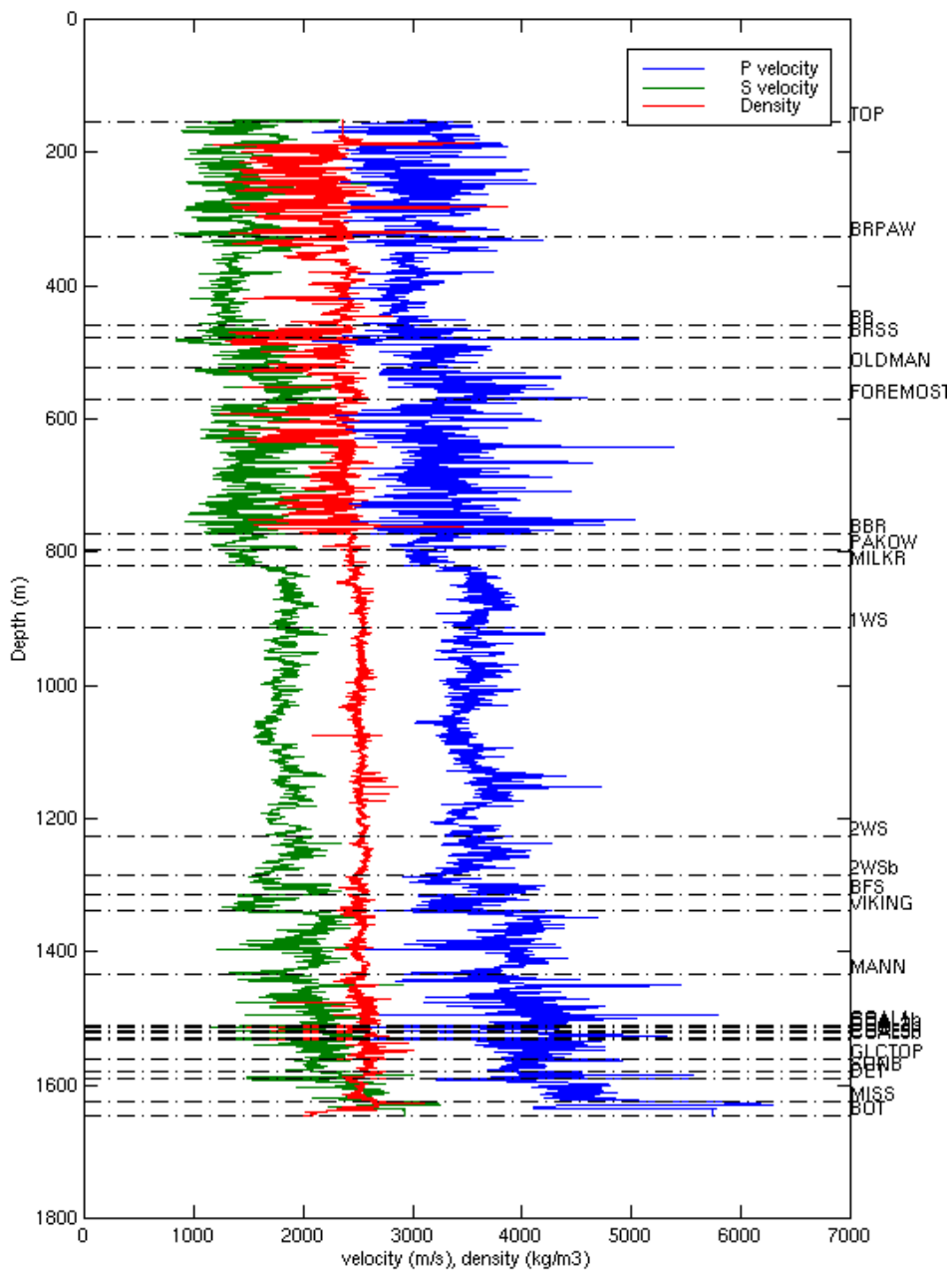


Figure 4.3. Log curves of well 04-16 and formation tops.

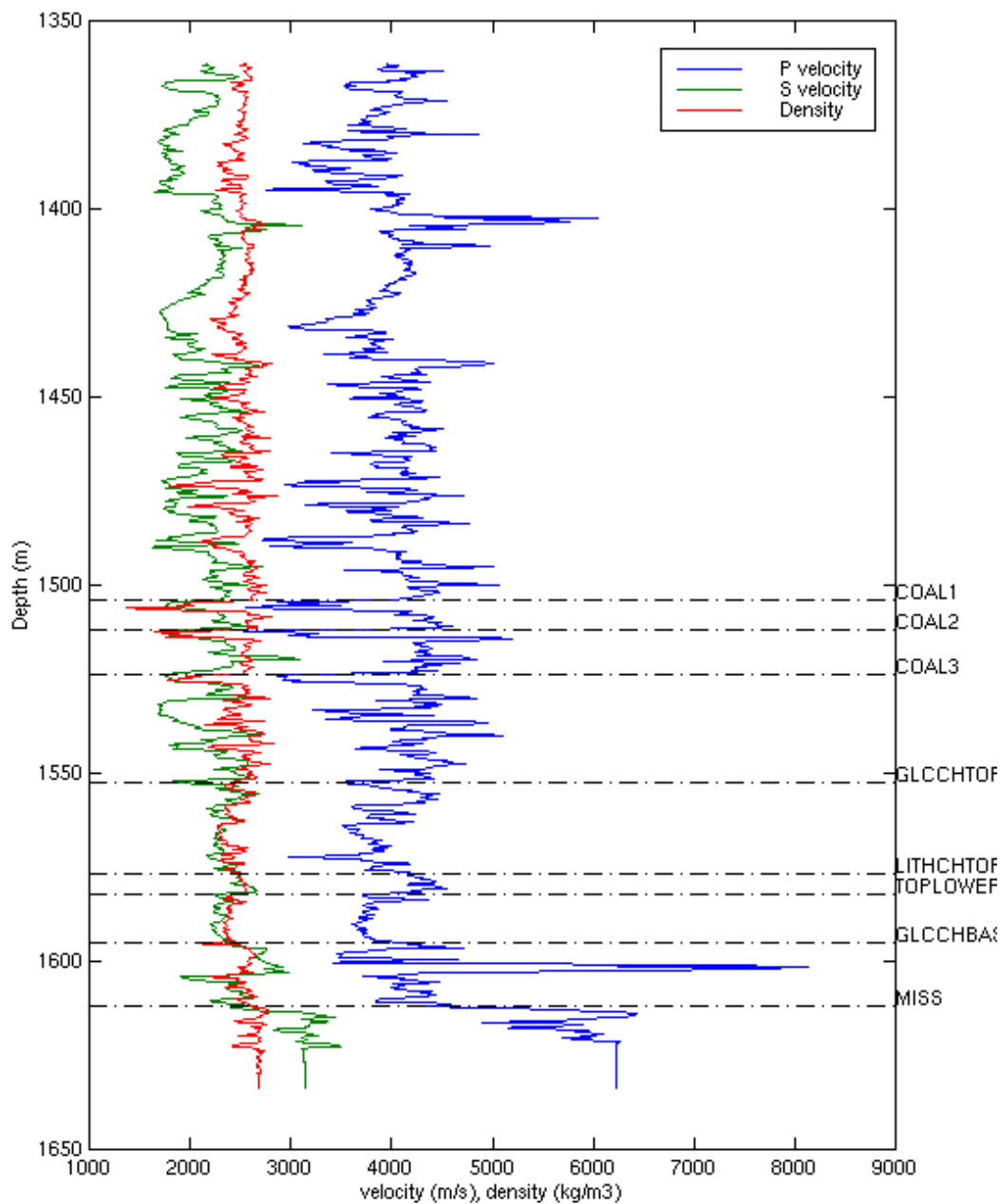


Figure 4.4. Log curves of well 08-08 and the formation tops.

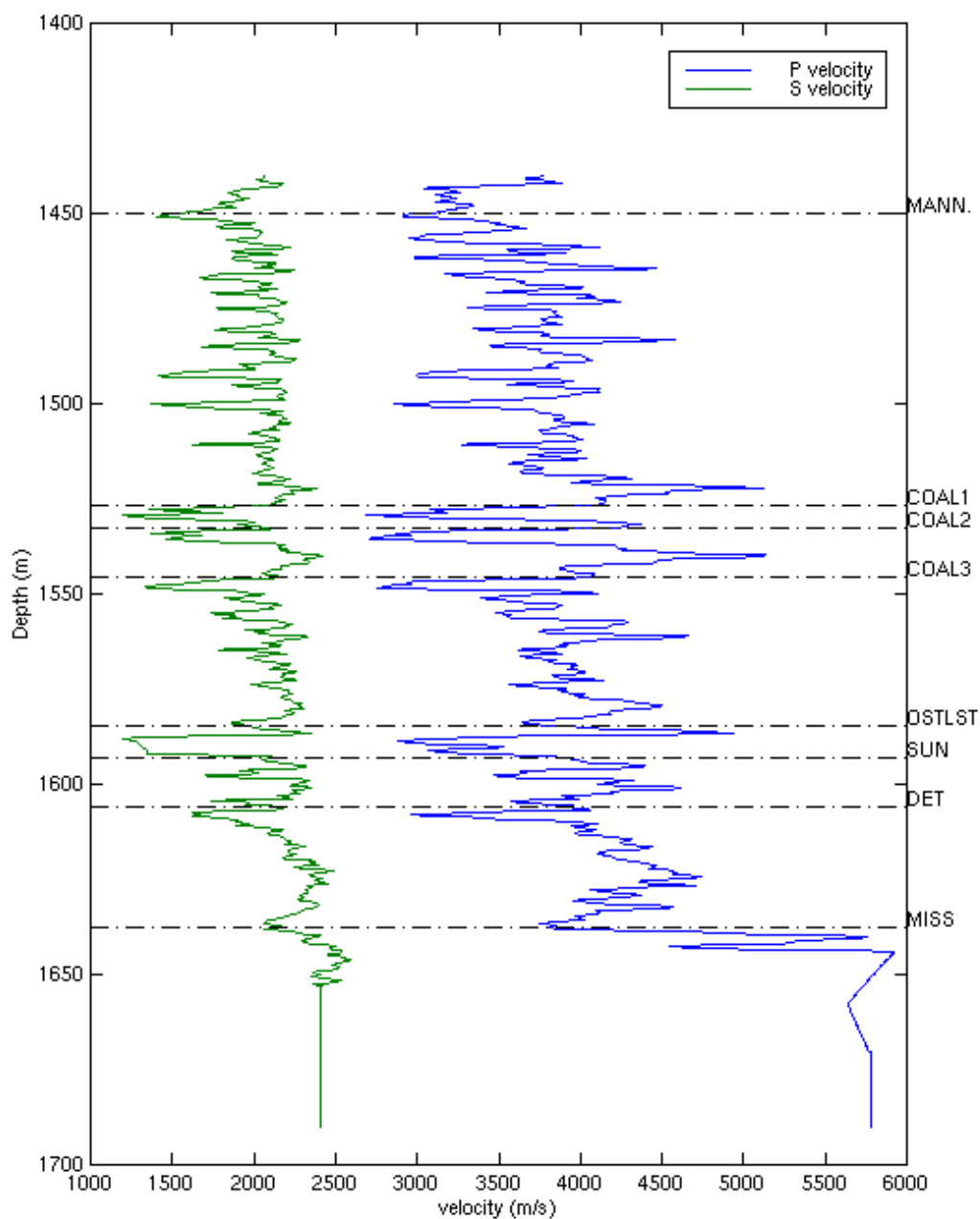


Figure 4.5. Log curves of well 09-17 and formation tops.

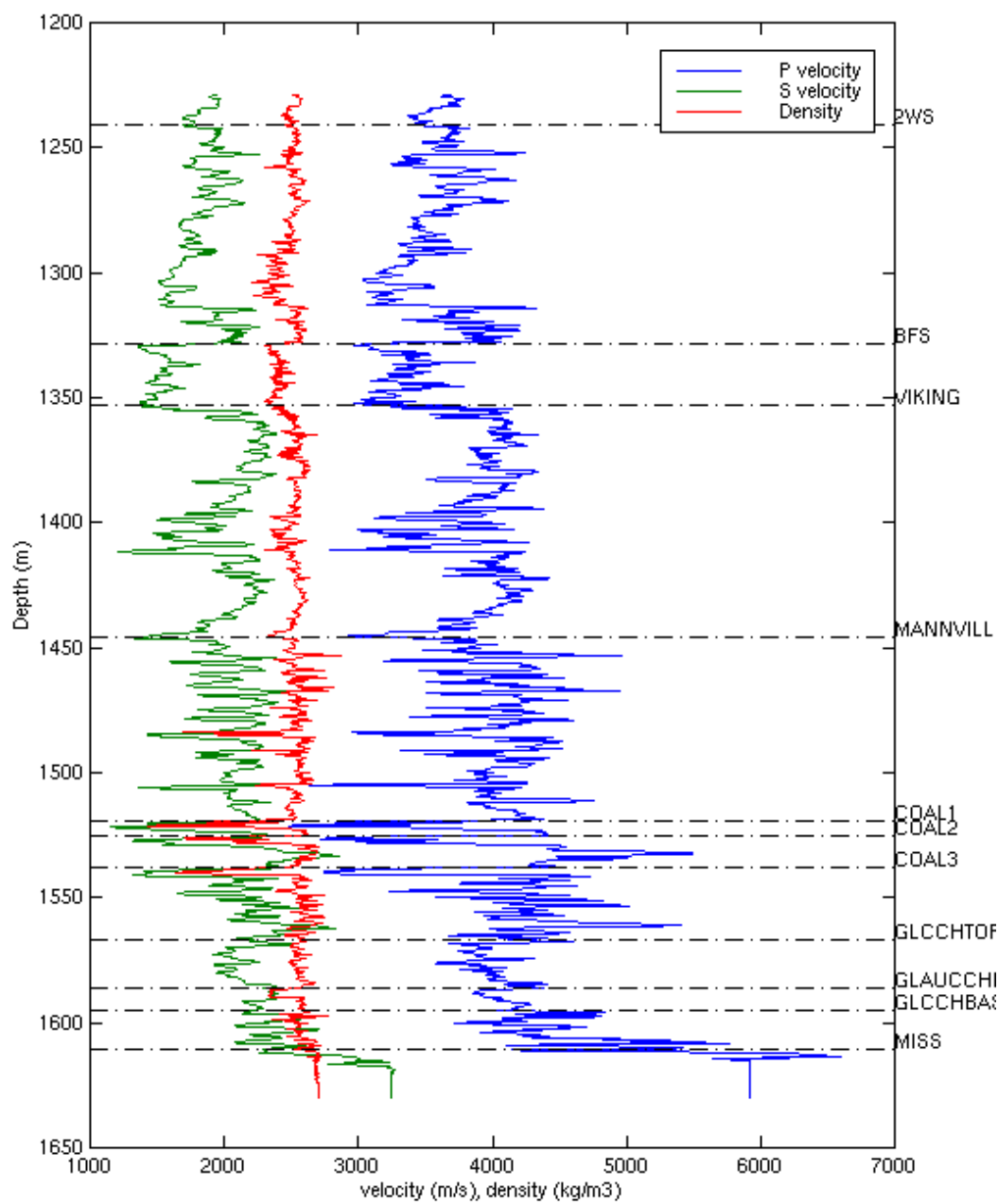
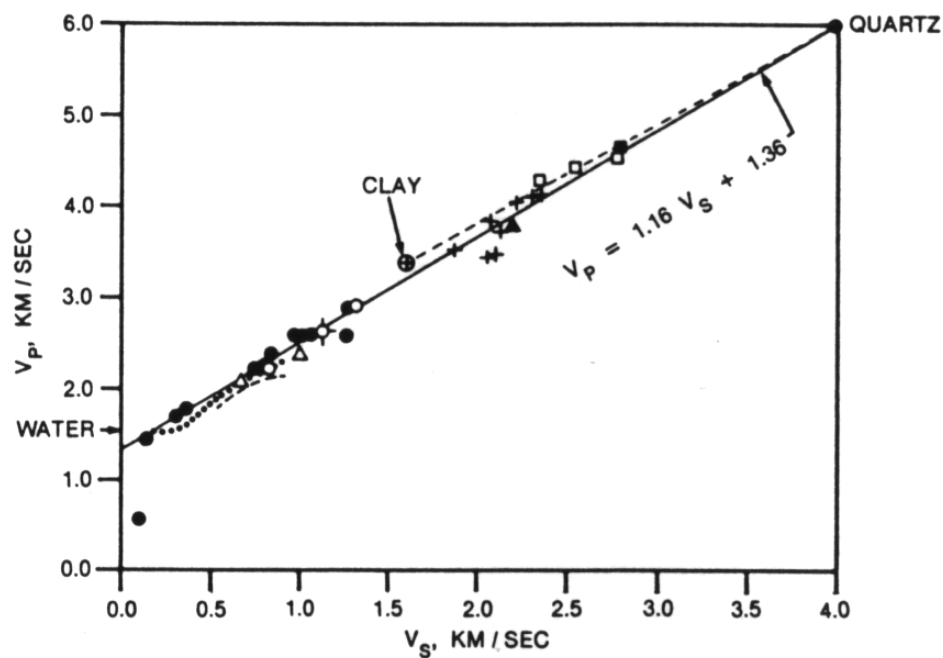


Figure 4.6. Log curves of well 12-16 and formation tops.



- KOERPERICH, 1979, SILTSTONE, SONIC LOG (15 KHz)
- EASTWOOD AND CASTAGNA, 1983, WOLFCAMP SHALE, SONIC LOG (10 KHz)
- ▲ OIL SHALE, SONIC LOG, (25 KHz)
- + LINGLE AND JONES, 1977, DEVONIAN SHALE, SONIC LOG
- ◇ HAMILTON, 1979, PIERRE SHALE
- HAMILTON, 1979, GRAYSON SHALE
- ⊗ HAMILTON, 1979, JAPANESE SHALE
- LASH, 1980, GULF COAST SEDIMENTS, VERTICAL SEISMIC PROFILE
- △ SHALE, SONIC LOG, INVERTED STONELEY WAVE VELOCITIES, (1 KHz)
- ..... HAMILTON, 1979, MUDSTONES
- EBENIRO, 1981, GULF COAST SEDIMENTS, SURFACE WAVE INVERSION
- ⊕ TOSAYA'S "CLAY" POINT (EXTRAPOLATION FROM LABORATORY DATA)

Figure 4.7. Compressional and shear wave velocities for mud-rocks from in-situ sonic and field seismic measurements (Castagna et. al., 1985).

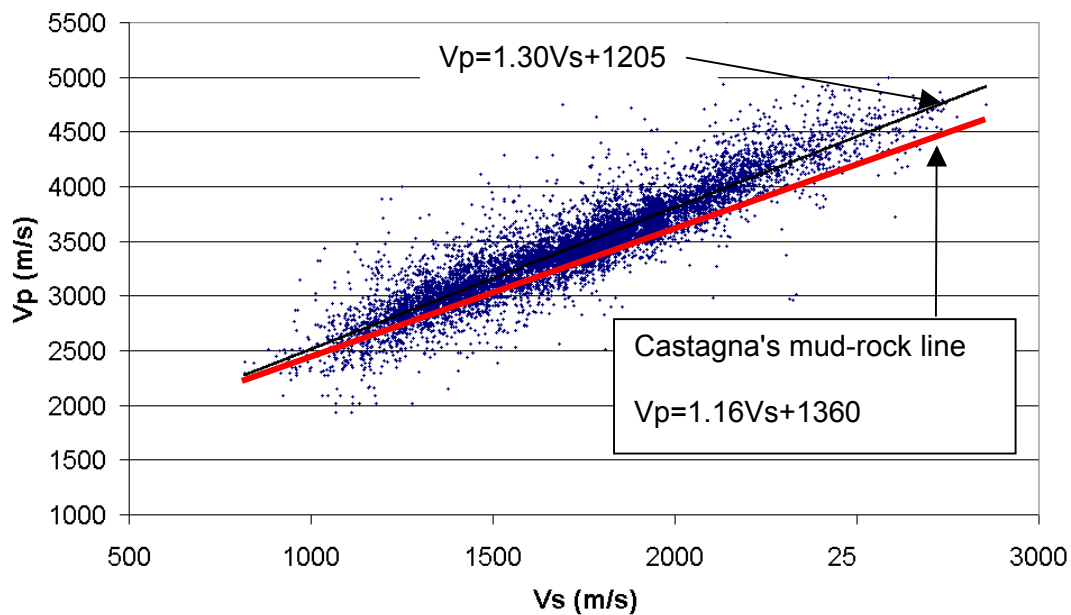


Figure 4.8. Cross-plot of  $V_p$  and  $V_s$  of well 04-16 (all data above Mississippian formation).

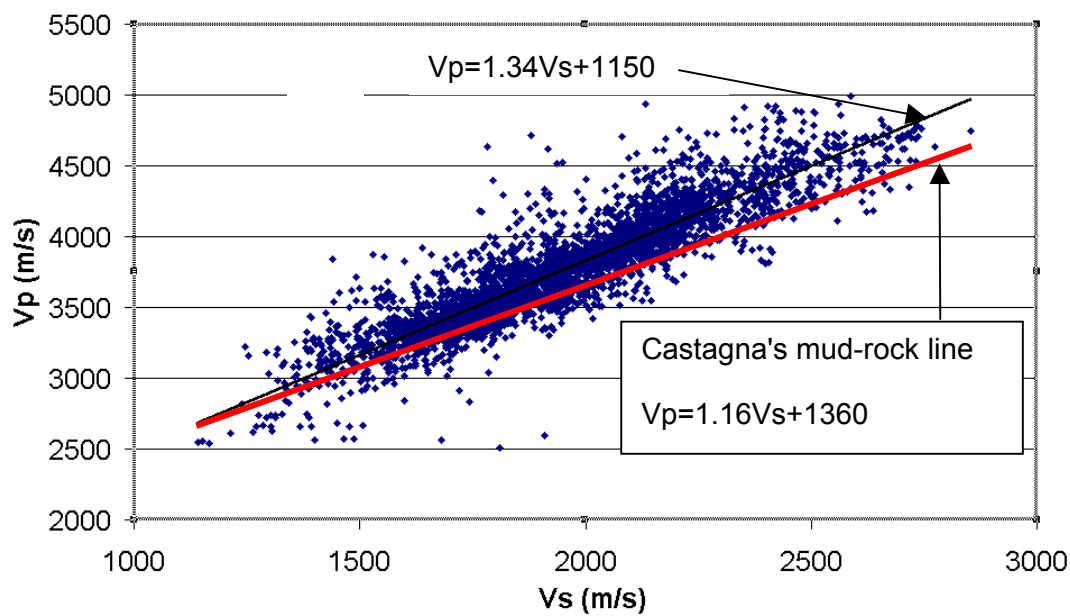


Figure 4.9. Cross-plot of  $V_p$  and  $V_s$  of well 04-16 (portion below 1000 meters and above Mississippian formation).

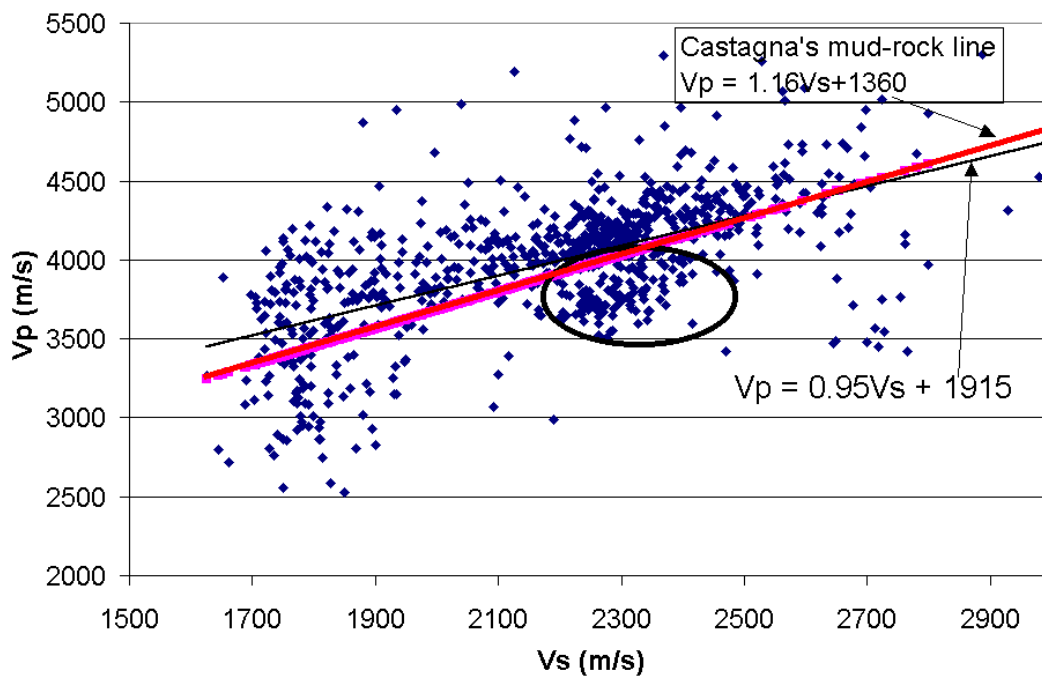


Figure 4.10. Cross-plot of  $V_p$  and  $V_s$  of well 08-08 (portion below 1000 meters and above Mississippian formation).

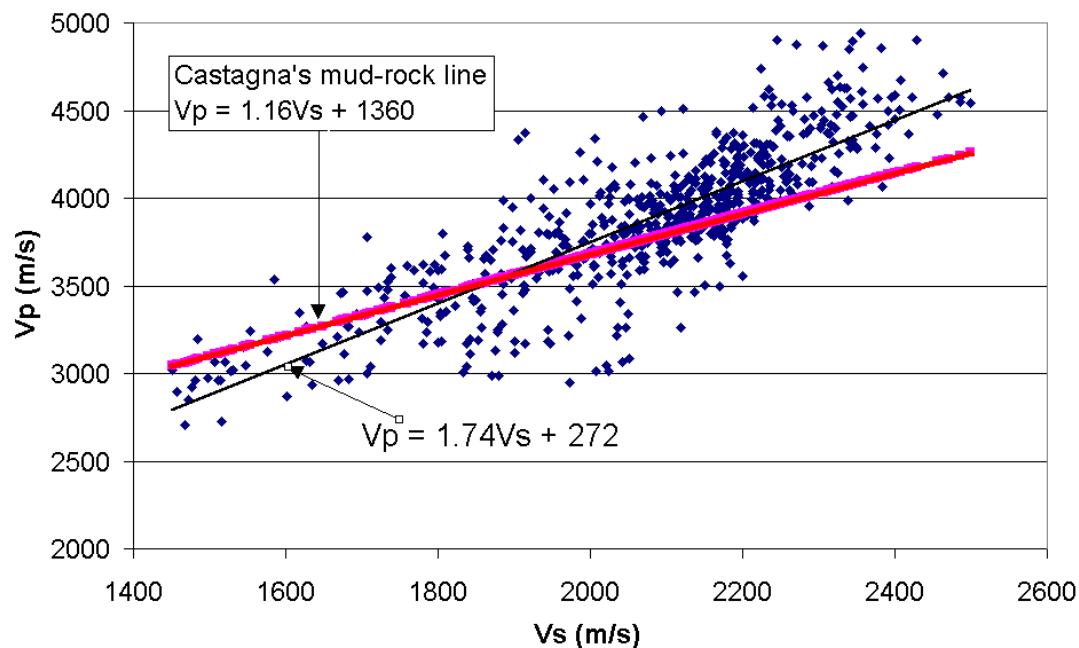


Figure 4.11. Cross-plot of  $V_p$  and  $V_s$  of well 09-17 (above Mississippian formation).

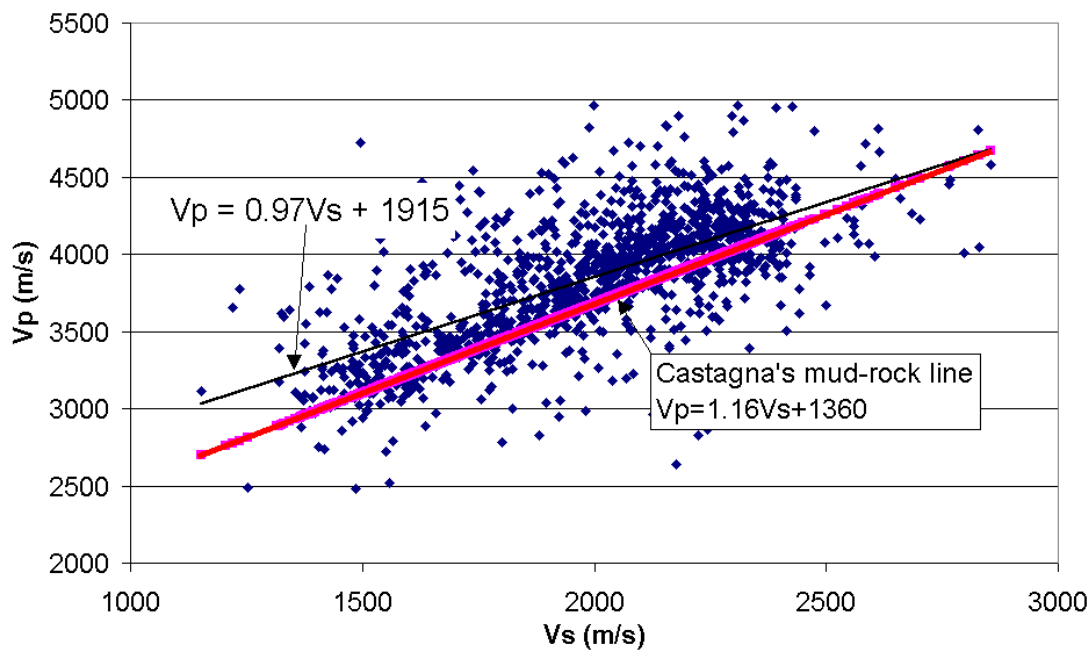


Figure 4.12. Cross-plot of  $V_p$  and  $V_s$  of well 12-16 (portion above Mississippian formation).

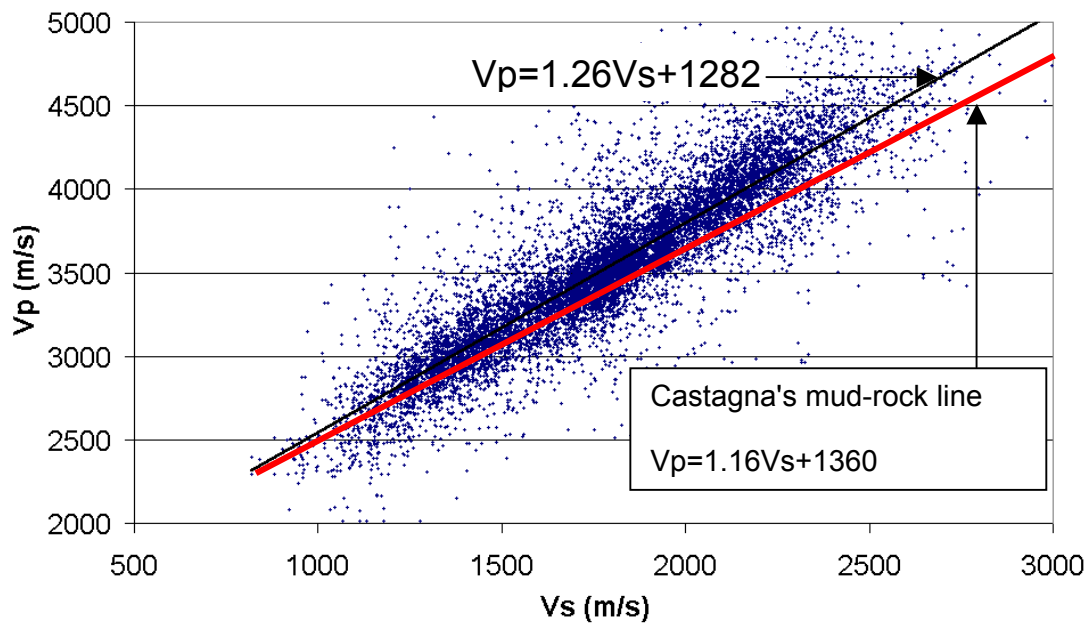


Figure 4.13. Cross-plot of  $V_p$  and  $V_s$  of four wells (portion above Mississippian formation).

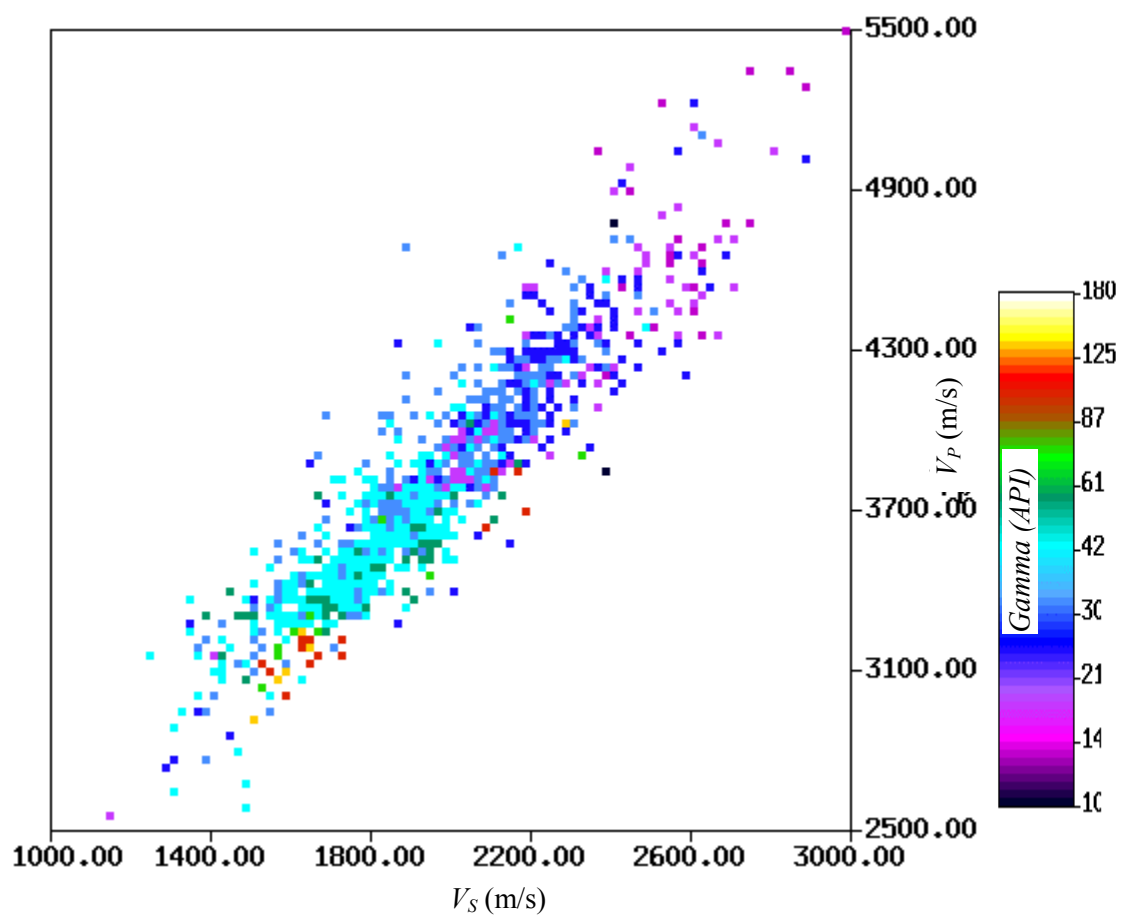


Figure 4.14. Cross-plot of  $V_p$  and  $V_s$  of four wells (portion above Mississippian formation).

### 4.3. EXTRACTION OF LAME PARAMETERS FROM BLACKFOOT 10 HZ VERTICAL DATA

#### 4.3.1. Background

The links between Lamé's parameters and seismic data have been noticed by various authors. Parson (1986), e.g., obtained contrasts of three elastic parameters ( $\lambda$ ,  $\mu$ , and  $\rho$ ) by pre-stack inversion. Goodway et al (1997) obtained the  $V_p$  and  $V_s$  from inversion and converted them to the  $\lambda/\mu$  to detect the reservoirs. Non-uniqueness, however, is always a problem in the seismic inversion, in that background velocity error causes a large ratio change or eliminates high frequency contrast. The discerning selection of parameters, background velocity, wavelet estimation, and the application of a priori information remain important issues which have yet to be resolved. Furthermore, Aki-Richards' approximation of  $P$ - $P$  reflection coefficient indicates that the reflection depends on the rock property contrasts instead of on the absolute value, although the absolute values may be obtained by directly integrating the difference extracted from seismic.

In the following subsections, methods are provided to extract the difference of Lamé's parameters directly from seismic data. The extracted contrasts may be used to detect anomalies before the absolute value is obtained. The extraction provides band-limited information which may be inverted by recursive inversion and other inversion schemes. In the extraction,  $P$ - $P$  reflection coefficient is expressed in the equations with the elastic parameters ( $\lambda$  and  $\mu$ , or  $\kappa$  and  $\mu$ ) and these parameters are directly extracted without using  $S$  velocity models.

#### 4.3.2 Equations in Lamé's parameter extraction

Aki-Richards' reflection coefficient formula for  $P$ - $P$  reflection can be rewritten as the combination of contrasts of incompressibility ( $\lambda$ ), shear modulus ( $\mu$ ), and density ( $\rho$ ) (Parson 1986, Goodway et al. 1997):

$$R_{PP} = \frac{1}{4}(1 + \tan^2 \theta) \frac{\Delta\lambda + 2\Delta\mu}{\lambda + 2\mu} - 2 \left( \frac{V_S}{V_P} \right)^2 \sin^2 \theta \frac{\Delta\mu}{\mu} + \frac{1}{4}(1 - \tan^2 \theta) \frac{\Delta\rho}{\rho} \quad (4.9)$$

Goodway et al. (1997) thought that this equation was impractical for AVO analysis and modified it as the impedance contrasts as equation (4.10). The third term in equation (4.10) can be cancelled using the approximations of  $V_p/V_s \sim 2$  and  $\tan i \sim \sin i$ . After inverting the seismic data to impedance of  $P$  and  $S$  waves, from which  $\lambda/\mu$ ,  $\mu/\rho$ , and ratio of  $\lambda/\mu$  may be calculated. This scheme, which was used by Goodway et al (1997), contains advantages of fewer unknowns and more robustness in the AVO analysis. However, the low frequency information of impedance from inversions is usually inaccurate, which influences ratio of  $\lambda/\mu$ , and, therefore, the detectability of anomalies.

$$R_{PP} = (1 + \tan^2 \theta) \frac{\Delta I_P}{I_P} - 8 \left( \frac{V_S}{V_P} \right)^2 \sin^2 \theta \frac{\Delta I_S}{I_S} + \left[ \frac{1}{2} \tan^2 \theta - 2 \left( \frac{V_S}{V_P} \right)^2 \sin^2 \theta \right] \frac{\Delta \rho}{\rho}. \quad (4.10)$$

In comparison to moduli and velocities, the variation of density is usually the smallest in the subsurface. The relative changes in density are much smaller than moduli changes, which may be seen on well logs. In Figure 3.7, various relative changes of rock parameters of well 08-08 blocked model in the Blackfoot survey are plotted. The small relative change of density compared with several forms of relative changes of  $\lambda$  and  $\mu$  may be noted. Actually the relative changes of  $\lambda$  and  $\mu$  magnify the changes of  $V_p$  and  $V_s$ . There is a great change of  $\Delta\mu/\mu$  at the oil-bearing layer (1580 meter).

Substituting relationship  $(V_s/V_p)^2 = \mu/(\lambda+2\mu)$  into equation (4.9), we have an equation without  $(V_s/V_p)^2$  as:

$$R_{PP} = \frac{1}{4} (1 + \tan^2 \theta) \frac{\Delta\lambda + 2\Delta\mu}{\lambda + 2\mu} - \sin^2 \theta \frac{2\Delta\mu}{\lambda + 2\mu} + \frac{1}{4} (1 - \tan^2 \theta) \frac{\Delta\rho}{\rho}. \quad (4.11)$$

Equation (4.11) can also be rewritten as the combination of contrasts of bulk and shear moduli and density as follows:

$$R_{PP} = \frac{1}{4} (1 + \tan^2 \theta) \frac{\Delta\kappa + \frac{4}{3}\Delta\mu}{\kappa + \frac{4}{3}\mu} - \sin^2 \theta \frac{2\Delta\mu}{\kappa + \frac{4}{3}\mu} + \frac{1}{4} (1 - \tan^2 \theta) \frac{\Delta\rho}{\rho}. \quad (4.12)$$

To make the AVO analysis more robust, the last term may be neglected as the density changes are small.

$$R_{PP} \approx \frac{1}{4}(1 + \tan^2 \theta) \frac{\Delta\lambda + 2\Delta\mu}{\lambda + 2\mu} - \sin^2 \theta \frac{2\Delta\mu}{\lambda + 2\mu} \quad (4.13)$$

Another way to make equation (4.12) a two-term expression is to incorporate the third term into the first term. Gardner's relationship fits to a very wide range of velocities and densities. Gardner's relationship between density and  $P$  wave velocity is

$$\rho = aV_p^b \quad (b=0.25). \quad (4.14)$$

The relationship between moduli, density and  $P$  wave velocity is

$$V_p = \sqrt{\frac{\lambda + 2\mu}{\rho}}. \quad (4.15)$$

From equations (4.14) and (4.15), an approximation of equation (4.12) is obtained as:

$$R_{PP} \approx \frac{1}{4} \left( \frac{10}{9} + \frac{8}{9} \tan^2 \theta \right) \frac{\Delta\lambda + 2\Delta\mu}{\lambda + 2\mu} - \sin^2 \theta \frac{2\Delta\mu}{\lambda + 2\mu} \quad (4.16)$$

or

$$R_{PP} \approx \frac{1}{4} \left( \frac{10}{9} + \frac{8}{9} \tan^2 \theta \right) \frac{\Delta\lambda}{\lambda + 2\mu} - \frac{1}{2} \left( \frac{10}{9} + \frac{8}{9} \tan^2 \theta - 4 \sin^2 \theta \right) \frac{\Delta\mu}{\lambda + 2\mu} \quad (4.17)$$

### 4.3.3 Lamé's parameter extraction from vertical component

Pre-stack seismic data were acquired from a 10 Hz Blackfoot seismic data set, with preliminary processing and amplitude-preserving processing being applied.

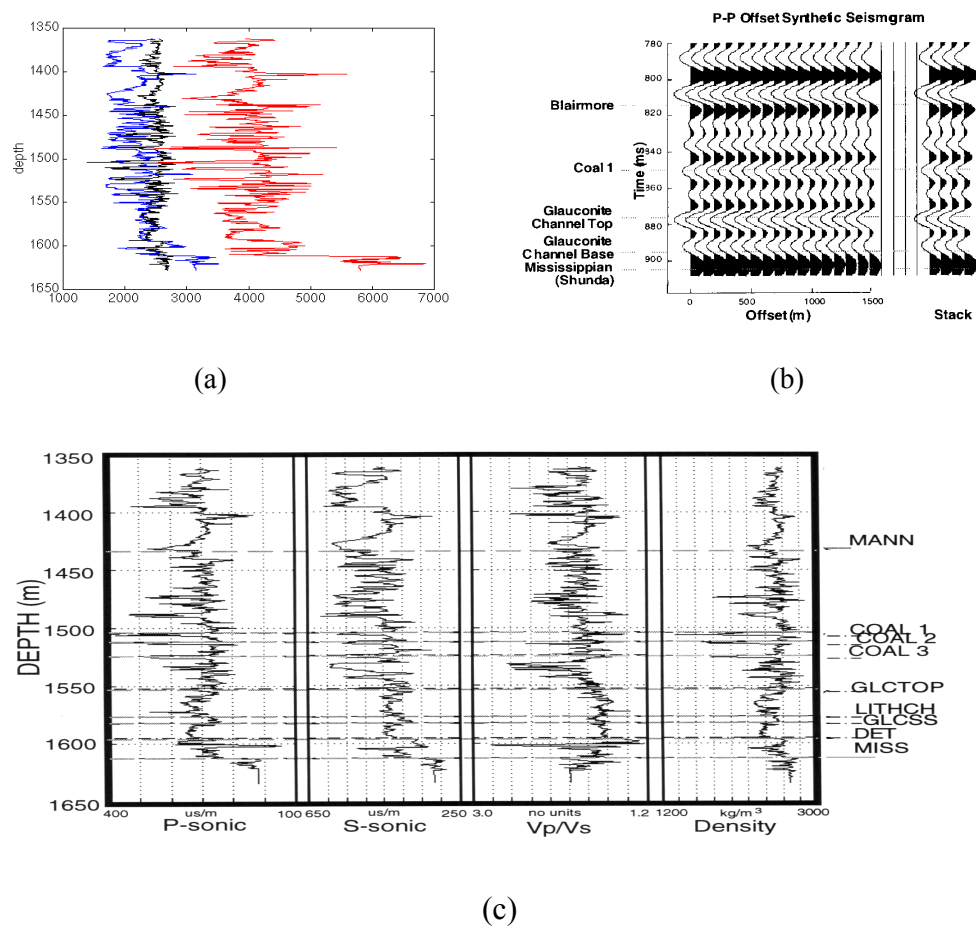


Figure 4.15. Well 0808 and synthetic gather from the well (Margrave et al, 1995, Potter et al, 1996).

Figure 4.15 shows the well logs of well 0808 and the synthetic gather. The Glaucoritic channel formation is also shown on the well logs. From the  $P$ -wave velocity and density contrasts, the channel sand has low  $P$  impedance. However the impedance changes are minimal, and the AVO anomaly on the synthetic gather lacks significance.

#### 4.3.3.1. $V_p/V_s$ ratio reflectivity

Using equation (4.13), the relative contrasts,  $\frac{\Delta(\lambda + 2\mu)}{\lambda + 2\mu}$  and  $\frac{\Delta\mu}{\lambda + 2\mu}$  are obtained

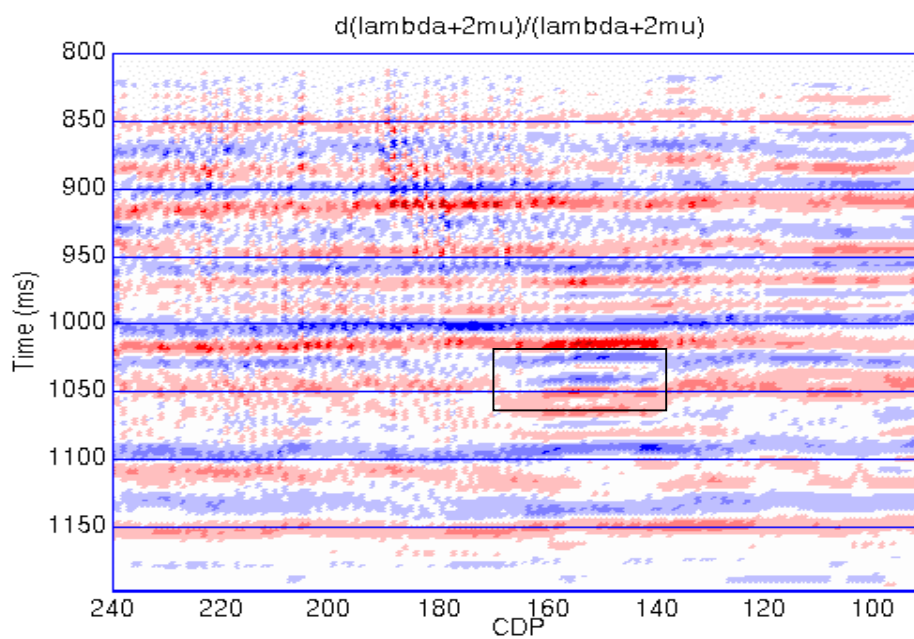
by linear regression. By combining these contrasts, the contrasts of  $\frac{\Delta\lambda}{\lambda + 2\mu}$ ,  $\frac{\Delta(\kappa - \mu)}{\lambda + 2\mu}$

and  $\frac{\Delta\gamma}{\gamma}$  are also derived, where  $\gamma$  is the  $V_p/V_s$  ratio. The relationship between these contrasts is

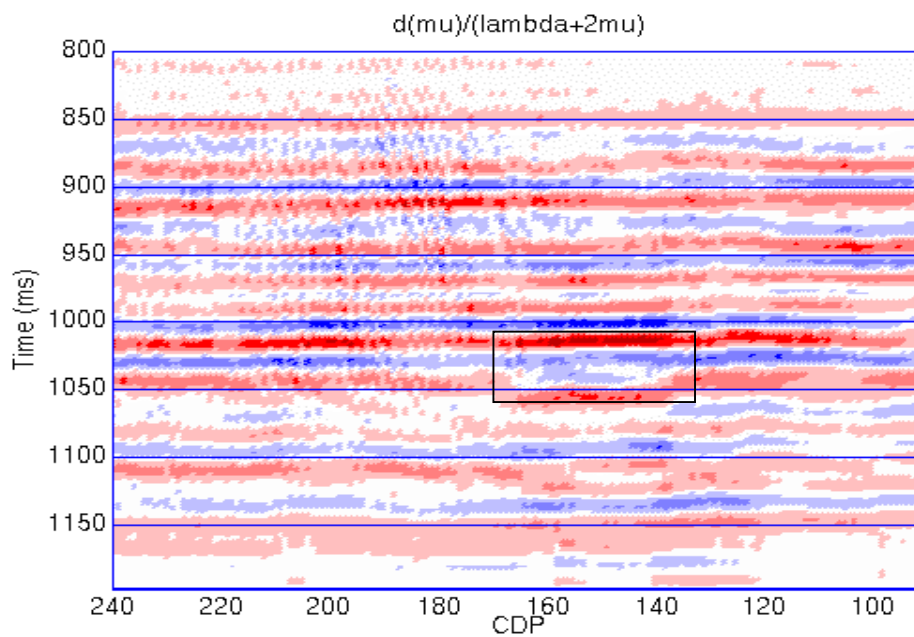
$$\frac{\Delta\gamma}{\gamma} = \frac{1}{2} \left( \frac{\Delta\lambda}{\lambda+2\mu} - \frac{(\gamma^2-2)\Delta\mu}{\lambda+2\mu} \right) \approx \frac{1}{2} \left( \frac{\Delta\lambda}{\lambda+2\mu} - \frac{2\Delta\mu}{\lambda+2\mu} \right). \quad (4.18)$$

#### 4.3.3.2. Extraction results

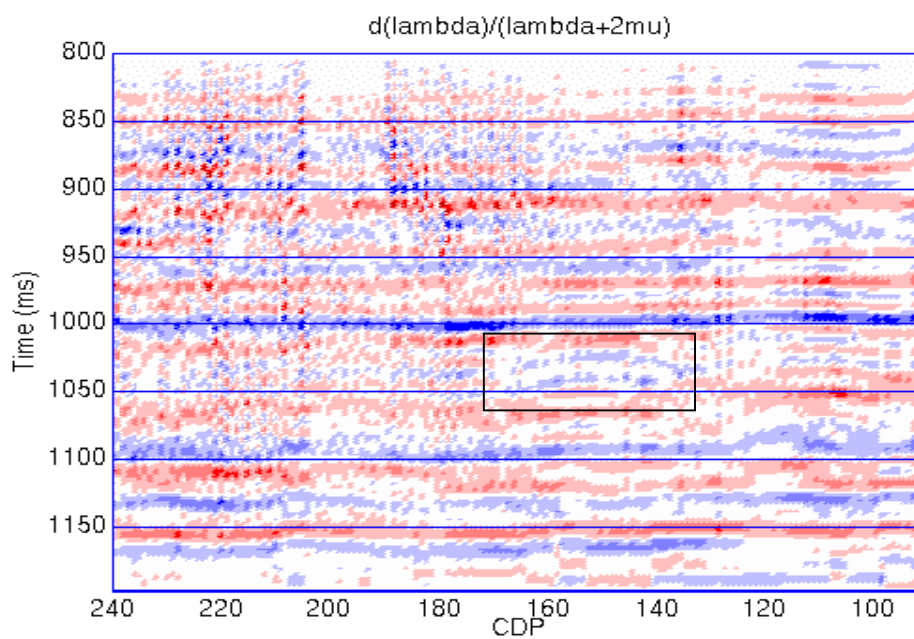
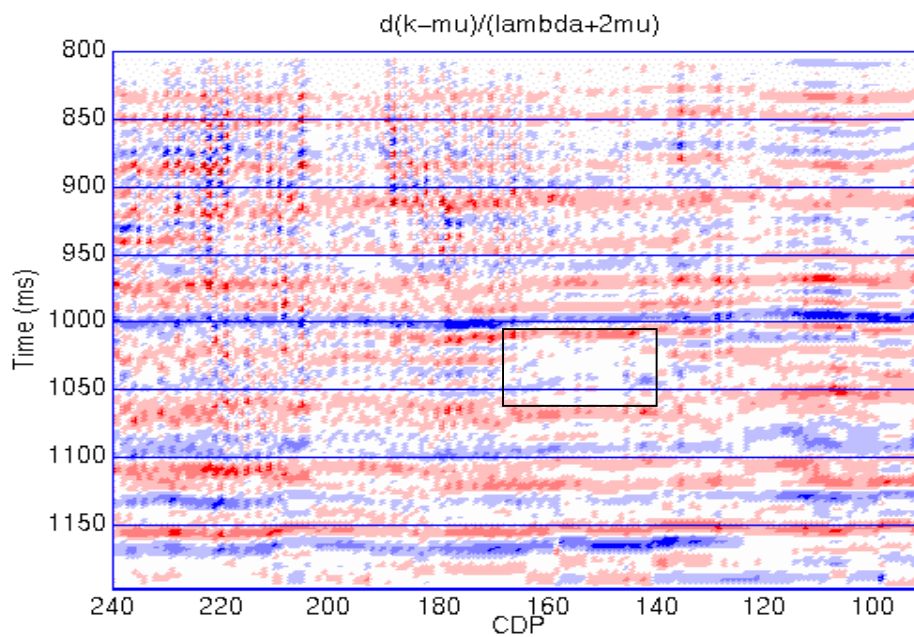
In Figure 4.18 (a) the contrast of  $\Delta(\lambda+2\mu)/(\lambda+2\mu)$  results an anomaly in the box (CDP 130-170, time 1000ms-1100ms), which is the approximated location of the Glauconitic channel. The box shows the zone and the difference from neighborhood. The extracted  $\Delta\mu/(\lambda+2\mu)$  section is displayed in Figure 4.18 (b). In the box in this figure, the Glauconitic channel shape can be seen.. Figure 4.18 (c) is obtained by subtraction of two times Figure 4.18 (b) from Figure 4.18 (a), approximating, thereby,  $\Delta\lambda/(\lambda+2\mu)$ . The anomaly shown in Figure 4.18 (a) is also evident, albeit weaker in Figure 4.18 (c). In Figure 4.18 (d), the  $\Delta(\kappa-\mu)/(\lambda+2\mu)$  is plotted. The channel in this figure has a white infillment, indicating an anomaly. In Figure 4.18 (e), the  $\Delta\gamma/\gamma$  manifests greater changes within the channel than in the neighborhood.

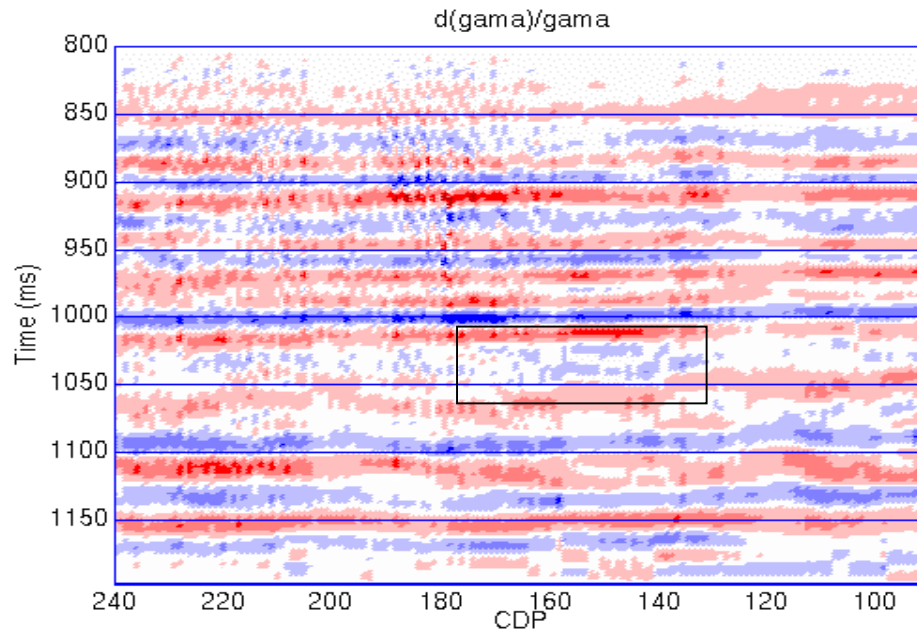


(a) the section of  $\Delta(\lambda+2\mu)/(\lambda+2\mu)$



(b) section of  $\Delta\mu/(\lambda+2\mu)$

(c) the section of  $\Delta\lambda/(\lambda+2\mu)$ (d) the section of  $\Delta(\kappa-\mu)/(\lambda+2\mu)$



(e) the section of  $\Delta\gamma/\gamma$  ( $\gamma$  is the  $V_p/V_s$  ratio).

Figure 4.18. The analysis results of Blackfoot vertical seismic data.

#### 4.3.3.3. Inversion of extracted lame parameters

Lame's parameter extraction sections are relative change of Lame's parameters with limited frequency band similar as seismic data. For the data studied here, the frequency band is 10-15-60-70 Hz. Full band results, at least with low frequency components, can help the interpretation. In the thesis, extracted  $\Delta\lambda/\lambda$  and  $\Delta\mu/\mu$  are inverted to  $\lambda$  and  $\mu$  using band limited inversion algorithms. The low frequency components of  $\lambda$  and  $\mu$  are built from well logs, which are incorporated with the components converted from  $\Delta\lambda/\lambda$  and  $\Delta\mu/\mu$ .

Figure 4.19 shows the inversion results for the extraction sections in Figure 4.18. The recursive integration of the AVO extraction sections in Figure 4.18 is merged with those low frequency components, which have been obtained from well logs.

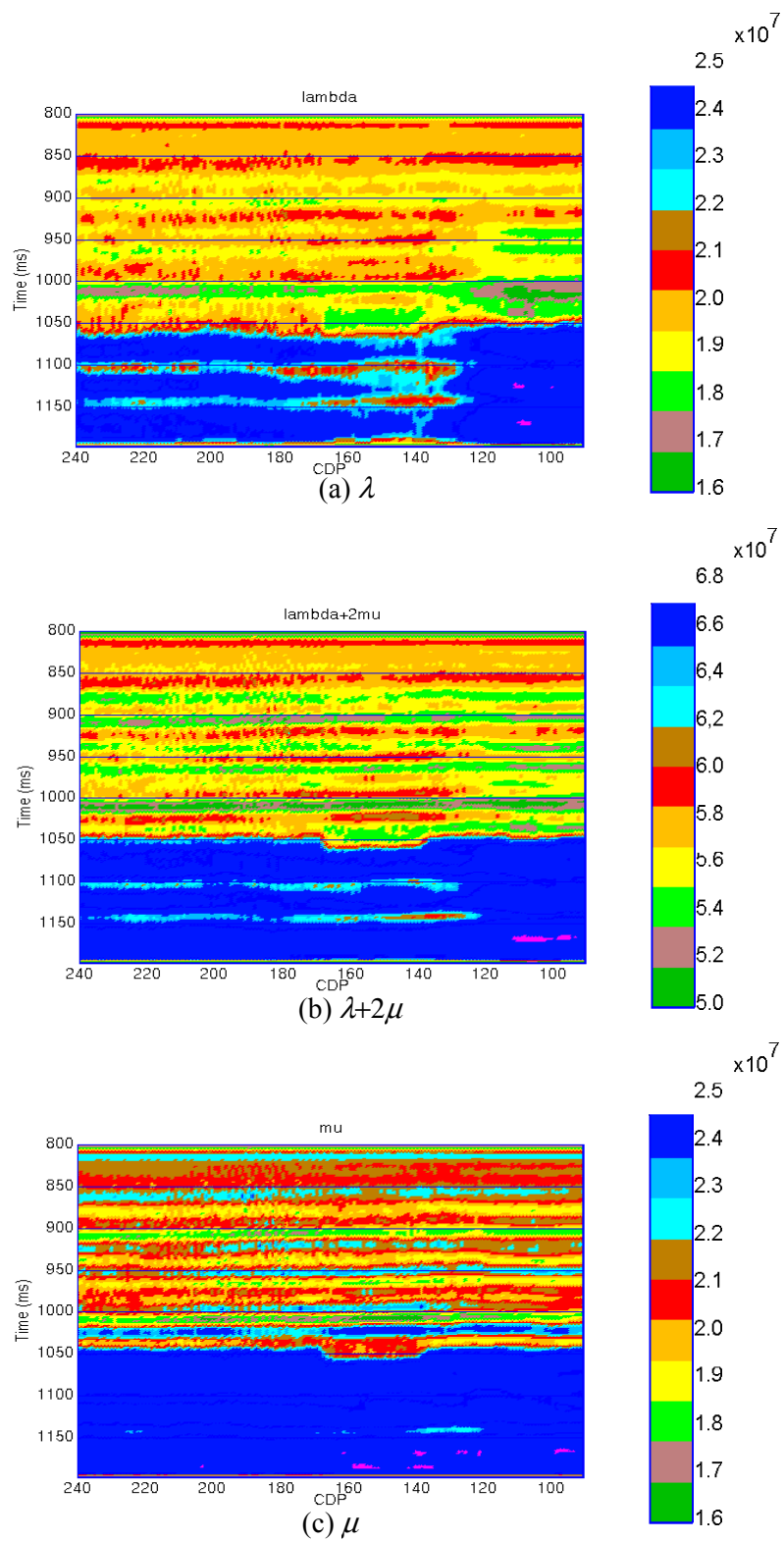


Figure 4.19. The inversion results from Figure 4.18.

#### 4.4. EXTRACTION OF $R_P$ AND $R_S$ AND FLUID FACTOR FROM VERTICAL COMPONENT DATA

The fluid factor method was introduced by Smith and Gidlow (1987) to seek these anomalies that deviate from a certain statistical relationship between  $V_P$  and  $V_S$  (see 4.2.1). Smith and Gidlow (1987) define the fluid factor as

$$\Delta F = \frac{\Delta V_P}{V_P} - 1.16 \frac{V_S}{V_P} \frac{\Delta V_S}{V_S}. \quad (4.19)$$

Derivation of equation (4.19) uses Castagna's mud-rock line that is a statistical relationship between  $V_P$  and  $V_S$  (Castagna, et. al., 1985) and is defined as

$$V_P = 1.16V_S + 1360. \quad (4.20)$$

The  $\frac{\Delta V_P}{V_P}$  and  $\frac{\Delta V_S}{V_S}$  in equation (4.19) can be approximated by  $R_P$  and  $R_S$  in the usual cases because density exhibits much smaller relative changes than  $V_P$  or  $V_S$ . The  $P$  and the  $S$  wave normal incident reflectivities ( $R_P$  and  $R_S$ ) are extracted from CDP gathers after true amplitude processing.

##### 4.4.1. Methodology

The  $R_P$  and  $R_S$  extraction from seismic data is based on Aki-Richards' approximation for  $P$ - $P$  reflection coefficient,  $R_{PP}(\theta)$ , which varies with incident angle,  $\theta$ . Aki-Richards' approximation is reformatted as equation (4.21):

$$R_{PP}(\theta) = \frac{1}{2}(1 + \tan^2 \theta) \frac{\Delta I_p}{I_p} - 4\left(\frac{V_S}{V_P}\right)^2 \sin^2 \theta \frac{\Delta I_s}{I_s} - \left[\frac{1}{2} \tan^2 \theta - 2\left(\frac{V_S}{V_P}\right)^2 \sin^2 \theta\right] \frac{\Delta \rho}{\rho} \quad (4.21)$$

Equation (4.21) is approximated to equation (4.22) with sufficient accuracy in the small incident angle ( $< 40^\circ$ ) cases:

$$R_{PP}(\theta) = (1 + \tan^2 \theta)R_P - 8\left(\frac{V_S}{V_P}\right)^2 (\sin^2 \theta)R_S, \quad (4.22)$$

where  $R_P = \frac{1}{2} \frac{\Delta I_P}{I_P}$  and  $R_S = \frac{1}{2} \frac{\Delta I_S}{I_S}$  are  $P$  and  $S$  wave normal incident reflectivity.

In this thesis, the vertical component seismic data is carefully processed to preserve true amplitude.  $R_P$  and  $R_S$  sections are extracted from CDP gathers using equation (4.22). A mud-rock line is derived from local sonic and shear sonic well logs. The fluid factor in equation (4.19) is modified using the new mud-rock line, before being calculated from the  $R_P$  and  $R_S$  sections.

Figure 4.1 shows the location map of 3C-2D seismic line 950278, the well controls and the incised valley isopach (Miller et. al., 1995). Two wells, 04-16 and 14-09, are used to form velocity models and derive the mud-rock line. The 04-16 well has dipole sonic log, while 14-09 does not have shear sonic log. Figure 4.20 shows the cross-plot of  $V_P$  and  $V_S$  of well 04-16 (portion below 1000 meters and above Mississippian formation). The fitted linear relationships between  $V_P$  and  $V_S$  and Castagna's mud-rock line are plotted in Figure 4.20. The fitted line has the equation (4.23), which has different coefficients from Castagna's mud-rock line in equation (4.19):

$$V_P = 1.340V_S + 1150. \quad (4.23)$$

From equation (4.23), a new fluid factor with a slight difference from equation (4.19), is derived:

$$\Delta F = \frac{\Delta V_P}{V_P} - 1.34 \frac{V_S}{V_P} \frac{\Delta V_S}{V_S}. \quad (4.24)$$

The right hand side curve in Figure 4.20 is the deviation of  $P$  wave velocity from the statistical trend in the essential portion. The deviation of hydrocarbon saturation on the well may not be seen because it is a dry hole. Glauconitic formation shows positive deviations, while the coals above Glauconite show negative deviations. Some shale in the channel has big positive deviations from statistical trends.

From vertical component data,  $P$  wave and  $S$  wave reflectivities may be extracted, and the well log used to fit a relationship between  $P$  and  $S$  wave velocities. This

relationship serves as a guide to calculate spatial anomalies in these  $P$  and  $S$  reflectivities, which have been extracted from vertical component.

#### 4.4.2. Extraction results

For purposes of comparison, the stack section of the vertical component data is plotted in Figure 4.21. The Glauconitic channel locates between CDP 140 and 165 at a time of around 1050ms. The Mississippian formation (with weathered top) is below the channel at a time of 1075ms. Figures 4.22 and 4.23 show the extracted  $R_P$  and  $R_S$  sections. The  $R_P$  section has no significant difference from the stack section, although it has better resolution than the stack section, with the Mississippian top being clearer on the  $R_P$  section. The  $R_S$  section is noisier and less continuous than the  $R_P$  section and the Mississippian top is not as clear. The inside of the channel, however, is more detailed in the  $R_S$  section. By comparing  $R_P$  and  $R_S$  sections, other lithology changes may be confirmed. The fluid factor section as shown in Figure 4.24 has advantages over  $R_P$  or  $R_S$  section in terms of describing the anomaly caused by the incised valley. Figure 4.25 enlarges the time portion around Glauconitic channel zone. In Figures 4.24 and 4.25, the Glauconitic channel anomaly is very strong and detailed.

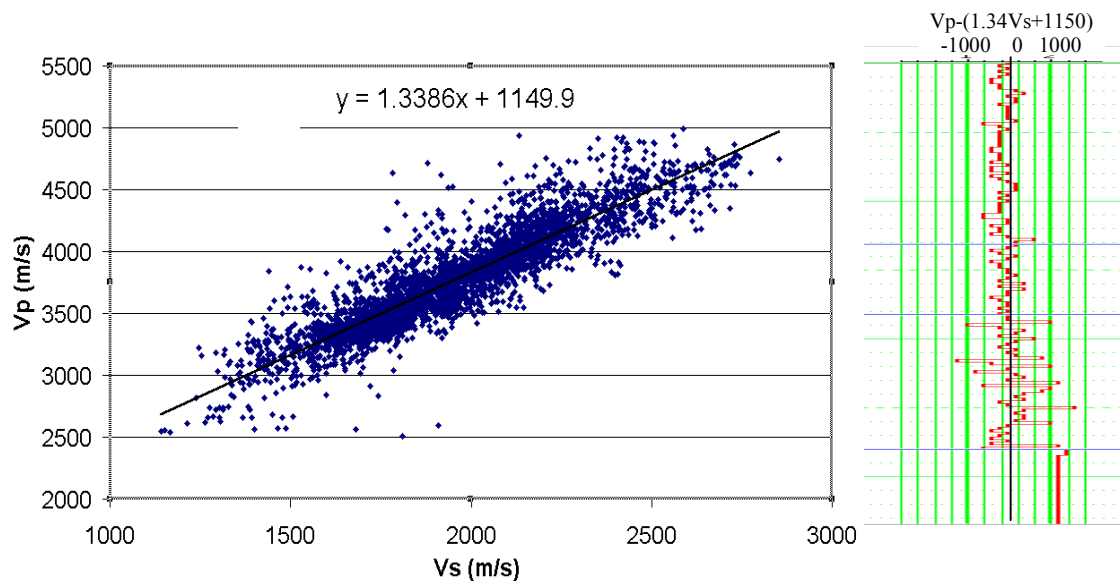


Figure 4.20. Statistical relationship between  $V_p$  and  $V_s$  from 04-16 well and  $V_p$ 's deviations from this statistical relationship.

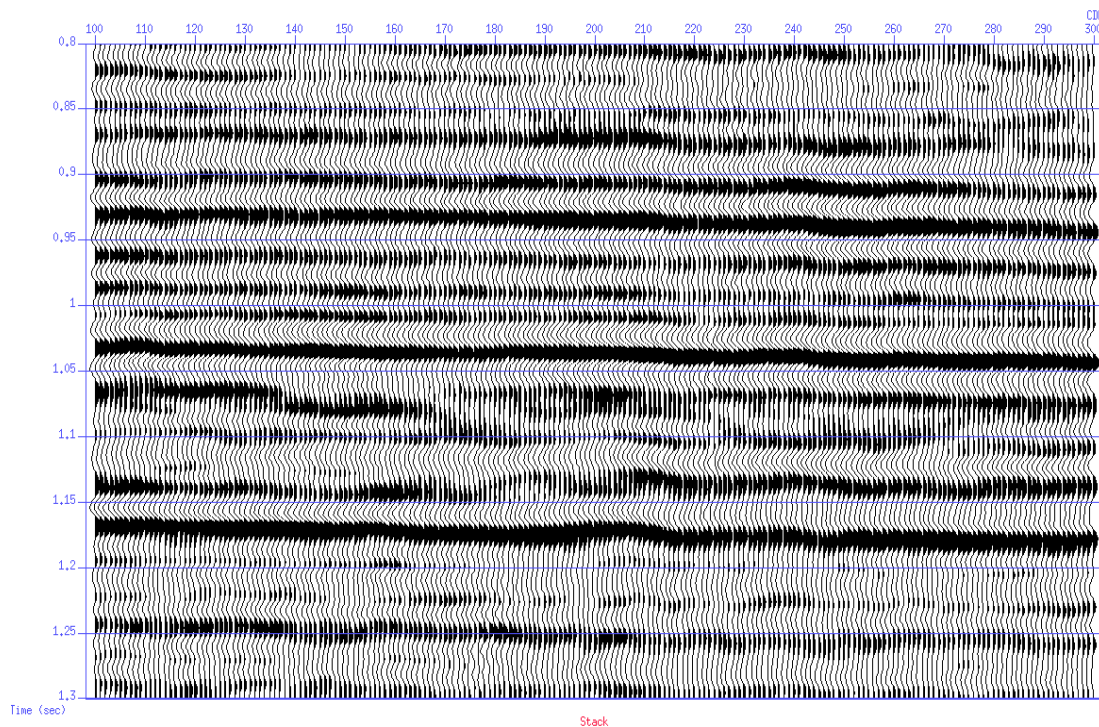


Figure 4.21. Stack section of vertical component of 10Hz data.

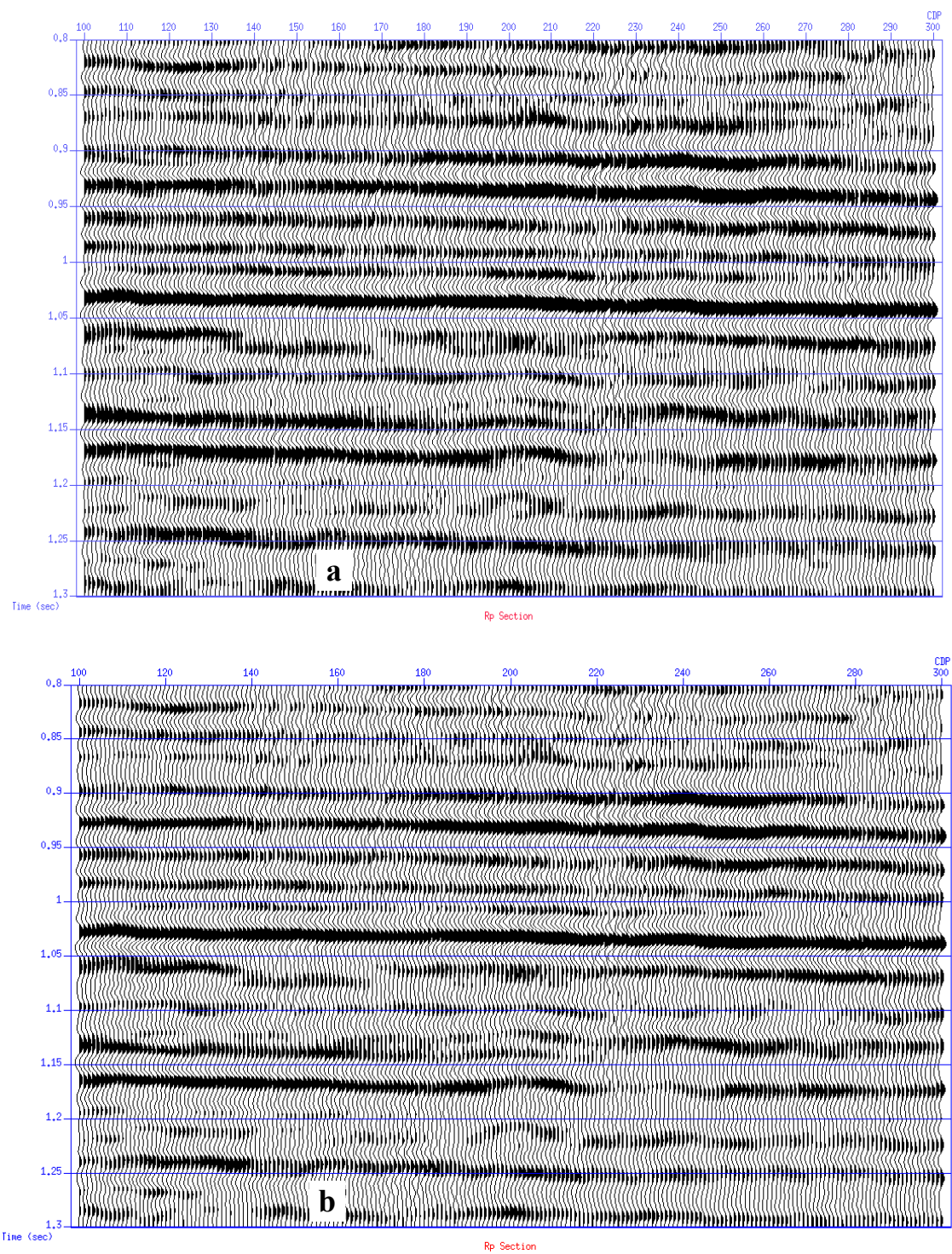


Figure 4.22. Extraction  $P$  wave reflectivity section from vertical component. (b) is 50 degree phase rotation applied on (a).

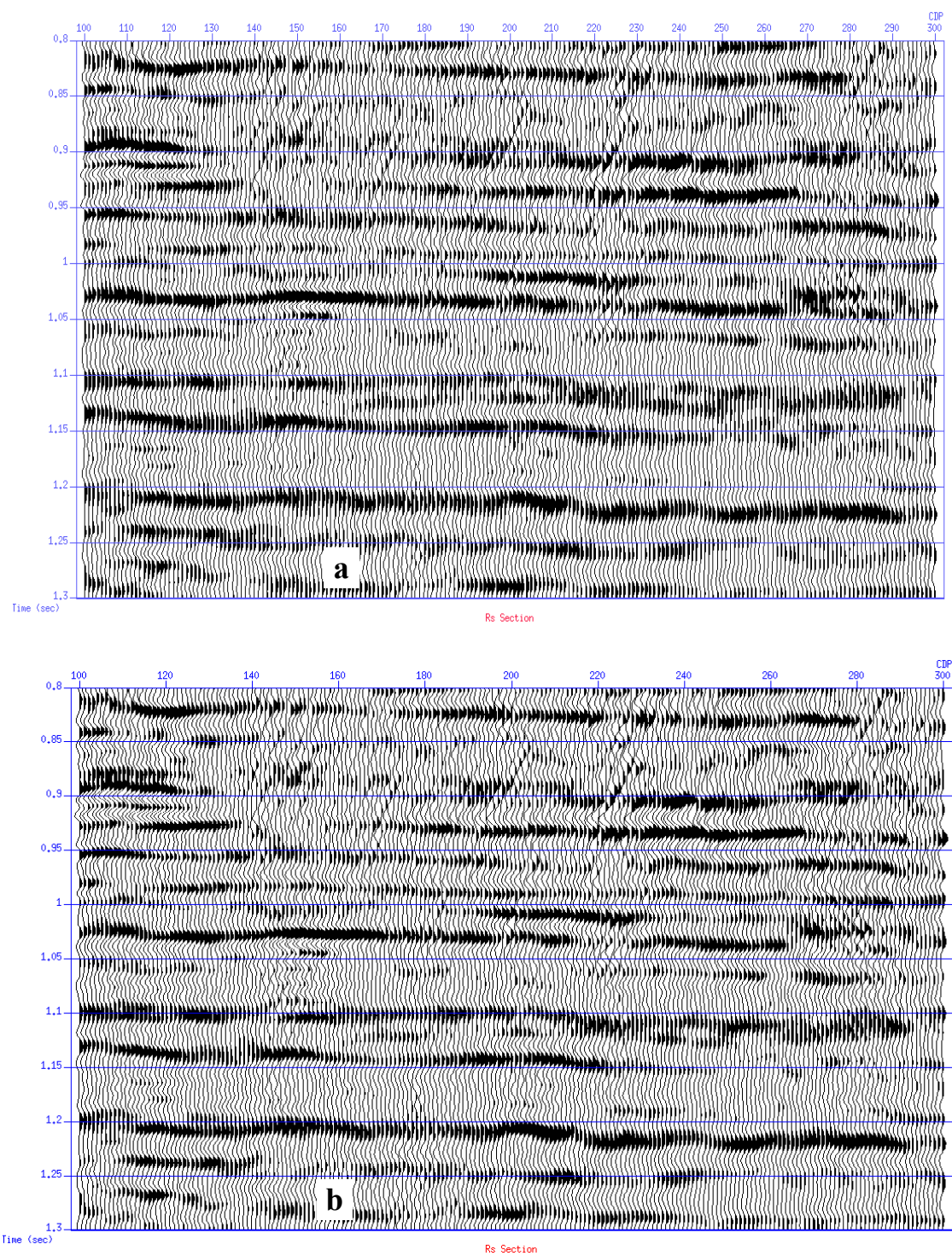


Figure 4.23. Extracted  $S$  wave reflectivity from vertical component. (b) is 50 degree phase rotation applied on (a).

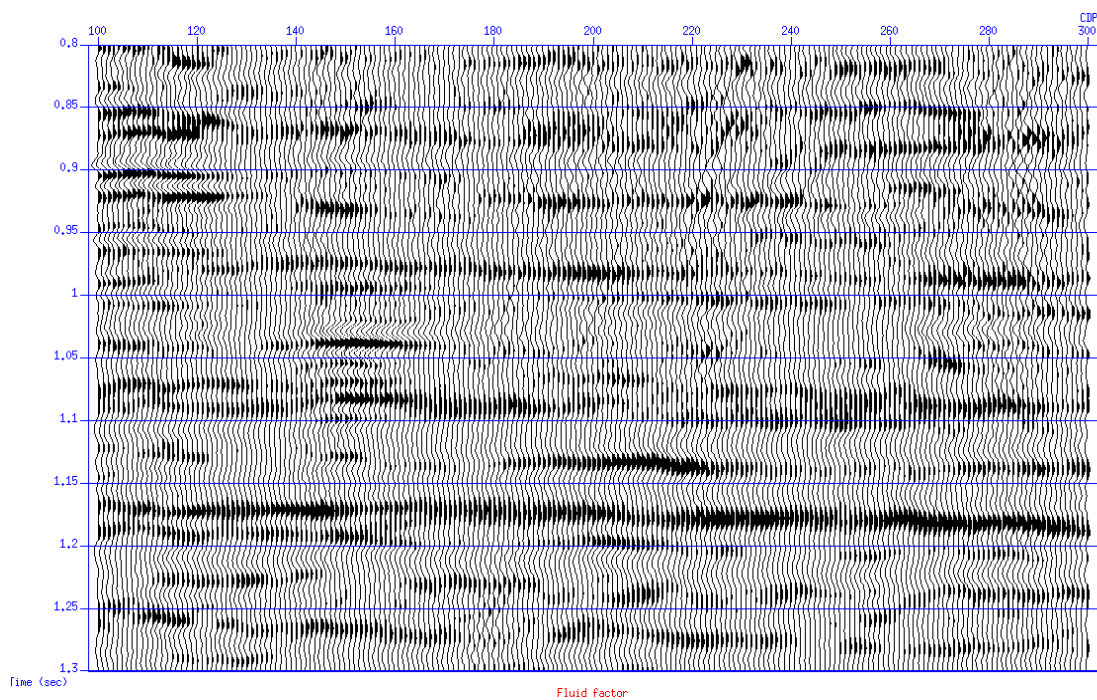
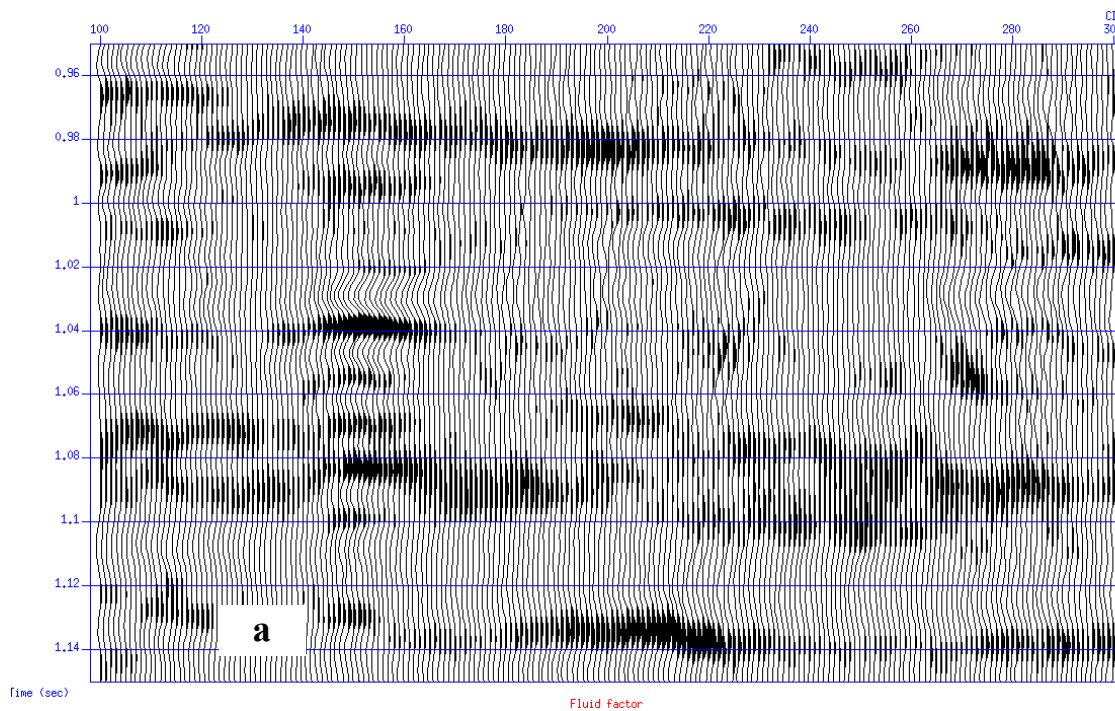


Figure 4.24. Fluid factor section calculated from extracted  $P$  wave and  $S$  wave sections and the mud-rock line.



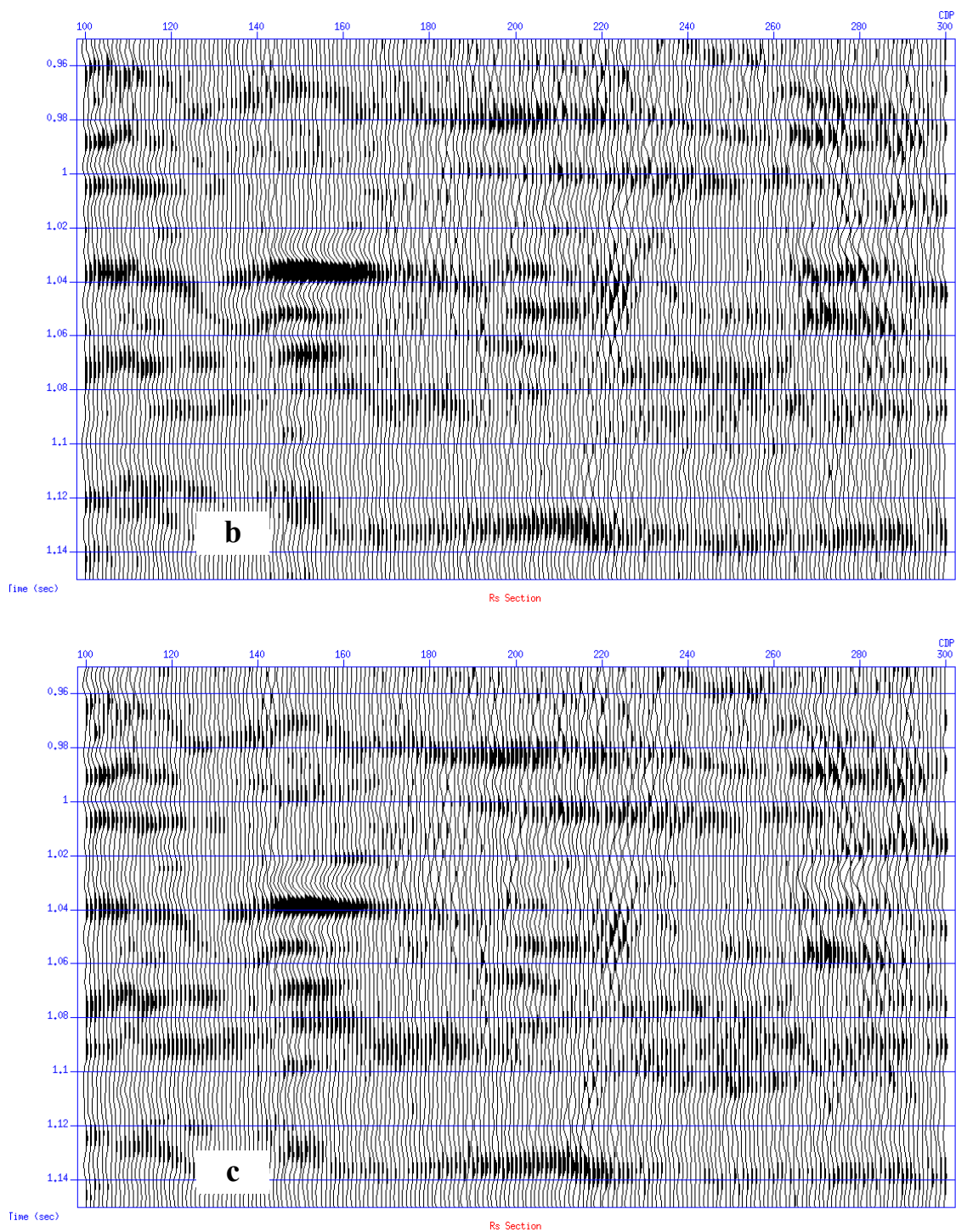


Figure 4.25. Zooming of fluid factor section of Figure 4.24 with channel zone. (a) original; (b) DECONed; (c) DECONed and 50 degree phase rotation

#### 4.4.3. Correlation of the extractions with well logs

The extraction results are now compared with the synthetics of the well logs.

In Figure 4.26, sonic and density logs from 04-16 are used to create normal incident seismograms. The synthetics tie with the  $R_p$  section very well.

In Figure 4.27, shear sonic and density logs are used to create pure  $S$  wave normal incident seismograms. The synthetic seismograms correlate to the  $R_s$  trace fairly well, especially, from the Viking to the Mississippian.

Figure 4.28 shows the correlation of fluid factor section with  $P$  and  $S$  wave velocities and density logs. Links between the well log curves with fluid factor section are not obvious.

In Figure 4.29 the deviation curve is calculated from well logs and combined with fluid factor. The negative or positive deviations to be observed briefly match the peak or trough on the fluid factor section.

In Figure 4.29, the central green curve is the deviation of  $P$  wave velocity from the statistical trend. The coals above Glauconitic on the curve have negative deviations. The section also shows a big trough. Glauconitic top has strong positive deviations on both section and curve. Other details inside the channel briefly match each other.

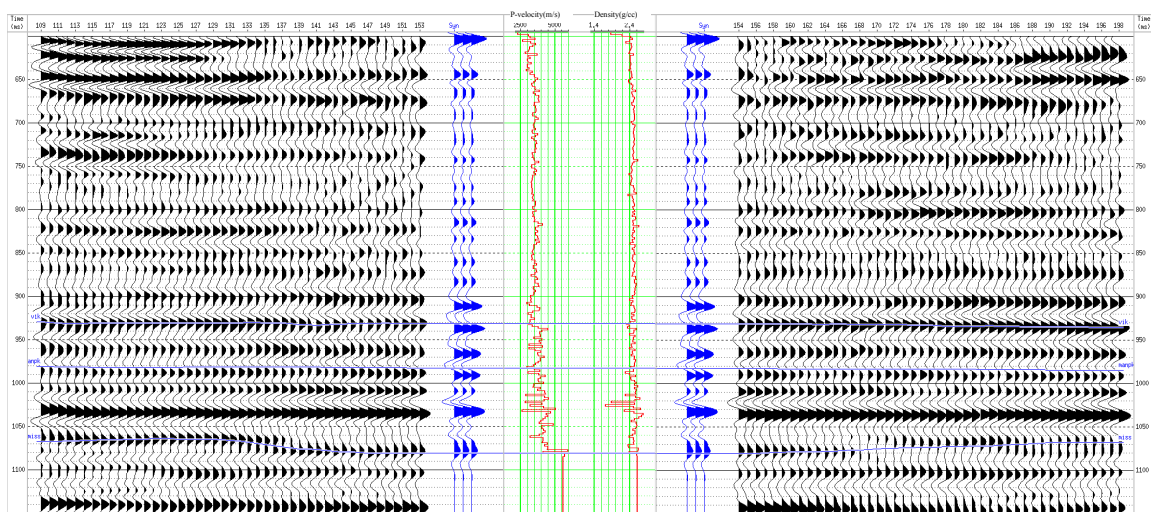


Figure 4.26. Well logs, synthetics and  $R_p$  extracted from vertical component.

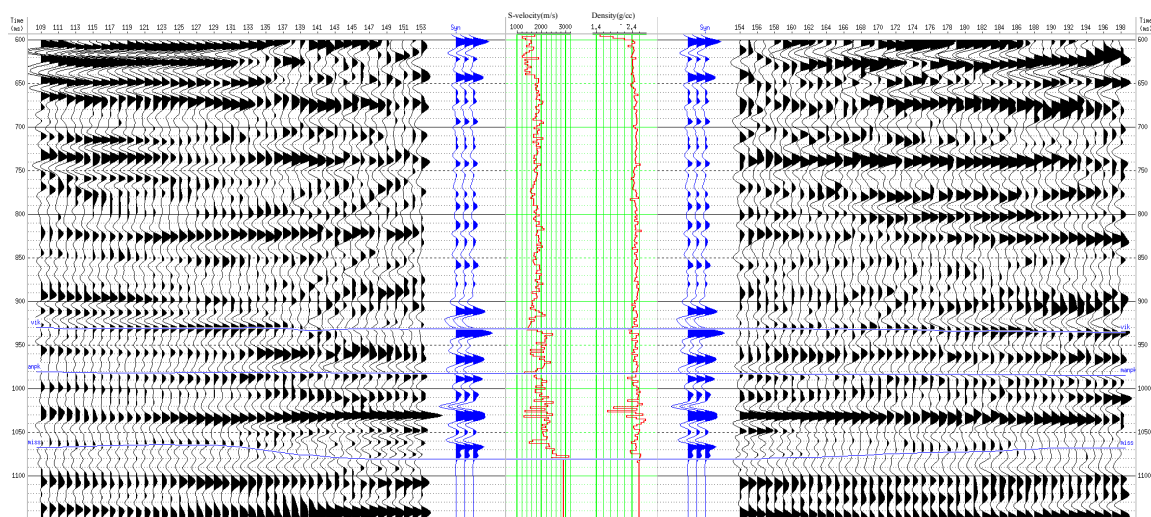


Figure 4.27. Well logs, synthetics and  $R_s$  extracted from vertical component.

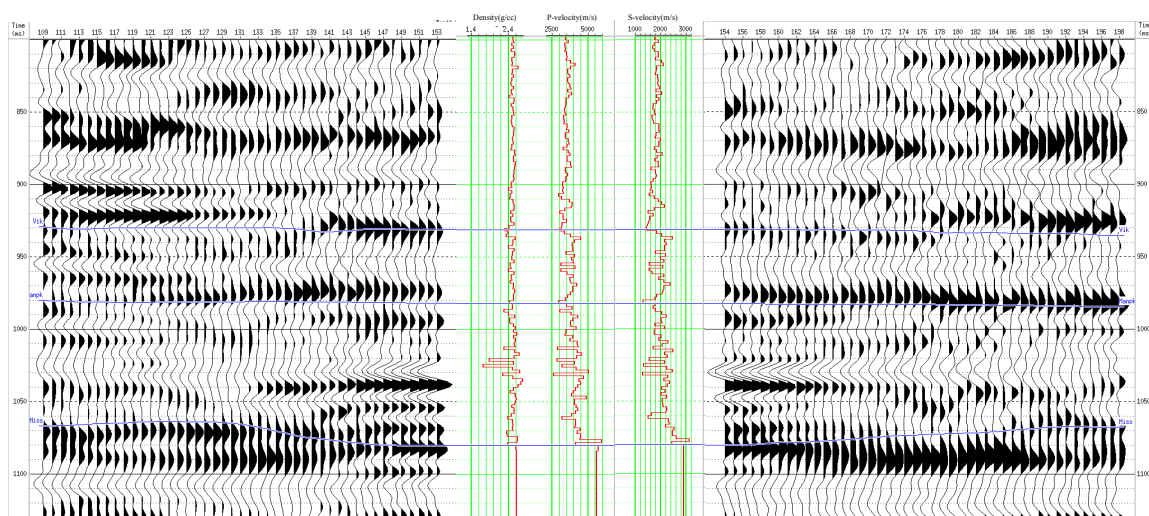


Figure 4.28. Well logs and fluid factor extracted from vertical component.

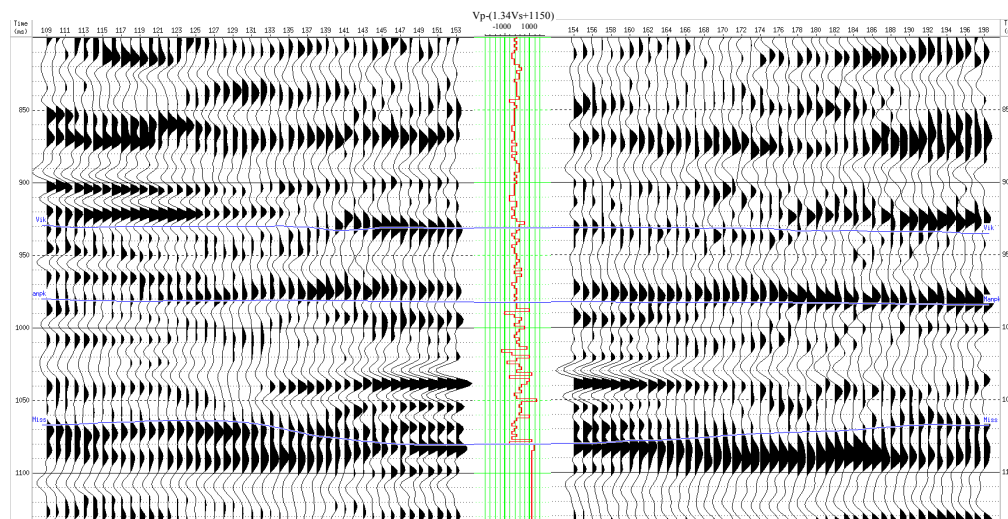


Figure 4.29. Fluid factor extracted from well logs and from vertical component.

#### 4.4.4. $R_p$ , $R_s$ , and fluid factor from CSP gathers

Equivalent offset migration is applied on the vertical component data set. The AVO extraction and fluid stack algorithms are applied on the CSP gathers. The  $R_p$ ,  $R_s$ , and fluid stack sections are shown in Figures 4.30 - 4.32. Both  $R_p$  and  $R_s$  sections (Figures 4.30 and 4.31) describe the similar geology structures as  $R_p$  and  $R_s$  sections from CMP gather (see Figures 4.22 and 4.23). On the  $R_s$  section in Figure 4.31, the Glauco channel bottom is better described, compared with the  $R_s$  section in Figure 4.23. The EOM helps to suppress the noise. However, the fluid stack section in Figure 4.32 calculated from CSP gathers has bigger difference from that from CMP gathers (see Figure 4.24). The coals in Mannville at time of 1025ms show continuous strong anomalies in Figure 4.32.

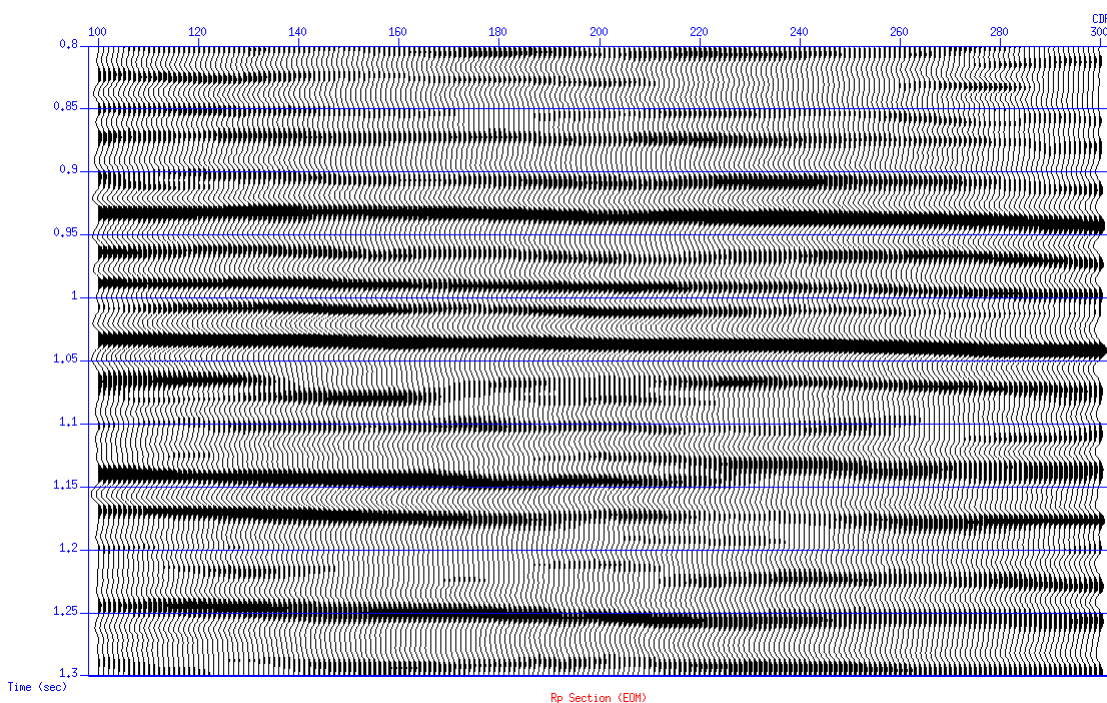


Figure 4.30. Extraction  $P$  wave reflectivity section from CSP gathers of the vertical component.

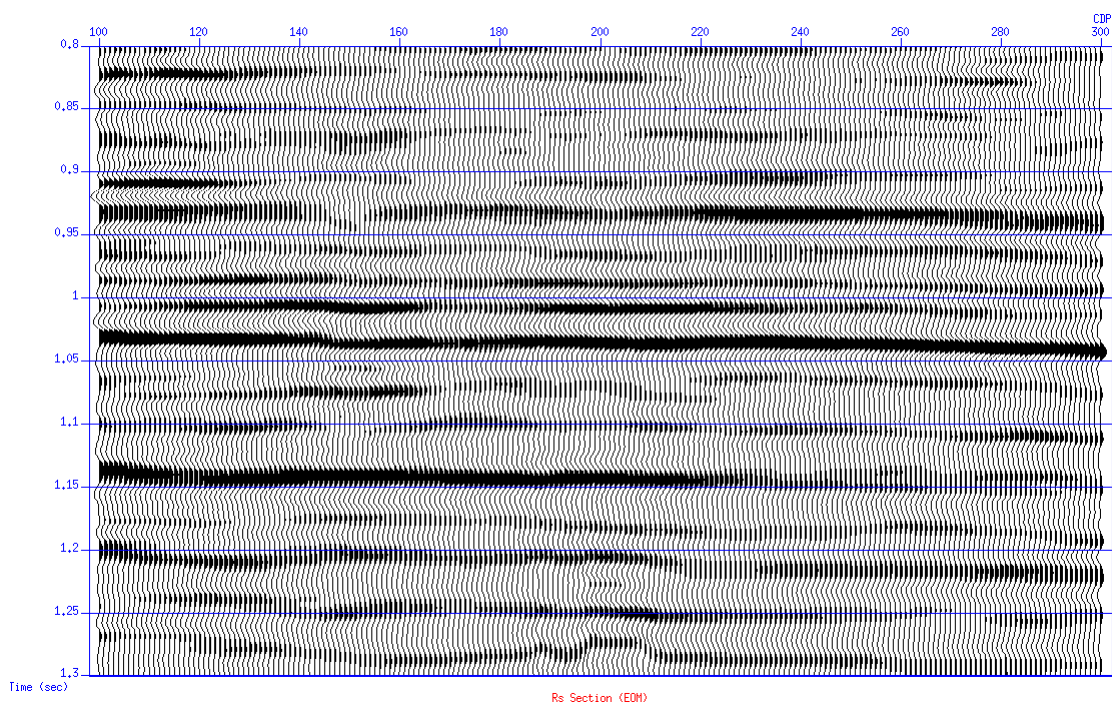


Figure 4.31. Extraction  $S$  wave reflectivity section from CSP gathers of the vertical component.

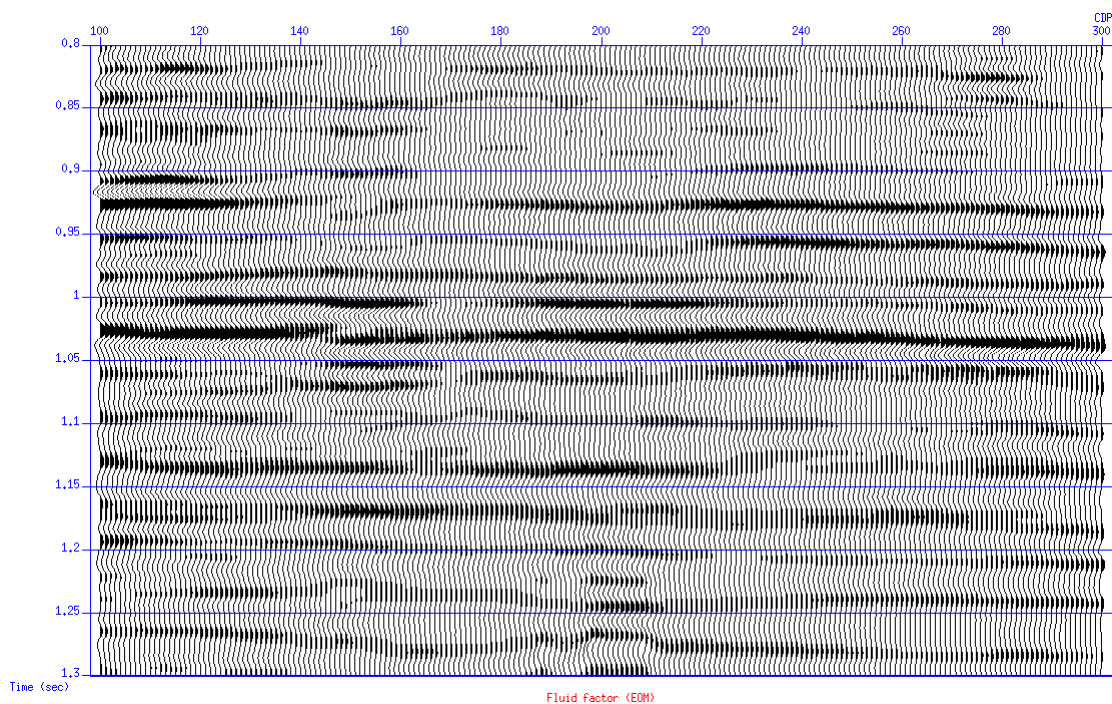


Figure 4.32. Fluid factor section calculated from  $P$  and  $S$  wave reflectivity sections from CSP gathers of the vertical component.

## 4.5. ANALYSIS OF RADIAL COMPONENT DATA

### 4.5.1. Methodology

The radial component of the 3C-2D line is dominated by converted mode energy. After special processing with rotation and separation, the data set is regarded as  $P$ - $S$  converted wave reflection. Therefore, the analysis of radial component of this 3C-2D line is based on the  $P$ - $S$  reflection coefficient.

$P$ - $S$  reflection coefficient can be simplified and associated with rock properties. Aki-Richards' approximation for  $P$ - $S$  reflection coefficient (see Chapter 2) can be reformatted in terms of rigidity and density:

$$R_{PS} = -\frac{1}{2} \frac{V_P}{V_S} \tan j \left[ \frac{\Delta\rho}{\rho} + 2 \frac{V_S}{V_P} \frac{\Delta\mu}{\mu} \cos(i+j) \right] \quad (4.28)$$

$$R_{PS} = -\frac{1}{2} \frac{V_P}{V_S} \tan j \left[ \left( \frac{\Delta\rho}{\rho} + 2 \frac{V_S}{V_P} \frac{\Delta\mu}{\mu} \right) - \frac{V_S}{V_P} \frac{\Delta\mu}{\mu} \left( \frac{V_P}{V_S} + 1 \right)^2 \sin^2 j \right]. \quad (4.29)$$

where  $i=(i_1+i_2)/2$  and  $j=(j_1+j_2)/2$  are following the conventions in Chapter 2.

In fact, equation (4.28) reveals the AVO variation for shear modulus and  $\rho$  term. The slope of  $P$ - $S$  wave AVO is primarily dependent on the shear modulus.

When  $\frac{V_S}{V_P} \sim \frac{1}{2}$  is assumed,

$$R_{PS} \approx -\tan j \left[ \frac{\Delta\rho}{\rho} + \frac{\Delta\mu}{\mu} \cos(i+j) \right], \quad (4.30)$$

$$R_{PS} \approx -\tan j \left[ -4R_{S0} - \frac{9}{2} \frac{\Delta\mu}{\mu} \sin^2 j \right], \quad (4.31)$$

where  $R_{S0} = -\frac{1}{2} \left( \frac{\Delta\rho}{\rho} + \frac{\Delta V_S}{V_S} \right)$  is the reflectivity of the normal incidence of the  $SH$  wave.

Equations (4.30) and (4.31) provide very good insights into the converted wave reflection. In this thesis,  $\frac{V_S}{V_P} \sim \frac{1}{2}$  is not assumed. Therefore, an equation similar to

equation (4.31), but more accurate, is used in the extraction of radial data. This equation is shown as equation (4.32).

$$R_{PS}(j) \approx -4 \tan(j) R_{S0} + \frac{1}{2} \tan(j) \sin^2(j) \left( \frac{V_P}{V_S} + 1 \right)^2 \frac{\Delta\mu}{\mu}. \quad (4.32)$$

Even in the horizontal homogeneous media, the incident  $P$  wave and converted  $S$  wave paths are not symmetrical, differing, thereby, from the incident  $P$  and reflected  $P$  wave paths. To obtain the incident angles, or, reflection angles, for the  $P$ - $S$  reflection, the  $V_P/V_S$  ratio is necessary even for a single interface case. In addition, the seismic data are usually sorted into common mid-point (CMP) gather form and the conversion from CMP gather to common converted point (CCP) gather is necessary before the  $P$ - $S$  seismic data can be extracted. Figure 4.33 illustrates the moving of a converted point as the  $V_P/V_S$  ratio changes in relation to fixed source and receiver positions.

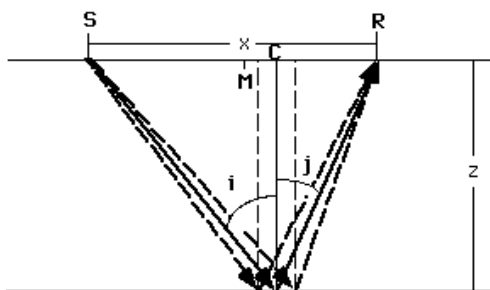


Figure 4.33. Illustration of propagation of incidence and converted wave.

#### 4.5.2. Extraction results from radial component

Figure 4.34 shows the stack section derived from the same data used to extract the  $S$  reflectivity section. Figure 4.35 shows the  $S$  reflectivity section extracted from radial component. The  $R_S$  section has higher resolution than stack section. In addition, the Glauconitic channel is slightly better described on the  $R_S$  section than on the stack section.

Finally, the  $R_s$  section from the vertical component (Figure (4.23)) is compared with the  $R_S$  section from the radial component (Figure (4.35)). There are similarities between both sections: in both, e.g., the Glauconitic top is strong, and Mississippian is

weak. However, the  $R_S$  section from the radial component is less continuous than from the vertical component.

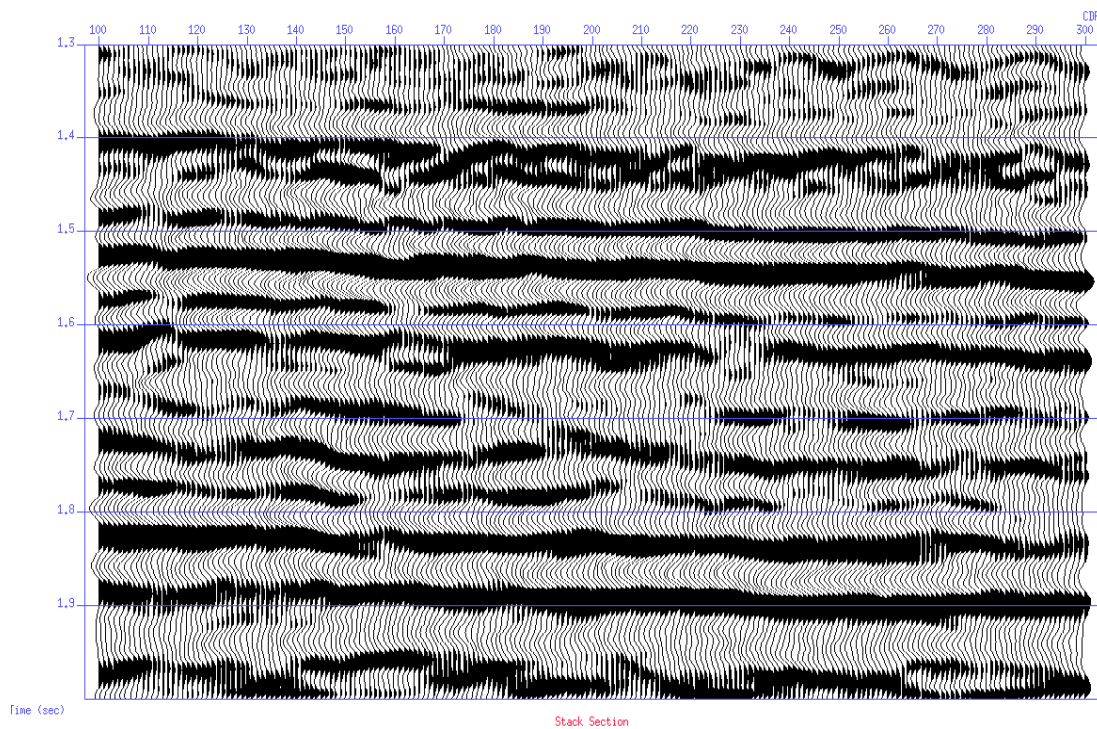


Figure 4.35. Stack section of the radial component with the same muting gate as in the AVO extraction.

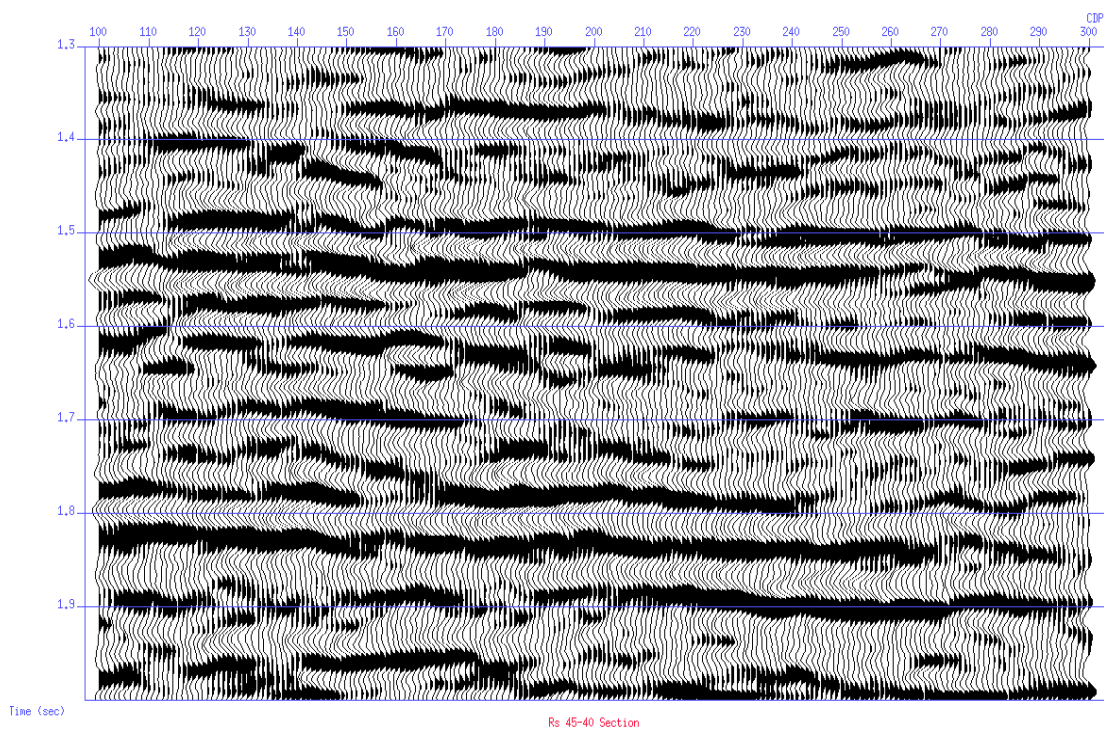


Figure 4.36. The extracted *S* wave normal incidence reflectivity from radial component.

# CHAPTER 5      CONCLUSIONS AND DISCUSSIONS

## 5.1. CHAPTER SUMMARY

This thesis is summarized as follows.

In Chapter 2, the reflection coefficients of compressional wave at ideal solid-solid interface are discussed and the approximations of Zoeppritz equations are studied. Aki-Richards' approximations of  $P$ - $P$  and  $P$ - $S$  reflection coefficients are also compared. At the normal incidence at the interface with elastic property variation,  $P$ - $S$  reflection coefficient is zero and  $P$ - $P$  reflection coefficient is not zero. In the small incident angle case, the magnitude of  $P$ - $P$  reflection coefficient is greater than the magnitude of  $P$ - $S$  reflection coefficient. Aki-Richards' approximation of  $P$ - $S$  reflection coefficient has larger relative error than the approximation of  $P$ - $P$  reflection coefficient in the model cases used in the thesis, especially the gas-filled sand cases. A higher order approximation of  $P$ - $S$  reflection coefficient is derived from the Zoeppritz equation, which is more accurate than the first order approximation. Different formats of the  $P$ - $S$  reflection coefficient equation are expressed with clear physical meaning and convenience for use in the extraction of AVO.

Chapter 3 discusses the methodology of AVO analysis. A number of AVO analysis methods in the industry are reviewed and compared prior to the discussion of their relative limitations and assumptions. The methodology of AVO analysis is summarized. The fluid factor method, as introduced by Smith and Gidlow (1987) is re-addressed. The sensitivities of Lamé's parameters are discussed. Theory and laboratory data indicate that the bulk ( $\kappa$ ) and shear ( $\mu$ ) moduli are very close for the dry rock, which suggests the difference between bulk ( $\kappa$ ) and shear ( $\mu$ ) moduli may work well as a fluid saturation indicator. When discussing the sensitivity of elastic parameters, it must be remembered that the reflectivities are actually the contrasts of rock properties and that the AVO response depends only on certain differences in properties instead of on absolute values. The noise issue is discussed using simple models. L1

norm estimation enables an approach to be used, which may help suppress multiples and linear noise. However,  $L2$  norm estimation is more robust at handling random noise.

In Chapter 4, both radial and vertical components of the 3C-2D line are studied. A methodology is developed to allow the use of the converted mode wave in AVO analysis. Both vertical and radial components of the 3C-2D seismic line are analyzed to extract elastic wave reflectivities. However, most efforts are made with AVO analysis of vertical component data. It should be noted that the vertical component is related to  $P$ - $P$  reflection and the radial component is related to the converted wave or the  $P$ - $S$  reflection. The mud-rock line, the linear relationship between  $V_p$  and  $V_s$ , is analyzed using wells with shear sonic logs in Blackfoot. Lamé's parameters are extracted from the vertical component. The Glauconitic channel shows an anomaly in the extracted Lamé's parameter sections and in the inverted sections.  $P$  wave and  $S$  wave reflectivities are also extracted from vertical component data. The fluid factor is calculated from the extracted  $P$  and  $S$  wave reflectivities. The Glauconitic channel shows an anomaly in extracted  $P$  wave and  $S$  wave reflectivity sections and the channel is clearly delineated by fluid factor extracted from vertical component. The AVO extraction and fluid factor calculation are applied on the CSP gathers created in the equivalent offset migration of vertical component. Finally,  $S$  wave reflectivity is extracted from radial component data. More work needs to be done on radial component data processing to obtain better result.

## 5.2. SUMMARY OF METHODOLOGY STUDY

The main work of methodology study in this thesis is summarized as the following:

- Higher order approximation of  $P$ - $S$  reflection coefficient;
- Convenient format of approximation for  $P$ - $S$  AVO analysis;
- Methodology to extract Lamé's parameters and inversion;
- $L1$  and  $L2$  norm fitting comparisons;
- Algorithms coding (fittings and ray-tracings) in Seismic Unix and Matlab;
- Decoupling lithology by crossplotting  $\Delta\lambda/(\lambda+2\mu)$  and  $\Delta\mu/(\lambda+2\mu)$ ;

- Methodology of joint  $P$ - $P$  and  $P$ - $S$  AVO analysis;
- Sensitivity of  $\kappa$ - $\mu$  as a direct hydrocarbon indicator.
- AVO analysis on CSP gathers from EOM.

### 5.3. SUMMARY OF WORK ON BLACKFOOT SURVEY

Blackfoot 3C-2D 10Hz line is used to test the developments in the thesis. AVO analysis done on this data set is summarized as follow:

- Statistical analysis of  $V_p$  and  $V_s$  from well logs;
- Lamé's parameters attribute extraction and inversion;
- $R_p$ ,  $R_s$ , and fluid factor extracted from vertical component data;
- $R_s$  extracted from radial component data.

### 5.4. PROBLEMS AND DISCUSSIONS

#### *True amplitude processing for the real data*

The 3C-2D seismic data used in AVO analysis was processed by Sensor Geophysical Ltd. The key processing flows to preserve the amplitude include surface consistent deconvolution and scaling, and spherical divergence corrections. The energy of CDP gathers after NMO correction is balanced with guidance of modeling from wells in the work of this thesis. To improve the AVO analysis, true amplitude processing should be applied.

#### *The amplitude preserved EOM*

The CSP gathers AVO is applied on in the thesis, is not assumed the AVO effect is preserved in the migration, although the AVO analysis results on CSP gathers and CMP gathers are comparable. Further study is necessary to solve the amplitude preserving problem.

#### *The phase of the vertical component seismic data*

On the stacked section,  $R_p$  section, and the correlation of these sections to well log synthetics, it is difficult to say if the phase is correct. However, the Wabamun (as a marker) top on the  $R_p$  section and the strong trough on the top of Glauconitic channel on the fluid factor section show the about 50 degree phase rotation may be necessary.

The crossplot of AVO attributes is the favorite for many interpreters. The crossplot of intercept and gradient is often used. However the intercept and gradient are coupling the  $Vp/Vs$  variation. From the crossplot of intercept and gradient, the  $Vp/Vs$  ratio variation is not easy to interpret. The crossplot of  $\Delta\lambda/(\lambda+2\mu)$  and  $\Delta\mu/(\lambda+2\mu)$  can decouple the  $Vp/Vs$  variation. Theoretical curves in this thesis show the area with  $Vp/Vs$  of about 2 exhibits better differentiation than too high or too low  $Vp/Vs$  ratios. It is promising to study the crossplot of  $\Delta\lambda/(\lambda+2\mu)$  and  $\Delta\mu/(\lambda+2\mu)$  in term of application on the real cases Further work will be done on this topic.  $\Delta\lambda/(\lambda+2\mu)$  and  $\Delta\mu/(\lambda+2\mu)$  is the variation based on same variable  $(\lambda+2\mu)$ . They have strong comparability and can be extracted from AVO analysis without contamination of errors of background  $Vp/Vs$  ratio.

## REFERENCES

- Aki, K. I. and Richards, P. G., 1980, Quantitative seismology: W.H. Freeman and CO.
- Behle, A. and Dohr, G. 1985, Converted waves in exploration seismic *in* Seismic Shear Waves, G. Dohr (ed.), 178-220. *Handbook of Geophysical Exploration*, Vol. 15b. Geophysical Press.
- Bancroft, J. C., Geiger, H. D., and Margrave, G. F., 1998, The equivalent offset method of prestack time migration: *Geophysics*, V. 63, 2042-2053.
- Bortfeld, R., 1961, Approximation to the reflection and transmission coefficients of plane longitudinal and transverse waves: *Geophys. Prosp.*, 9, 485 - 502.
- Castagna, J. P., Batzle, M. L. and Eastwood, R. L., 1985, Relationship between compressional wave and shear wave velocities in clastic silicate rocks: *Geophysics*, V. 50, 571 - 581.
- Castagna, J. P., 1993, Petrophysical imaging using AVO: *The Leading Edge*, March, 1993, 172-178.
- Castagna, J. P., Batzle, M. L. and Kan, T. K., 1993, Rock physics: the link between rock properties and AVO response *in* Castagna, J. P., and Backus, M. M., Eds., *Offset-dependent reflectivity--Theory and practice of AVO analysis*, Soc. Expl. Geophys., 135-171.
- Castagna, J. P., and Smith, S. W., 1994, Comparison of AVO indicators: A modeling study: *Geophysics*, V59, 1849-1855.
- Castagna, J. P., Swan, H. W., and Foster, D. J., 1998, Framework for AVO gradient and intercept interpretation: *Geophysics*, V63, 948-956.
- Chiburis, E., F., 1993, AVO applications in Saudi Arabia *in* Castagna, J. P., and Backus, M. M., Eds., *Offset-dependent reflectivity--Theory and practice of AVO analysis*, Soc. Expl. Geophys., 211-229.
- Chung, W. Y., and Corrigan, D., 1985, Gathering mode-converted shear waves: a model study: 55th SEG meeting, Washington, Expanded Abstracts, 602-604.
- Dahl, T., and Ursin, B., 1991, Parameter estimation in a one-dimensional anelastic medium, *Journal of Geophysical Research*, V 96, 20,217 - 20, 233.

- Dey-Sarkar, S. K., and Svatek, S. V., Prestack analysis – An integrated approach for seismic interpretation in Clastic basins *in* Castagna, J. P., and Backus, M. M., Eds., Offset-dependent reflectivity--Theory and practice of AVO analysis, Soc. Expl. Geophys., 57-77.
- Fatti J. L., Smith. G. C., Vail P. J., Strauss, P. J. and Levitt, P.R., 1994, Detection of gas in sandstone reservoirs using AVO analysis: a 3\_D case history using Geostack technique: Geophysics V59, 1362-1376.
- Ferguson, R. J., P-P and P-S inversion of 3-C seismic data: Blackfoot, Alberta: CREWES Research Report 1995, Chapter 41.
- Goodway, B., Chen, T., and Downton, J., 1997, Improved AVO fluid detection and lithology discrimination using Lamé petrophysical parameters; “ $\lambda\rho$ ”, “ $\mu\rho$ ”, and “ $\lambda/\mu$  fluid stack”, from P and S inversions: CSEG national convention, Expanded Abstracts, 148-151.
- Goodway, B., Chen, T., and Downton, J., 1997, Improved AVO fluid detection and lithology discrimination using Lamé petrophysical parameters; “ $\lambda\rho$ ”, “ $\mu\rho$ ”, and “ $\lambda/\mu$  fluid stack”, from P and S inversions: 67th Ann. Internat. Mtg., Soc. Expl. Geophys., Expanded Abstracts.
- Garotta, R., 1988, Amplitude-versus-offset measurements involving converted waves: 58th Ann. Internat. Mtg., Soc. Expl. Geophys., Expanded Abstracts, 1357.
- Hampson, D., and Russell, B., 1990, AVO inversion: theory and practice: 60th Ann. Internat. Mtg., Soc. Expl. Geophys., Expanded Abstracts, 1456-1458.
- Koefoed, O., 1955, On the effect of Poisson’s ratio of rock strata on the reflection coefficients of plane waves: Geophys. Prosp., 3, 381-387.
- Lindseth, R. O., 1979, Synthetic sonic logs -- a processing for stratigraphic interpretation: Geophysics, V. 44, No 1, 3 -26.
- Margrave, G. F., Foltinek, D. S., 1995, P-P and P-SV cross sections: CREWES Research Report 1995, Chapter 5.
- Miller, S. L. M., Aydemir, E. O., and Margrave, G. F., 1995, Preliminary interpretation of P-P and P-S seismic data from the Blackfoot broad-band survey: CREWES Research Report 1995, Chapter 42.

- Parson, R., 1986, Estimating reservoir mechanical properties using constant offset images of reflection coefficients and incident angles: 56th Ann. Internat. Mtg., Expanded Abstracts, 617-620.
- Pigott, J. D., Shrestha, R. K., and Warwick, R. A., 1990, Direct determination of Carbonate reservoir porosity and pressure from AVO inversion: 60<sup>th</sup> Ann. Internat. Mtg., Soc. Expl. Geophys., Expanded Abstracts, 1533-1536.
- Potter, C. C., Miller, S. L. M., and Margrave, G. F., 1995, Formation elastic parameters and synthetic P-P and P-S seismograms for the Blackfoot field: CREWES Research Report 1995, Chapter 37.
- Press, Flannery, Teukolsky, and Vetterling, 1986, Numerical recipes, Cambridge university press.
- Rutherford, S. R. and Williams, R. H., 1989, Amplitude-versus-offset variation in gas sands: Geophysics, 54, 680-688.
- Simin, V., Margrave, G. F., and Yang G. Y. C., AVO measurements for P-P and P-S data in Blackfoot 3C-3D dataset: CREWES Research Report 1995, Chapter 42.
- Smith, G. C., and Gidlow, P. M., 1987, Weighted stacking from rock property estimation and detection of gas: Geophys. Prosp. 35, 993-1014.
- Spratt, R. S., Goins, N. R., and Fitch, T. J., 1993, Pseudo-shear: The analysis of AVO in Castagna, J. P., and Backus, M. M., Eds., Offset-dependent reflectivity--Theory and practice of AVO analysis, Soc. Expl. Geophys., 37-56.
- Shuey, R. T. 1985, A simplification of the Zoeppritz equations: Geophysics, V 50, 609 - 614.
- Stewart, R. R., Zhang, Q., and Guthoff, F., 1995, Relationships among elastic-wave values ( $R^{PP}$ ,  $R^{PS}$ ,  $R^{SS}$ ,  $V_p$ ,  $V_s$ ,  $\rho$ ,  $\sigma$ ,  $\kappa$ ): CREWES Research Report 1995, Chapter 10.
- Swan, H. W., 1991, Amplitude-versus-offset measurement errors in a finely layered medium: Geophysics, 56, 41-49.
- Taylor, G., The point of P-S mode-converted reflection: An exact determination: Geophysics, 54, 1060-1063.
- Tessmer, G., and Behle, A., 1988, Common reflection point data-stacking technique for converted waves: Geophys. Prosp., V 36, 671-688.

- Verm, R. W., and Hilterman, F. J., 1994, Lithologic color-coded sections by AVO cross plots: *The Leading Edge*, August, 847 - 853.
- Xu, Y. and Bancroft, J. C., 1997, Joint AVO analysis of PP and PS data, CREWES sponsors' annual meeting report, chapter 34.
- Xu, Y. and Bancroft, J. C., 1998, AVO case study: Extraction of Lamé's parameters from vertical component seismic data: Presented at Geotriad'98, Canada.
- Xu, Y. and Bancroft, J. C., 1998, Statistical relationships between  $V_p$  and  $V_s$  from well logs, CREWES sponsors' annual meeting report, chapter 46.
- Xu, Y. and Bancroft, J. C., 1999, Description of Glauconitic channel by AVO analysis: Presented at CSEG national annual meeting.
- Yu, G., 1985, Offset-amplitude variation and controlled-amplitude processing: *Geophysics*, 50, 2697-2708.
- Zheng, X., 1992, United formulas for reflection and transmission in potential: Presented at the 62nd Annual International SEG Meeting, New Orleans, abstr. book, 1282-1284.
- Zhong, B., Zhou, X., Liu, X., and Jiang, Y., A new strategy for CCP stacking: *Geophysics*, 60, 517-521.

## APPENDIX

### A. ZOEPPRITZ EQUATIONS OF P-P AND P-S REFLECTION COEFFICIENTS

Aki and Richards (1980) expressed the Knot-Zoeppritz equations in convenient forms. The reflection coefficients of the incident  $P$  wave and reflected  $P$  wave and  $S$  wave are shown as follows:

$$PP = [(b \frac{\cos i_1}{\alpha_1} - c \frac{\cos i_2}{\alpha_2})F - (a + d \frac{\cos i_1}{\alpha_1} \frac{\cos j_1}{\beta_1})Hp^2] / D,$$

$$PS = -2 \frac{\cos i_1}{\alpha_1} (ab + cd \frac{\cos i_2}{\alpha_2} \frac{\cos j_2}{\beta_2}) p \alpha_1 / (\beta_1 D),$$

where

$$M = \begin{pmatrix} -\alpha_1 p & -\cos j_1 & \alpha_2 p & \cos j_2 \\ \cos i_1 & -\beta_1 p & \cos i_2 & -\beta_2 p \\ 2\rho_1 \beta_1^2 p \cos i_1 & \rho_1 \beta_1 (1 - 2\beta_1^2 p^2) & 2\rho_2 \beta_2^2 p \cos i_2 & \rho_2 \beta_2 (1 - 2\beta_2^2 p^2) \\ -\rho_1 \alpha_1 (1 - 2\beta_1^2 p^2) & 2\rho_1 \beta_1^2 p \cos j_1 & \rho_2 \alpha_2 (1 - 2\beta_2^2 p^2) & -2\rho_2 \beta_2^2 p \cos j_2 \end{pmatrix},$$

$$a = \rho_2 (1 - 2\beta_2^2 p^2) - \rho_1 (1 - 2\beta_1^2 p^2), \quad b = \rho_2 (1 - 2\beta_2^2 p^2) + 2\rho_1 \beta_1^2 p^2,$$

$$c = \rho_1 (1 - 2\beta_1^2 p^2) + 2\rho_2 \beta_2^2 p^2, \quad d = 2(\rho_2 \beta_2^2 - \rho_1 \beta_1^2),$$

$$E = b \frac{\cos i_1}{\alpha_1} + c \frac{\cos i_2}{\alpha_2}, \quad F = b \frac{\cos j_1}{\beta_1} + c \frac{\cos j_2}{\beta_2},$$

$$G = a - d \frac{\cos i_1}{\alpha_1} \frac{\cos j_2}{\beta_2}, \quad H = a - d \frac{\cos i_2}{\alpha_2} \frac{\cos j_1}{\beta_1},$$

and

$$D = EF + GHp^2 = (\det M) / (\alpha_1 \alpha_2 \beta_1 \beta_2).$$

The angles of  $i_1$ ,  $i_2$ ,  $j_1$ , and  $j_2$  are shown on Figure A-1.

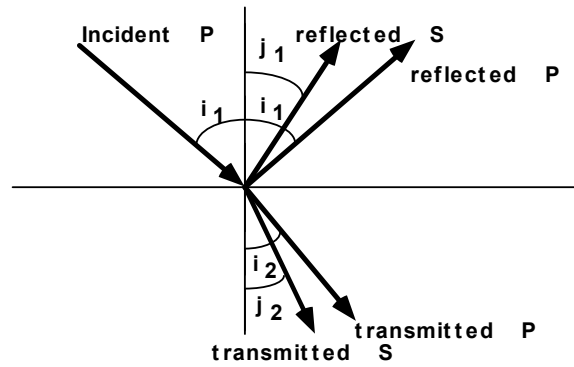


Figure A-1. Waves generated at an interface by an incident  $P$ -wave.

## B. DERIVATION OF EQUATIONS (3.7) AND (3.8)

$P$  and  $S$  wave velocities have relationship with Lamé's parameters as follows

$$V_P = \sqrt{\frac{\lambda + 2\mu}{\rho}} = \sqrt{\frac{\kappa + \frac{4}{3}\mu}{\rho}},$$

and

$$V_S = \sqrt{\frac{\mu}{\rho}}.$$

After reformatting the above two expressions, we have:

$$V_P^2 \rho = \lambda + 2\mu = \kappa + \frac{4}{3}\mu, \quad (\text{B.1})$$

and

$$V_S^2 \rho = \mu. \quad (\text{B.2})$$

From (B.1) and (B.2), we obtain

$$2 \frac{\Delta V_P}{V_P} + \frac{\Delta \rho}{\rho} = \frac{\Delta(\lambda + 2\mu)}{\lambda + 2\mu} = \frac{\Delta(\kappa + \frac{4}{3}\mu)}{\kappa + \frac{4}{3}\mu}, \quad (\text{B.3})$$

and

$$2 \frac{\Delta V_S}{V_S} + \frac{\Delta \rho}{\rho} = \frac{\Delta \mu}{\mu}. \quad (\text{B.4})$$

After further reformatting, we have

$$\frac{\Delta V_P}{V_P} = \frac{1}{2} \left( \frac{\Delta(\lambda + 2\mu)}{\lambda + 2\mu} - \frac{\Delta \rho}{\rho} \right) = \frac{1}{2} \left( \frac{\Delta(\kappa + \frac{4}{3}\mu)}{\kappa + \frac{4}{3}\mu} - \frac{\Delta \rho}{\rho} \right), \quad (\text{B.5})$$

and

$$\frac{\Delta V_S}{V_S} = \frac{1}{2} \left( \frac{\Delta \mu}{\mu} - \frac{\Delta \rho}{\rho} \right). \quad (\text{B.6})$$

Aki and Richards' (1980) approximation of  $P$ - $P$  reflection coefficient is:

$$R_{PP}(\theta) = \frac{1}{2} (1 + \tan^2 \theta) \frac{\Delta V_P}{V_P} - 4 \left( \frac{V_S}{V_P} \right)^2 \sin^2 \theta \frac{\Delta V_S}{V_S} + \frac{1}{2} \left( 1 - 4 \left( \frac{V_S}{V_P} \right)^2 \sin^2 \theta \right) \frac{\Delta \rho}{\rho}. \quad (\text{B.7})$$

After substituting (B.5) and (B.6) into (B.7), we have

$$R_{PP}(\theta) = \frac{1}{4} (1 + \tan^2 \theta) \frac{\Delta(\lambda + 2\mu)}{\lambda + 2\mu} - 2 \left( \frac{V_S}{V_P} \right)^2 \sin^2 \theta \frac{\Delta \mu}{\mu} + \frac{1}{4} (1 - \tan^2 \theta) \frac{\Delta \rho}{\rho}, \quad (\text{B.8})$$

and

$$R_{PP}(\theta) = \frac{1}{4} (1 + \tan^2 \theta) \frac{\Delta(\kappa + \frac{4}{3}\mu)}{\kappa + \frac{4}{3}\mu} - 2 \left( \frac{V_S}{V_P} \right)^2 \sin^2 \theta \frac{\Delta \mu}{\mu} + \frac{1}{4} (1 - \tan^2 \theta) \frac{\Delta \rho}{\rho}. \quad (\text{B.9})$$

Using the relationship between  $V_P/V_S$  and Lamé's parameters:

$$\left( \frac{V_S}{V_P} \right)^2 = \frac{\mu}{\lambda + 2\mu} = \frac{\mu}{\kappa + \frac{4}{3}\mu},$$

(B.8) and (B.9) are reformatted into equations (3.7) and (3.8) as follows:

$$R_{PP}(\theta) = \frac{1}{4} (1 + \tan^2 \theta) \frac{\Delta(\lambda + 2\mu)}{\lambda + 2\mu} - \sin^2 \theta \frac{2\Delta \mu}{\lambda + 2\mu} + \frac{1}{4} (1 - \tan^2 \theta) \frac{\Delta \rho}{\rho}, \quad (\text{3.7})$$

and

$$R_{PP}(\theta) = \frac{1}{4}(1 + \tan^2 \theta) \frac{\Delta(\kappa + \frac{4}{3}\mu)}{\kappa + \frac{4}{3}\mu} - \sin^2 \theta \frac{2\Delta\mu}{\kappa + \frac{4}{3}\mu} + \frac{1}{4}(1 - \tan^2 \theta) \frac{\Delta\rho}{\rho}.$$

(3.8)